清华大学地球系统科学前沿系列讲座
2013年6月3号

地球陆表辐射能量平衡之研究进展

梁顺林
北京师范大学全球变化与地球系统科学研究院

Department of Geographical Sciences
University of Maryland at College Park, USA
sliang@umd.edu, http://www.glue.umd.edu/~sliang

Acknowledgements

Liang

- This work is done by many individuals and some of the materials are also from the multiple sources.

提纲

Liang

- ♣ 背景
- ♣ 下行太阳辐射/天空”变亮”与”变暗”
- ♣ 反照率
- ♣ 下行长波辐射
- ♣ 温度，发射率和上行长波辐射
- ♣ ET

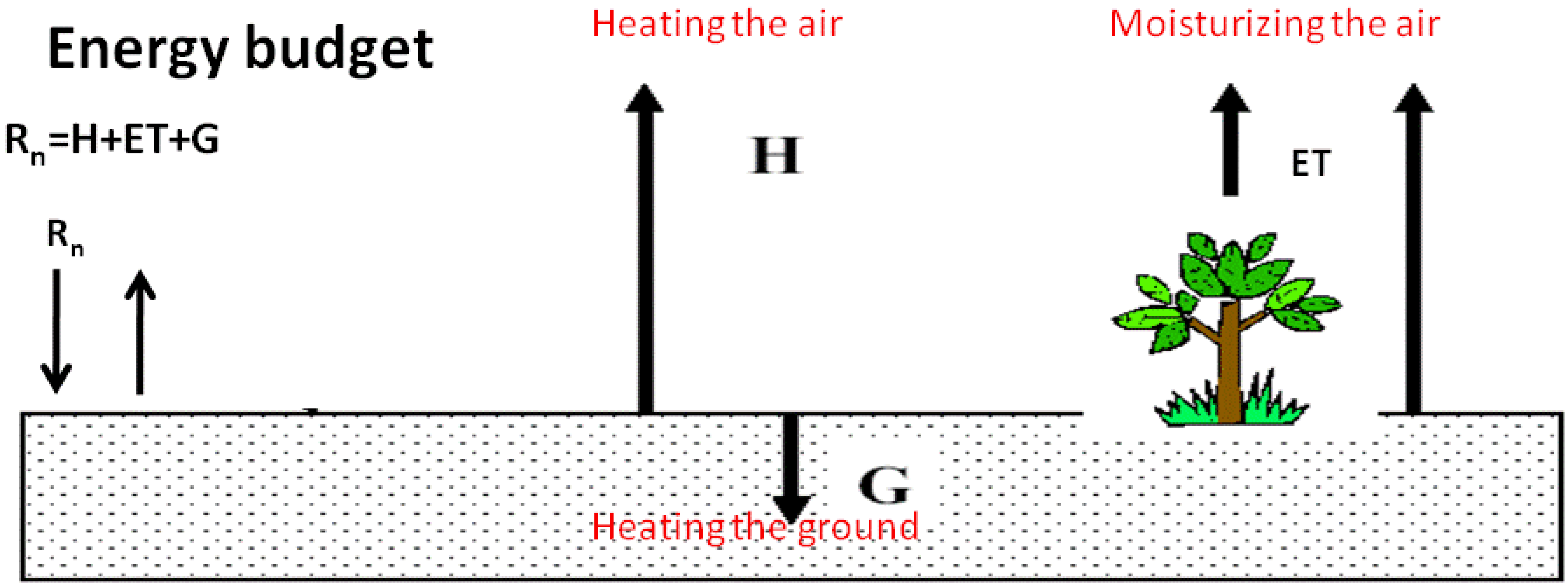

$$R_n = R_n^s + R_n^l = (1-\alpha)F_d^s + \varepsilon F_d^l - \sigma\varepsilon T^4$$

Net radiation

albedo

Insolation

Emissivity

Longwave downward radiation

Skin temperature

Radiation budget

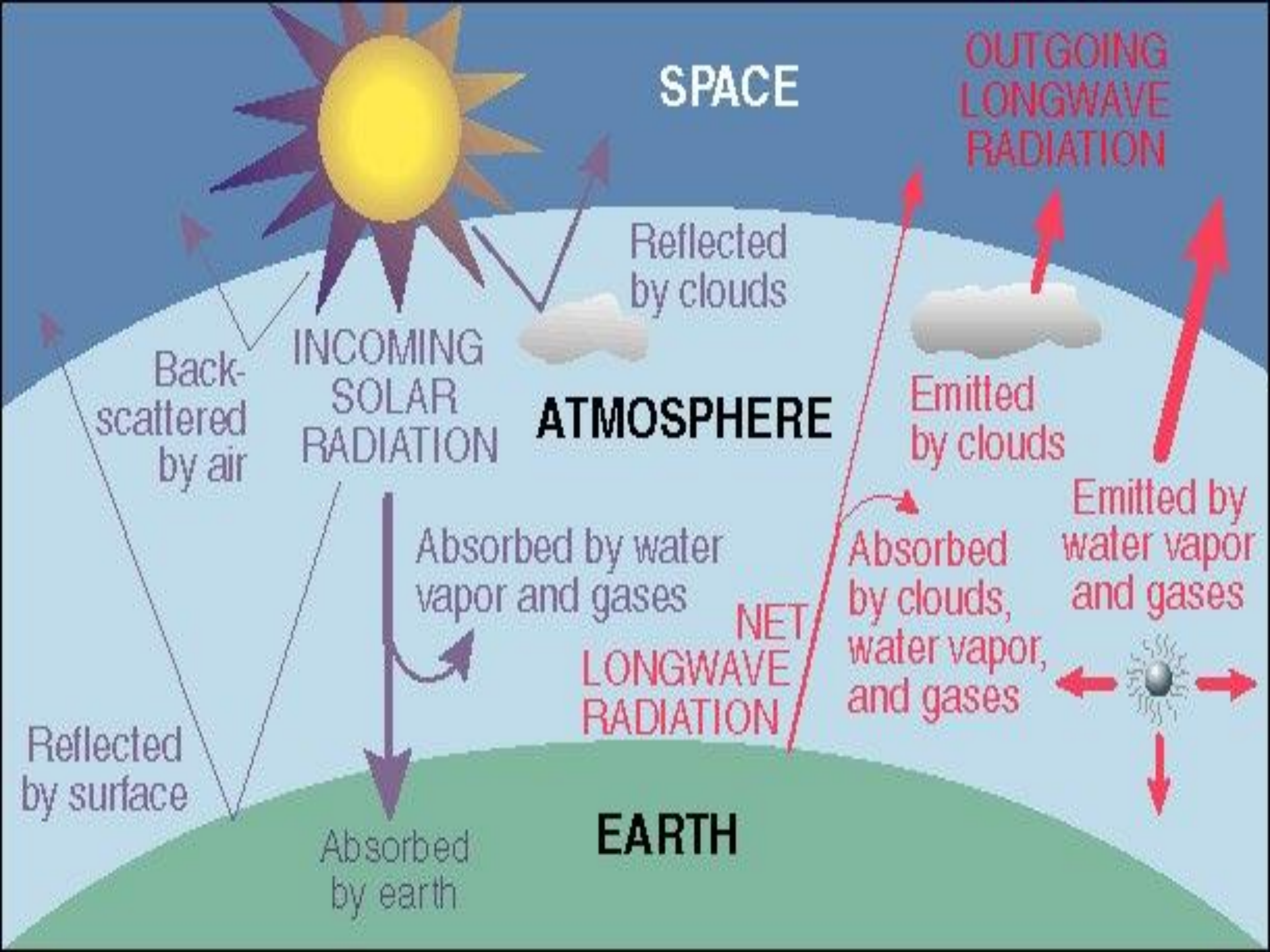
SPACE
OUTGOING LONGWAVE RADIATION
Reflected by clouds
INCOMING SOLAR RADIATION
Back-scattered by air
ATMOSPHERE
Emitted by clouds
Emitted by water vapor and gases
Absorbed by water vapor and gases
NET LONGWAVE RADIATION
Absorbed by clouds, water vapor, and gases
Reflected by surface
EARTH
Absorbed by earth

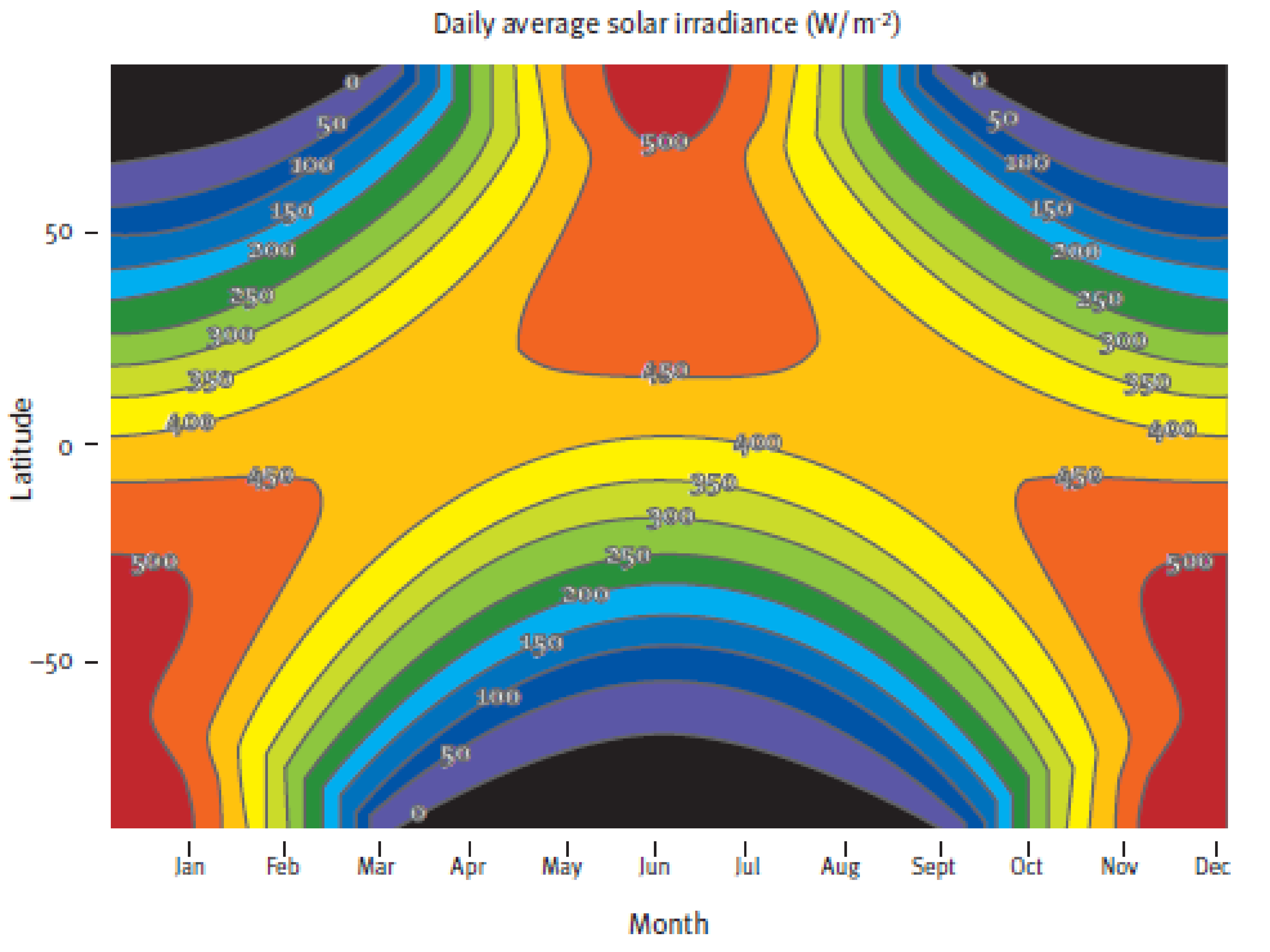

Daily average solar irradiance (W/ m⁻²)
Latitude
50
0
−50
Month
Jan
Feb
Mar
Apr
May
Jun
Jul
Aug
Sept
Oct
Nov
Dec
0
50
100
150
200
250
300
350
400
450
500

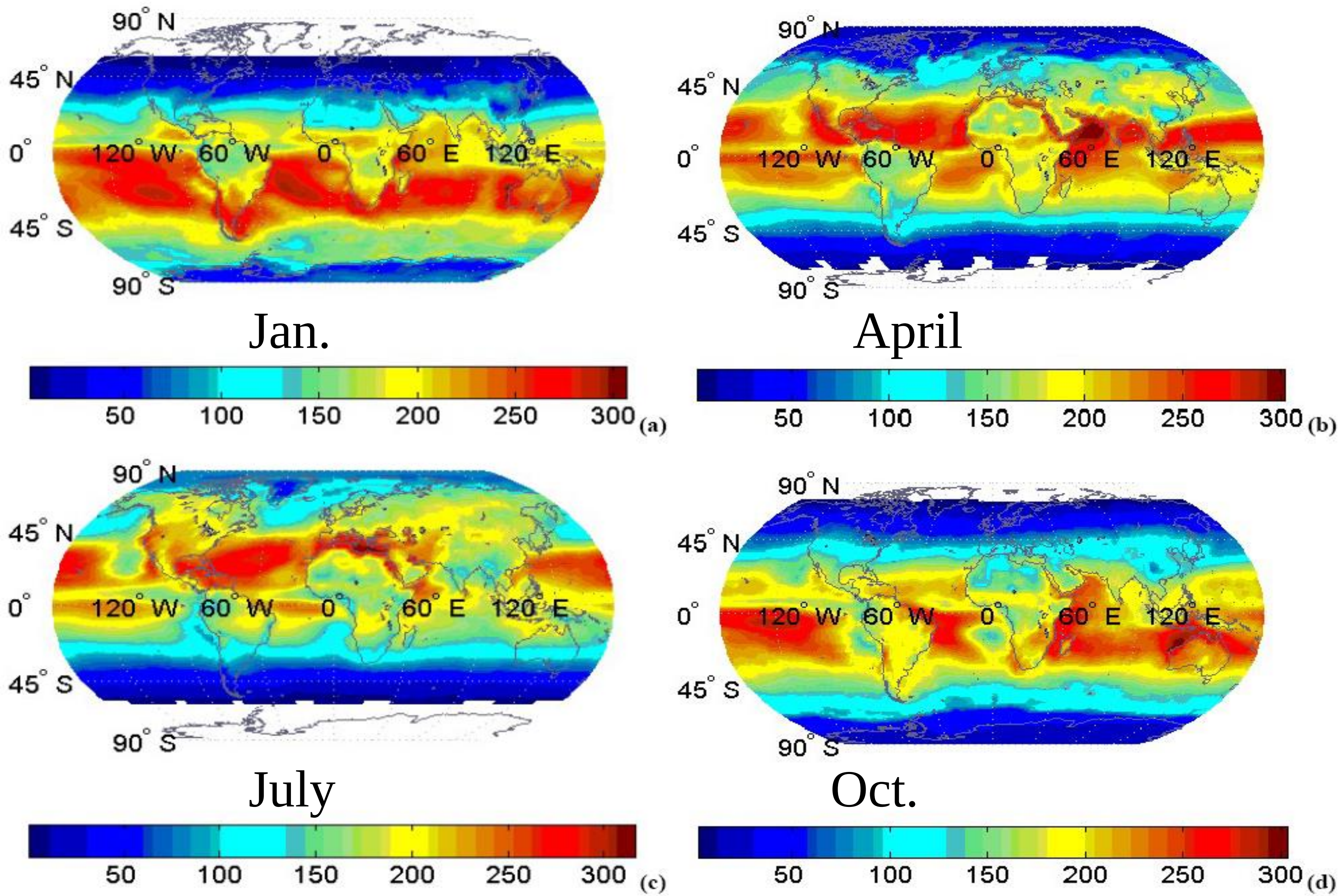

Long-term (1984–2000) average global distribution of downward net surface shortwave radiation (Wm−2) (Hatzianastassiou et al., 2005)

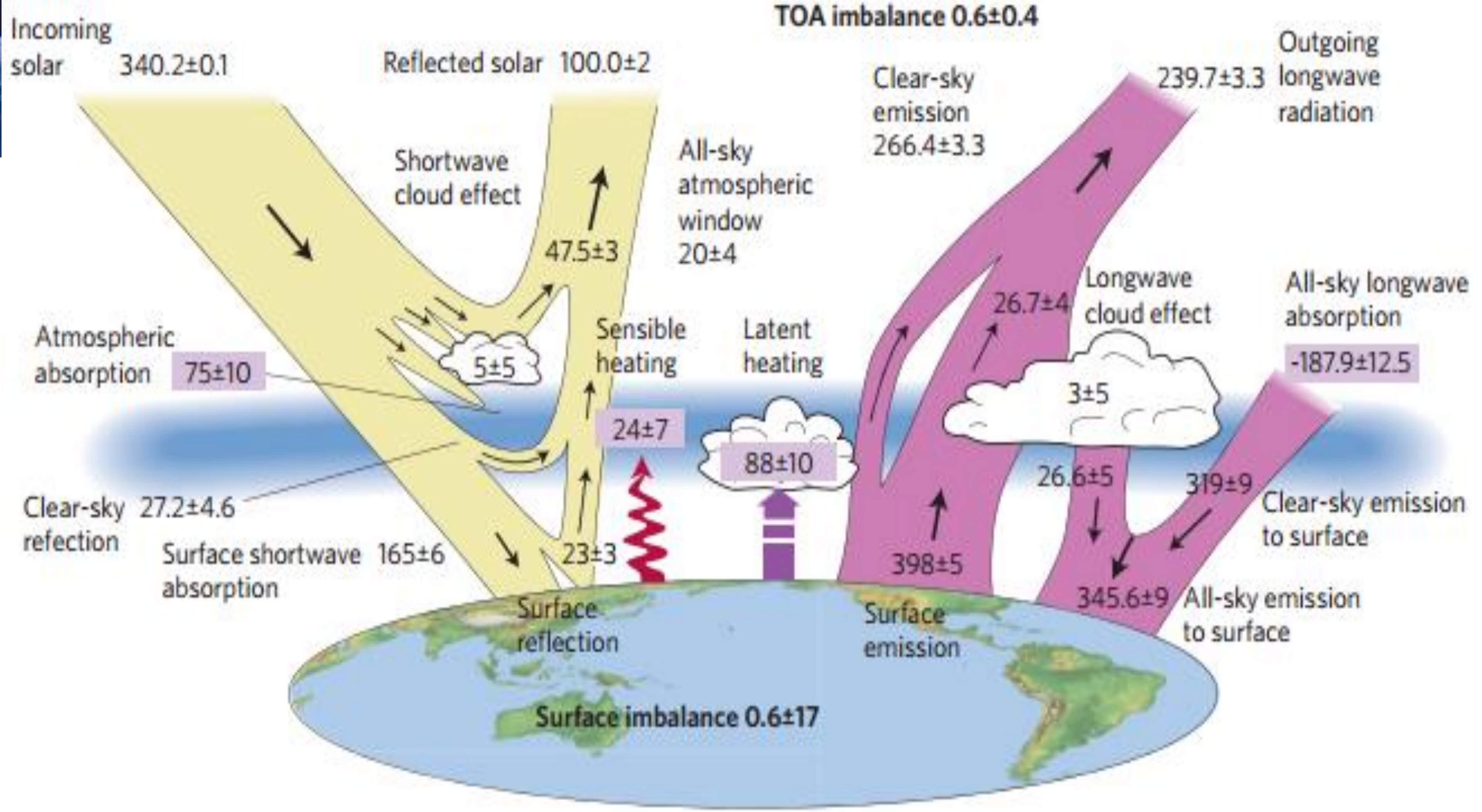

The global annual mean energy budget of Earth for the approximate period 2000–2010. All fluxes are in Wm-2. Solar fluxes are in yellow and infrared fluxes in pink. The four flux quantities in purple-shaded boxes represent the principal components of the atmospheric energy balance.(Stephens et al., 2012)

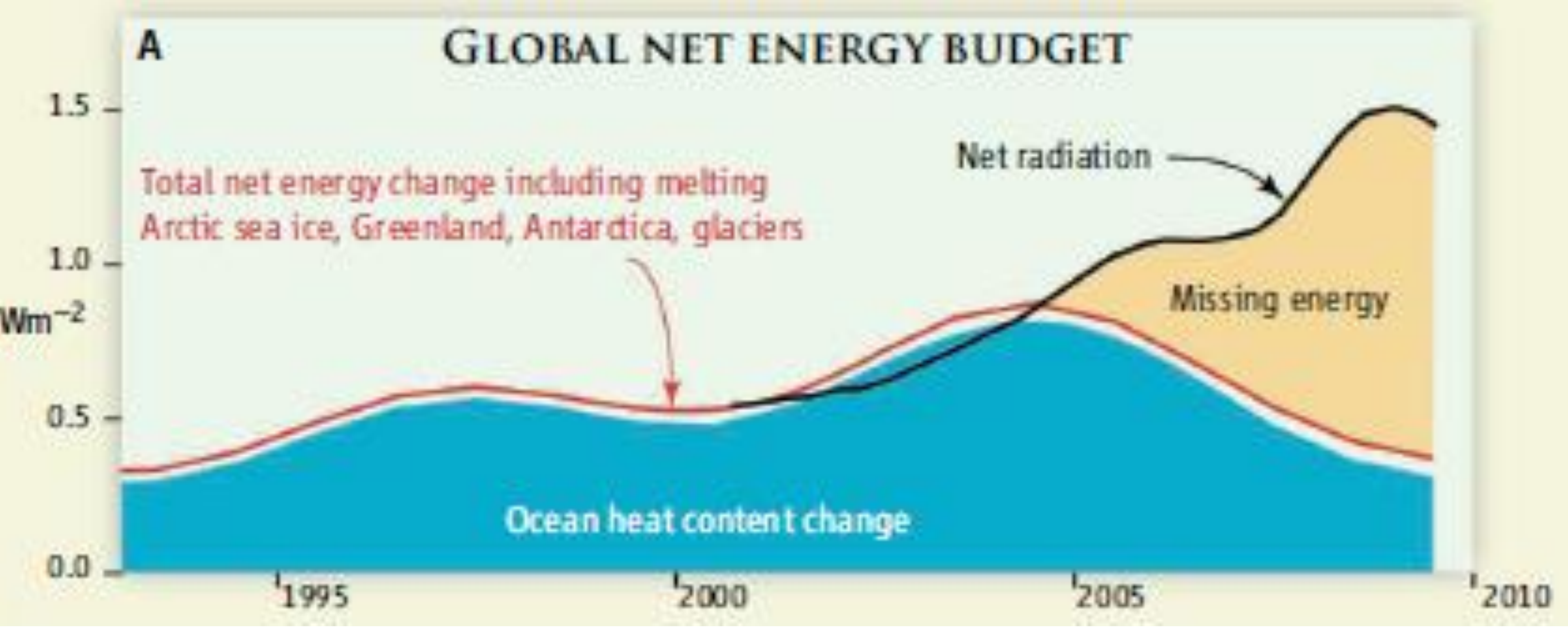

Trenberth, *Science*, 2010

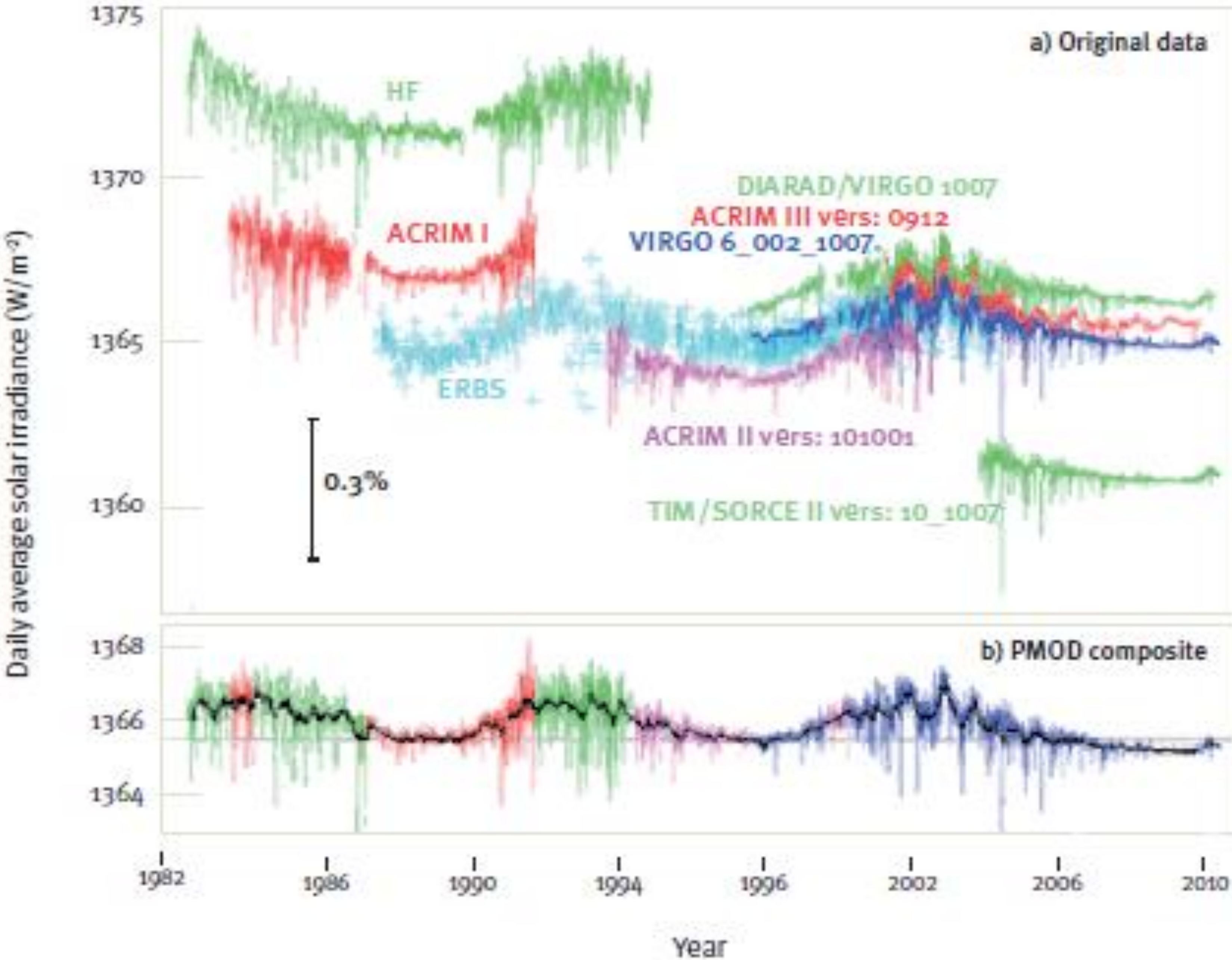

Figure 10. (a) Daily-averaged total solar irradiance (Wm^{-2}) from 1978 to present: all measurements made from satellites. (b) Composite record obtained by inter-calibration of the data from the individual instruments[16].

TABLE 1. Global mean clear- and all-sky SW, LW, and net TOA radiative fluxes, solar irradiance, and CRE for satellite-based data products (units in W m^{-2}).

Product name	ERBE S-4	CERES ES-4 Ed2_rev1	CERES SRBAVG-nonGEO Ed2D_rev1	CERES SRBAVG-GEO Ed2D_rev1	GEWEX SRB Version 2.86	ISCCP FD
Time period	02/85 – 01/89			03/00 – 02/2005		
Solar irradiance	341.3	341.3	341.3	341.3	341.8	341.5
LW (All sky)	235.2	239.0	237.7	237.1	240.4	235.8
SW (All Sky)	101.2	98.3	96.6	97.7	101.7	105.2
Net (All Sky)	4.9	4.0	7.0	6.5	−0.3	0.5
LW (Clear Sky)	264.9	266.6	266.4	264.1	268.1	262.3
SW (Clear Sky)	53.6	49.3	51.2	51.1	54.5	54.2
Net (Clear Sky)	22.8	25.4	23.7	26.2	19.2	25.0
LW CRE	29.7	27.6	28.7	27.0	27.7	26.5
SW CRE	−47.6	−49.0	−45.4	−46.6	−47.2	−51.0
NET CRE	−17.9	−21.4	−16.7	−19.7	−19.5	−24.5

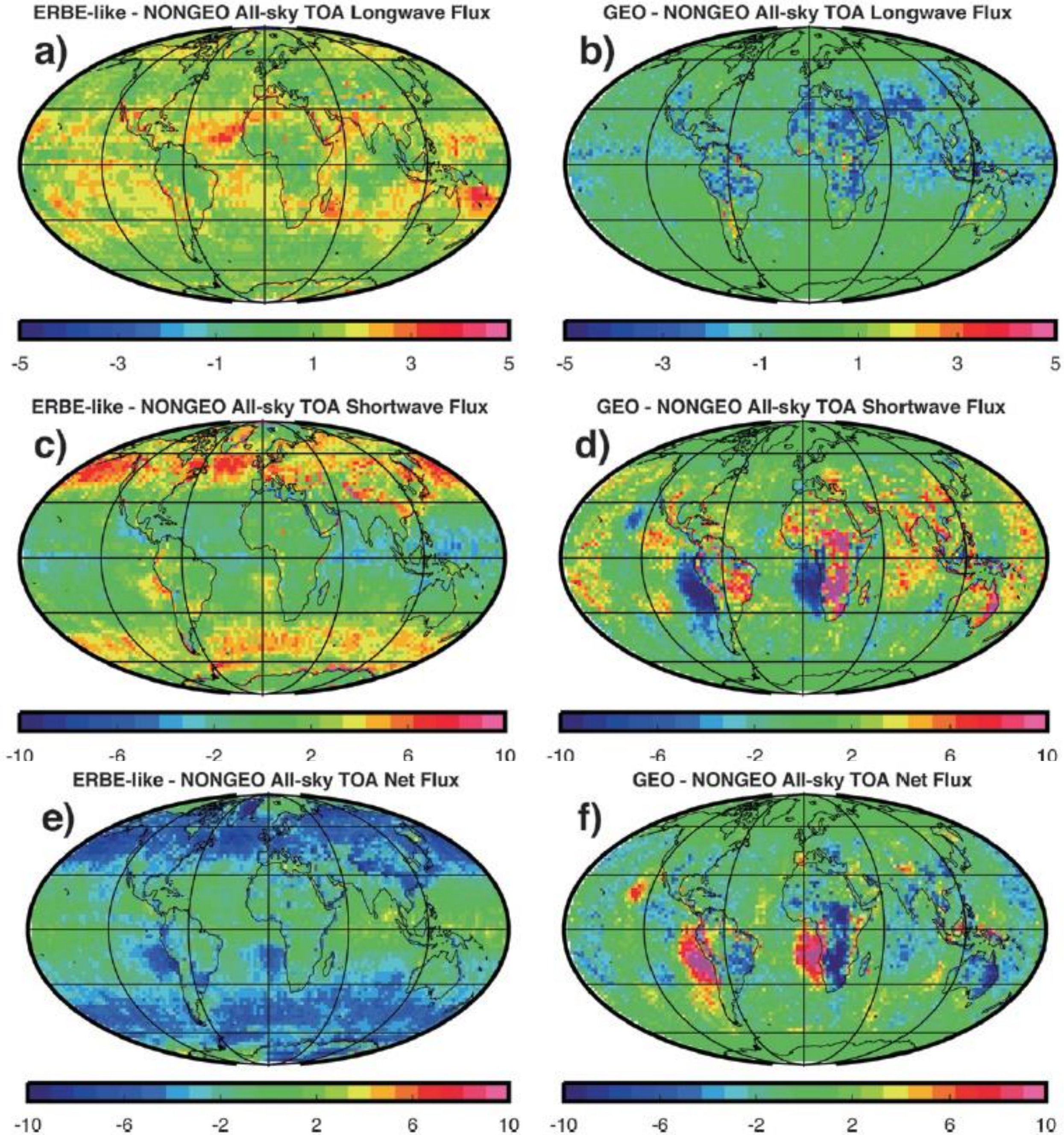

FIG. 1. Annual mean TOA flux difference between (left) CERES ERBE-like and CERES SRBAVG-nonGEO and (right) CERES SRBAVG-nonGEO and SRBAVG-GEO for (a), (b) LW; (c), (d) SW; and (e), (f) net for the year 2002.

Flux (Wm^{-2})	NASA/GEWEX SRB Release 3.0 (NASA LaRC) *24-Year Mean (1984-2007)*		Trenberth et al. (2009) CERES/ CCM3	Zhang and Rossow et al. (2004) *21-Year Mean (1984-2004)*	Wild (2008) IPCC AR4 Models
	Main Models	QC Models			
SRF SW Down	188.6	182.1	184	189.2	
SRF SW Net	166.6	159.5	161	165.9	161.8
SRF LW Down	343.8	347.5	333	343.8	337.5
SRF LW Net	-52.6	-51.2	-63	-49.6	-55.6
SRF Total Net	114.0	108.3	98	116.3	106.2
SRF SW CRF	-58.9	-61.9	---	-53.0	-57.2
SRF LW CRF	33.5	34.3	---	29.5	
SRF Total CRF	-25.4	-27.6	---	-23.5	
TOA SW Net	240.4	—	239	236.5	
TOA LW Net	-237.8	—	-239	-233.9	-233.7
TOA SW CRF	-47.5	—	---	-50.0	-50.6
TOA LW CRF	27.4	—	---	25.8	
TOA Net CRF	-20.1	—	---	-24.2	

Table 1. 24-year (1984–2007) global averaged radiative flux components at the surface (SRF) and TOA from SRB Release 3.0. The quality-check (QC) algorithms provide estimates of surface fluxes. Fluxes from ISCCP FD (Zhang and Rossow et al., 2004), Trenberth et al. (2009), and Wild (2008) are included for comparison. CRF: Cloud Radiative Forcing. The annual averaged total solar irradiance: F0=S0/4 where S0 is the solar constant. S0=1365 Wm^{-2} for Trenberth et al. results and 1367 Wm^{-2} for all others.

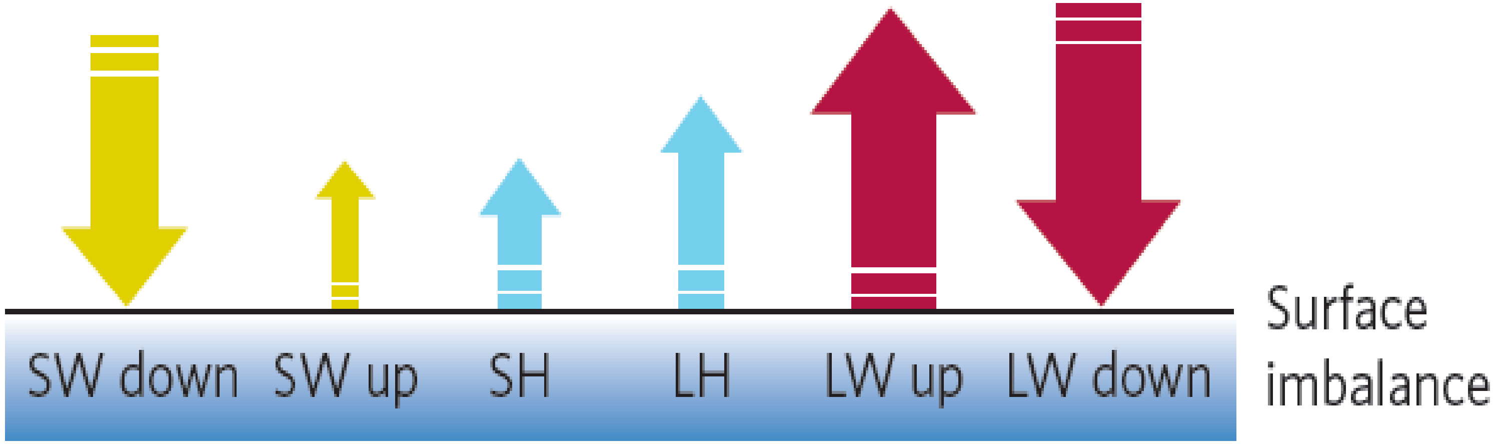

	SW down	SW up	SH	LH	LW up	LW down	Surface imbalance
Observations	188±6	23±3	24±7	88±10	398±5	345.6±9	0.6±17
CMIP5							
Min	181.9	21.1	17.6	78.4	391.9	326.4	
(Mean)	(190.3)	(24.9)	(20.9)	(85.8)	(397.5)	(339.7)	
Max	196.2	30.3	27.8	93.6	398.1	347.0	

Observed and climate model deduced energy fluxes and uncertainties (all in Wm-2) at the surface (Stephens et al., 2012). 'SW in' and 'SW out' refer to the incoming and outgoing (reflected) solar fluxes at the top-of-atmosphere (TOA) and 'LW out' is the outgoing longwave radiation. Similarly 'SW down' and 'SW up' refer to downward and upward (reflected) solar fluxes at the surface, and 'LW up' and 'LW down' refer to the upward emitted flux of longwave radiation from the surface and the downward longwave flux emitted from the atmosphere to the surface, respectively. SH and LH refer to latent and sensible heat fluxes.

the 1991 Mt. Pinatubo Eruption

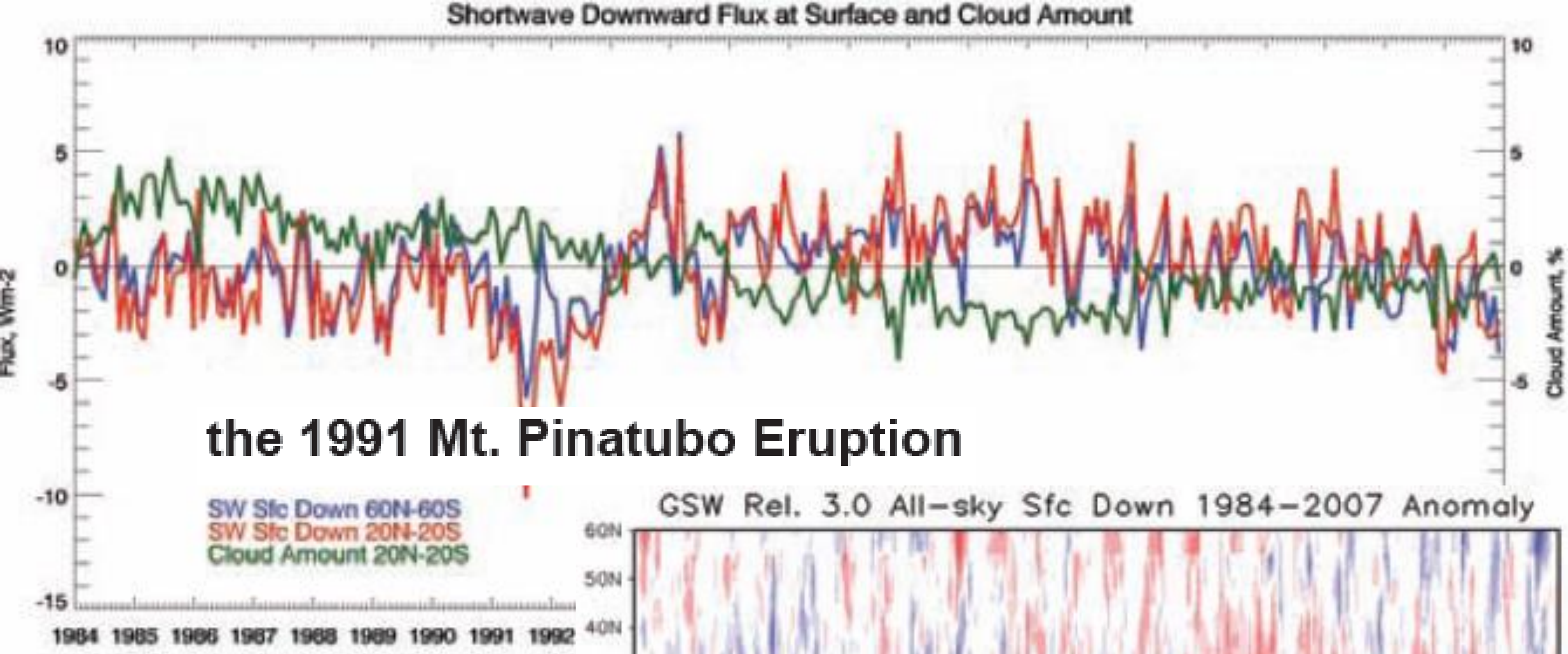

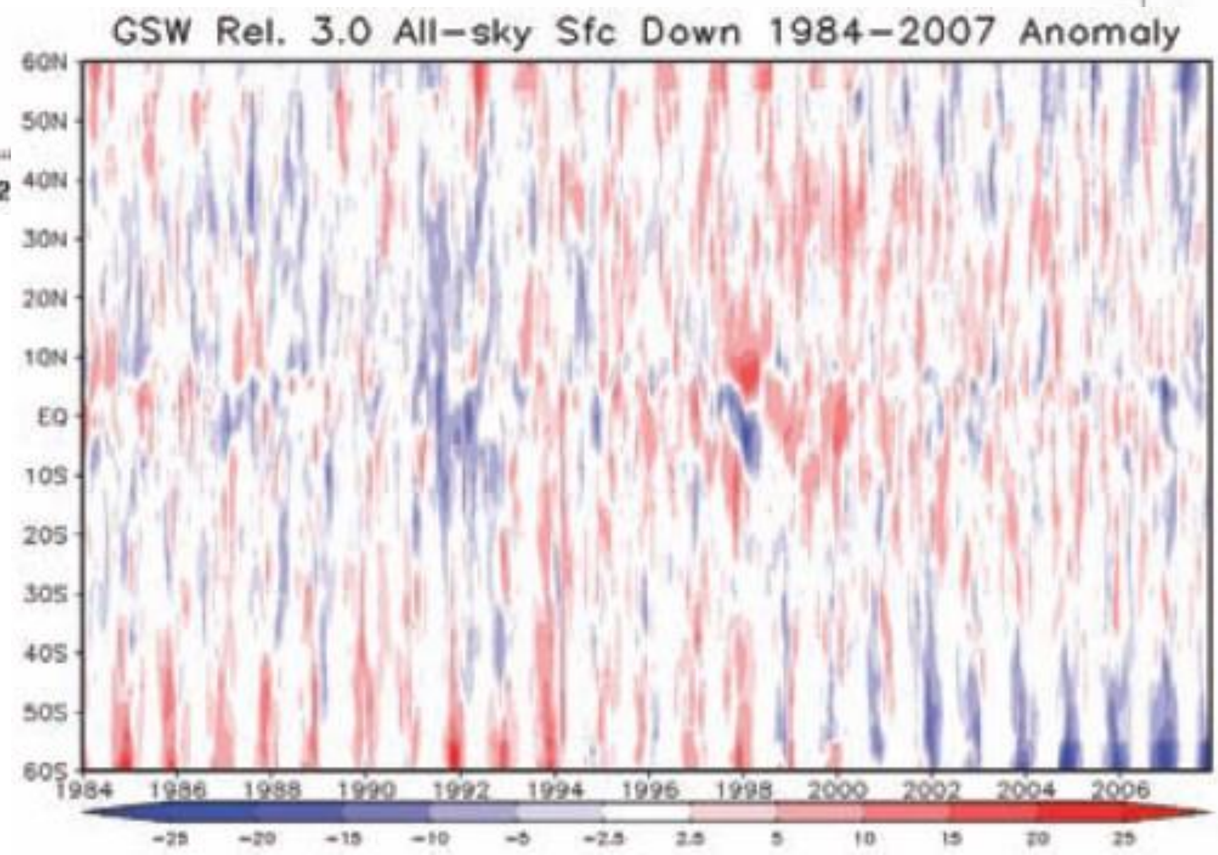

the 24-year time series for the 20 °S–20 °N and the 60 °S–60 °N zonally averaged deseasonalized flux anomalies for the shortwave, the deasonalized anomalies of the same zones for the cloud amount from ISCCP and the time-latitude cross-sections (Hovmöller plots) for the deseasonalized SW anomalies

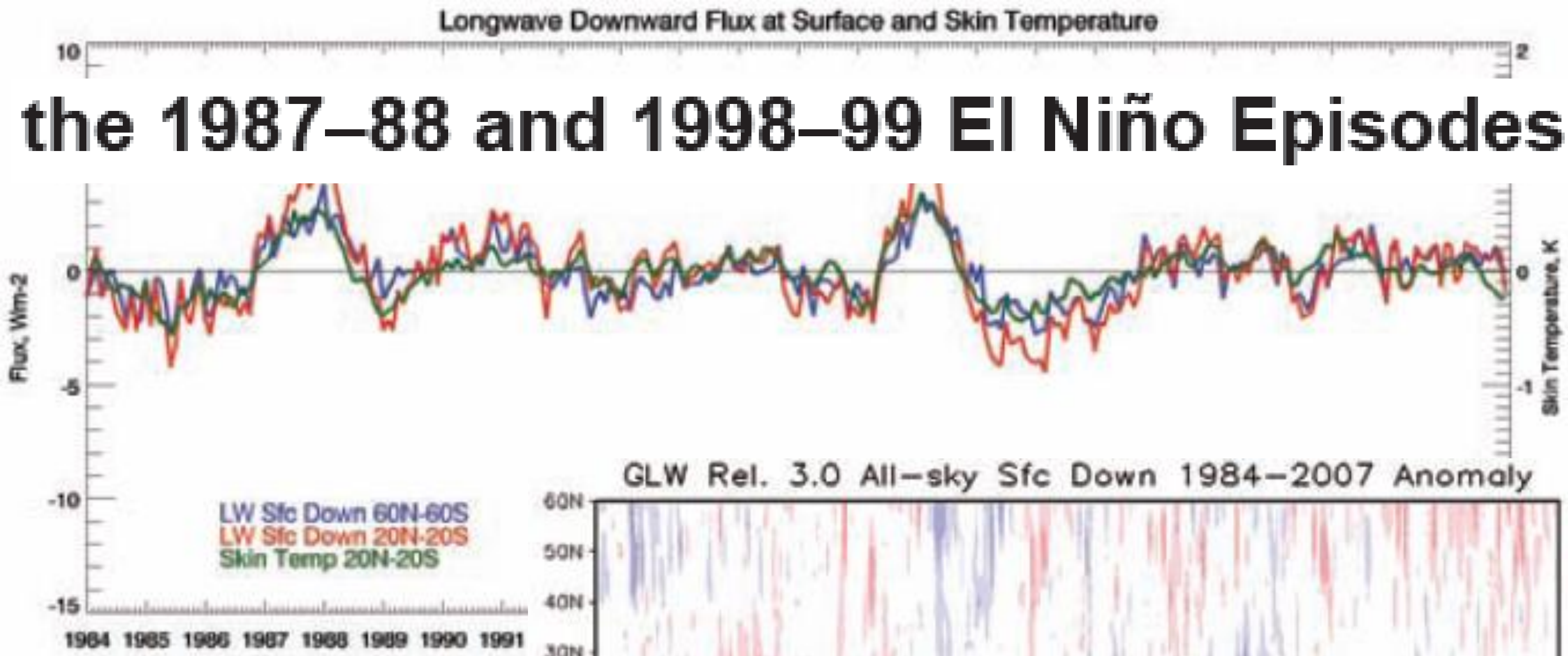

the 1987–88 and 1998–99 El Niño Episodes

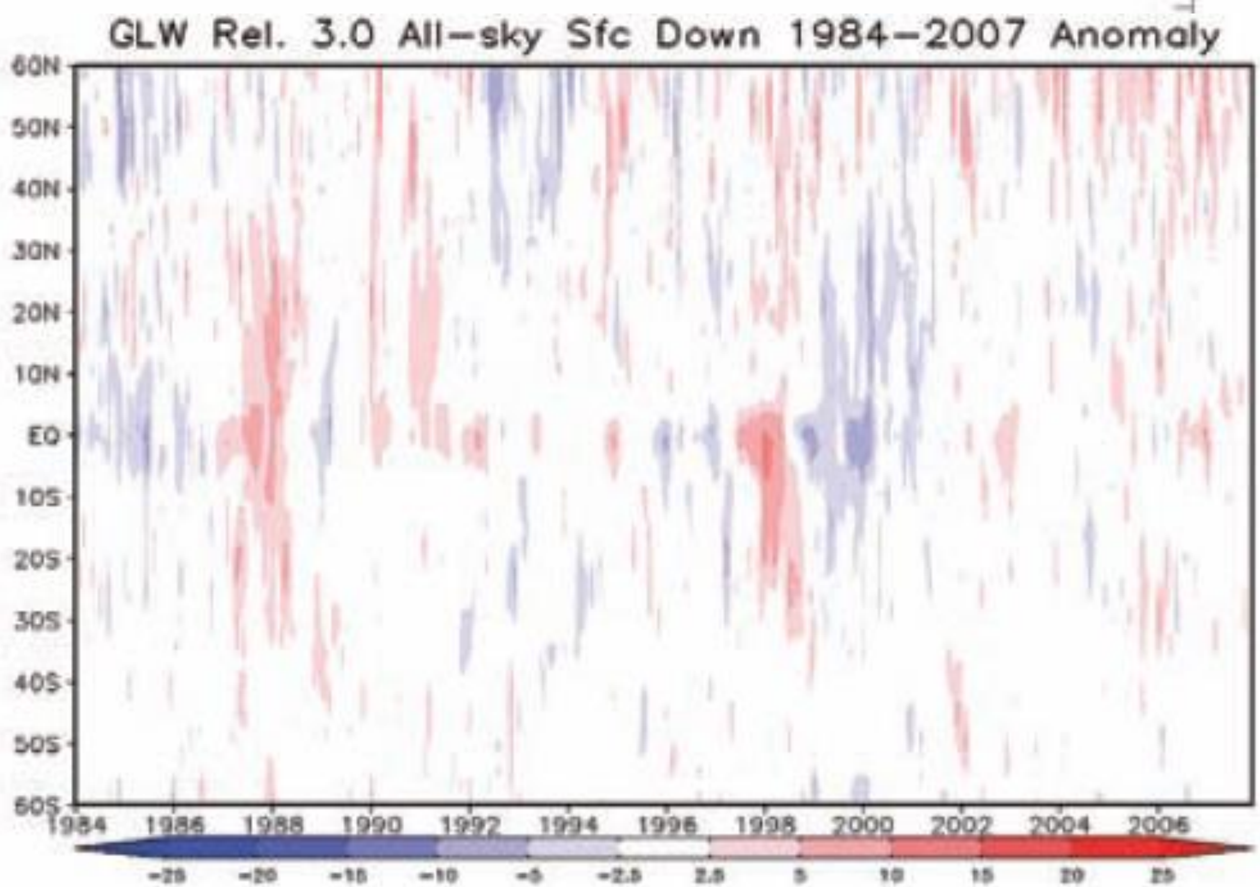

the 24-year time series for the 20°S–20°N and the 60°S–60°N zonally averaged deseasonalized flux anomalies for the longwave, the deasonalized anomalies of the same zones for the cloud amount from ISCCP and the time-latitude cross-sections (Hovmöller plots) for the deseasonalized LW anomalies

提纲

Liang

- 背景
- 下行太阳辐射/天空”变亮”与”变暗”
- 反照率
- 下行长波辐射
- 温度，发射率和上行长波辐射
- ET

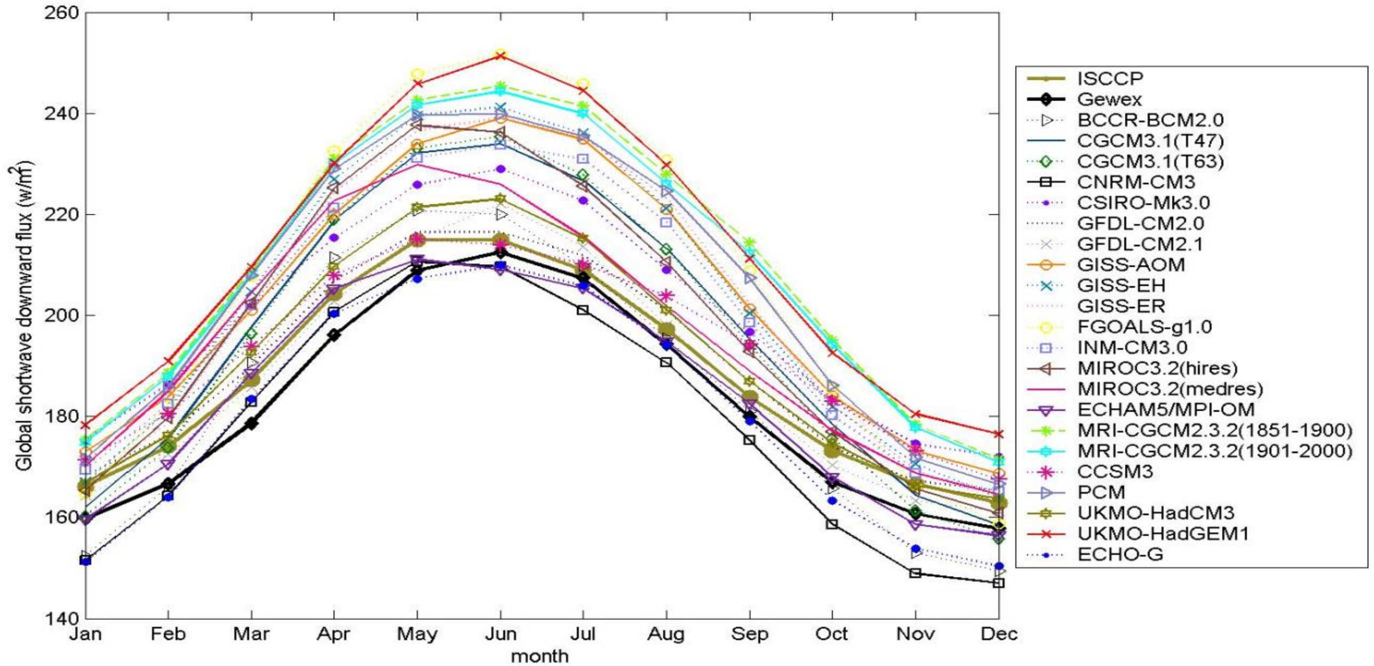

IPCC AR4 GCM model simulations and two satellite products

Table 1 Estimated averaged Insolation over land surfaces (Wm^{-2})

dataset	ISCCP-FD [125]	NRA [125]	ERA-40 [125]	JRA [125]	Trenberth et al. [125]	AMIPII GCMs mean [140]	GEBA mean [140]	IPCC AR4 GCM mean	GEWEX
Feb. 1985- April 1989	190.1	224.1	177.2	206.4		178	169	175	
Mar 2000 – May 2004	188.8	225.4	-	207.4	184.7				182.4

Liang, S., K. Wang, and X. Zhang, M. Wild, (2010), Review of estimation of land surface radiation and energy budgets from ground measurements, remote sensing and model simulation, *IEEE Journal of Special Topics in Applied Earth Observations and Remote Sensing*, 3:225-240.

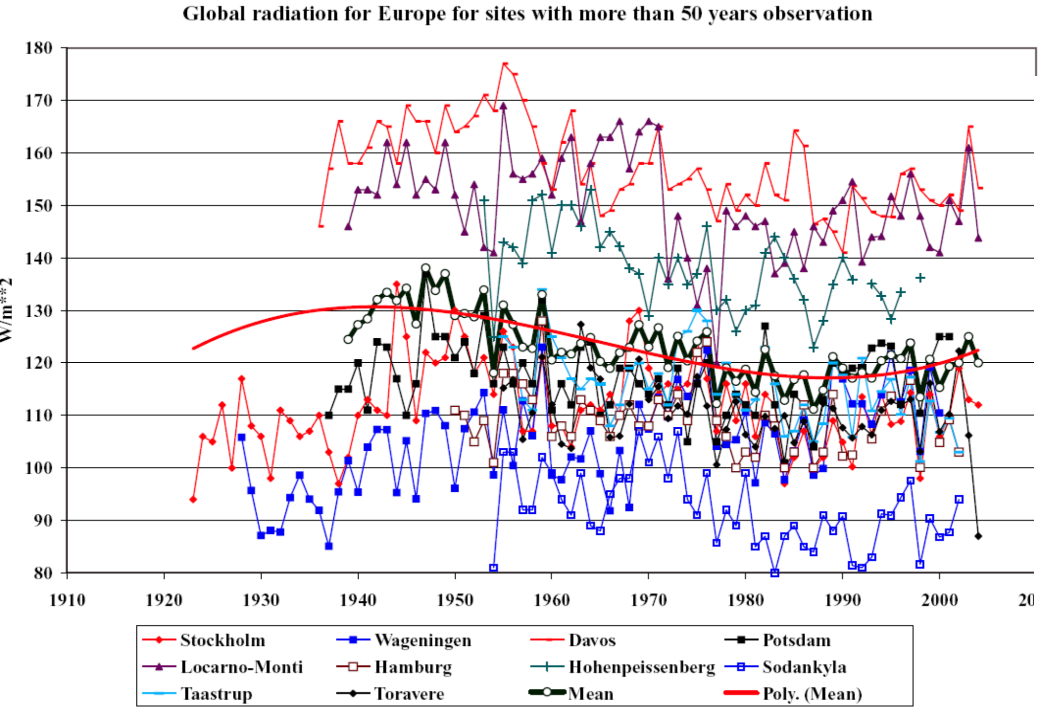
Global radiation for Europe for sites with more than 50 years observation
W/m**2
Stockholm
Wageningen
Davos
Potsdam
Locarno-Monti
Hamburg
Hohenpeissenberg
Sodankyla
Taastrup
Toravere
Mean
Poly. (Mean)

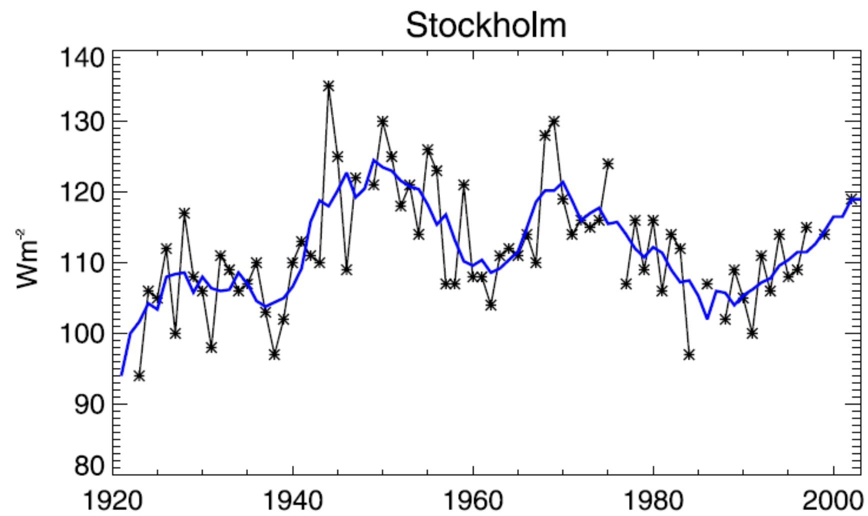
Stockholm
Wm^{-2}

“全球变暗”

“全球变亮”

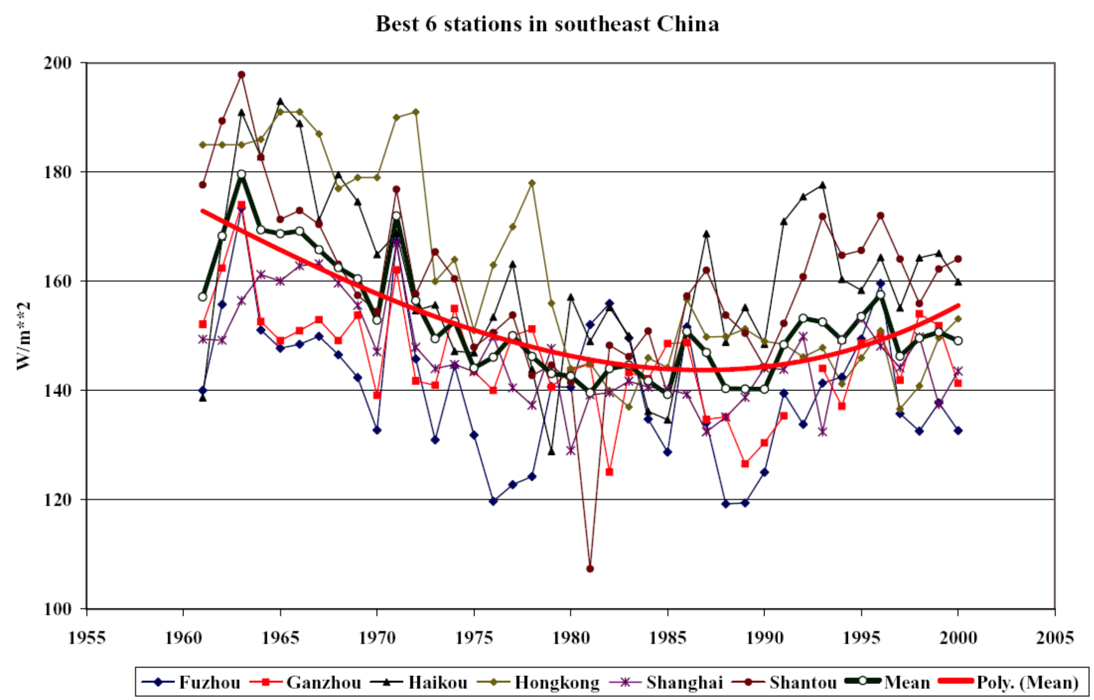
Best 6 stations in southeast China
W/m**2
Fuzhou
Ganzhou
Haikou
Hongkong
Shanghai
Shantou
Mean
Poly. (Mean)

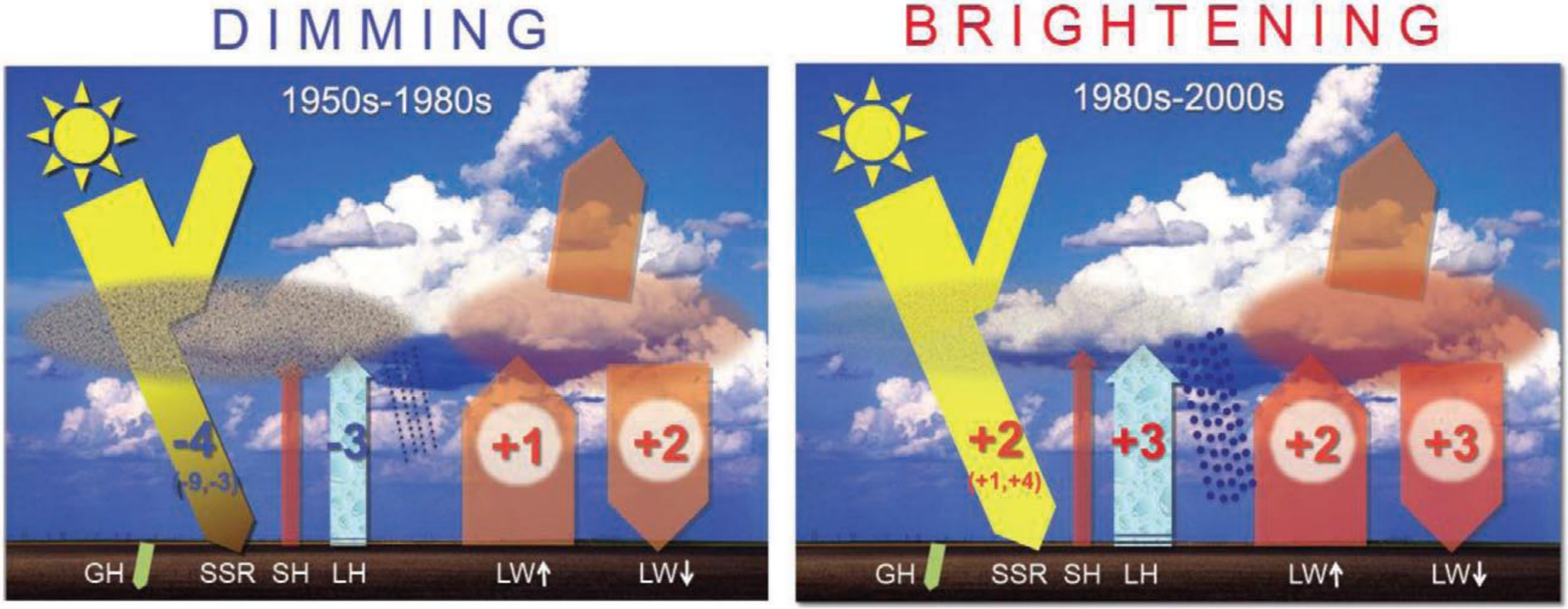

FIG. 1. Schematic representation of "dimming" and "brightening" periods over land surfaces. (left) During dimming (1950s–80s) the decline in surface solar radiation (SSR) may have outweighed increasing atmospheric downwelling thermal radiation (LW↓) from enhanced greenhouse gases and effectively counteracted global warming, causing only little increase in surface thermal emission (LW↑). The resulting reduction in radiative energy at Earth's surface may have attenuated evaporation and its energy equivalent, the latent heat flux (LH), leading to a slowdown of the water cycle. (right) With the transition from dimming to brightening (1980s–2000s), the enhanced greenhouse effect has no longer been masked, causing more rapid warming, stronger evaporation/LH, and an intensification of the water cycle. Values denote best estimates of overall changes in surface energy fluxes over both periods in W m^{-2} (ranges of literature estimates for SSR dimming/brightening in parentheses). Positive (negative) numbers, shown in red (blue), denote increasing (decreasing) magnitudes of the energy fluxes in the direction indicated by the arrows. Changes in ground heat flux (GH) and sensible heat flux (SH) are considered small compared to the above mentioned flux changes.

太阳辐射短期变化的原因

Liang

- 大气外部太阳辐射变化：反映在地质年代尺度上，每11 年太阳黑子变化只导致 ±1 Wm-2
- 大气内部条件的变化
  - 水汽： 10%变化导致0.5%太阳辐射下降。每1 ℃ 增温导致大概5%的水汽量变化
  - 云
  - 气溶胶

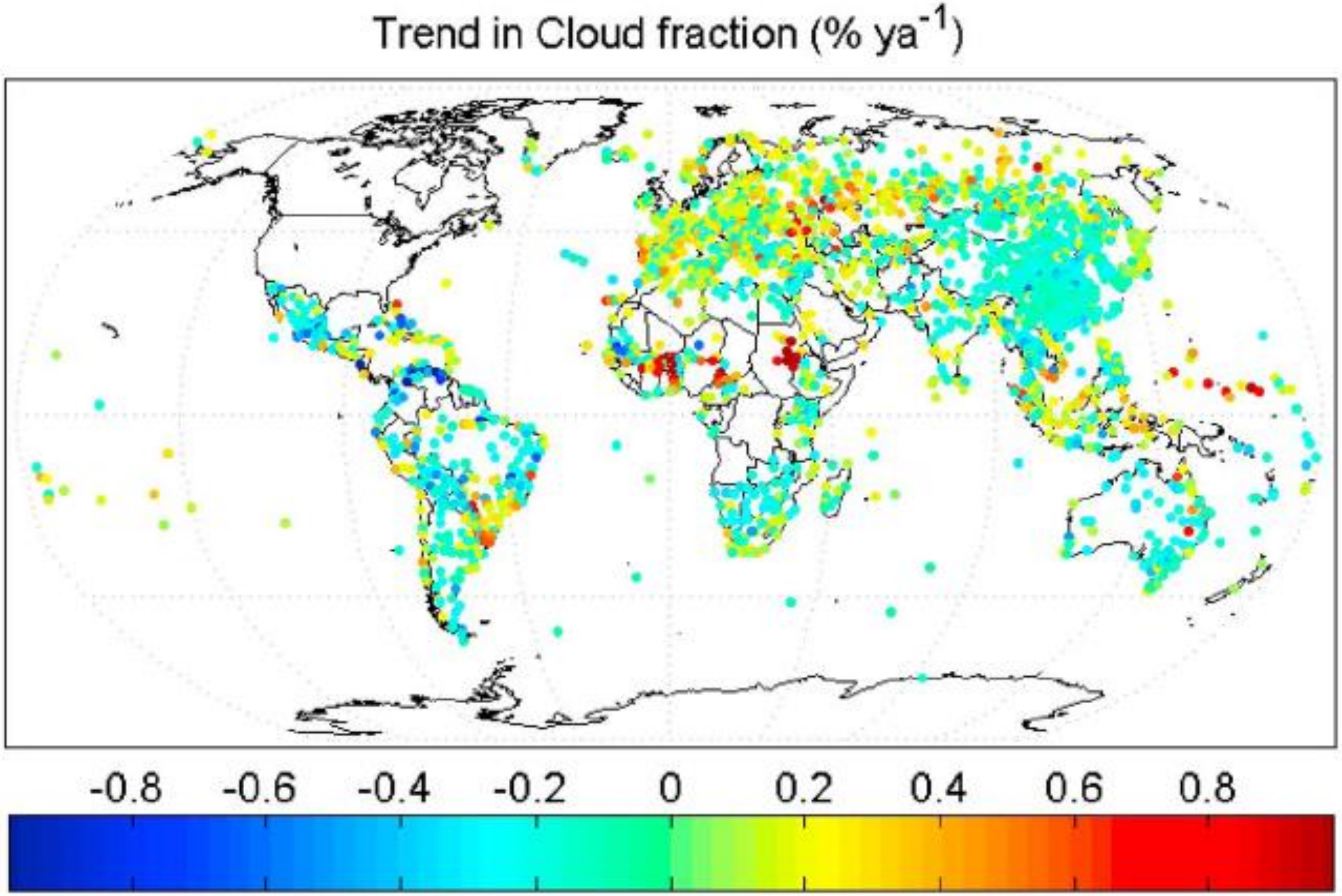

Figure 6. Linear trend of daily total cloud coverage from 1973 to 2008. The monthly total cloud cover fraction anomaly is derived and used to calculate the linear trend using the Mann-Kendall trend test method, and only stations that pass the 95% significance level in the Mann-Kendall trend test are shown. Some sites over North America and some European countries changed the observational method from human visual observations to instrument observations during the 1990s and are excluded because they show obvious discontinuities in total cloud coverage.

Wang, K., B. Dickinson, M. Wild, **S. Liang**, (2010), Evidence for Decadal Variation in Global Terrestrial Evapotranspiration between 1982 and 2002, Part 1: Model Development", *Journal of Geophysical Research - Atmospheres* 115, D20112

Wang, K., R. Dickinson and S. Liang, (2009), Clear sky visibility has decreased over land globally from 1973 to 2007,*Science*, 323, 1468-1470

Liang

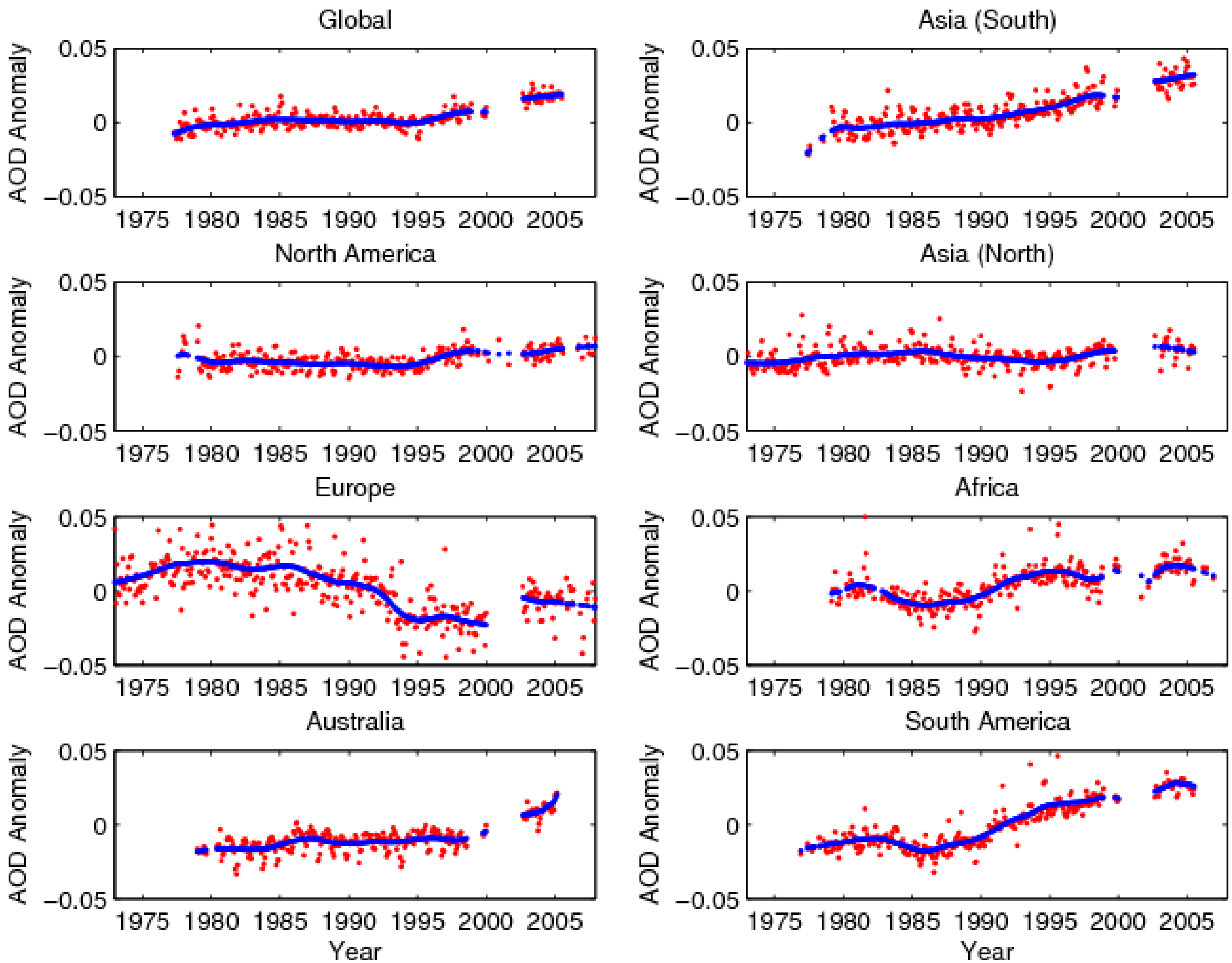

Observed tendencies in surface solar radiation

	1950s-1980s	1980s-2000	after 2000
USA	-6	5	8
Europe	-3	2	3
China/Mongolia	-7	3	-4
Japan	-5	8	0
India	-3	-8	-10

FIG. 2. Changes in surface solar radiation observed in regions with good station coverage during three periods. (left column) The 1950s–1980s show predominant declines ("dimming"), (middle column) the 1980s–2000 indicate partial recoveries ("brightening") at many locations, except India, and (right column) recent developments after 2000 show mixed tendencies. Numbers denote typical literature estimates for the specified region and period in W m^{-2} per decade. Based on various sources as referenced in Wild (2009).

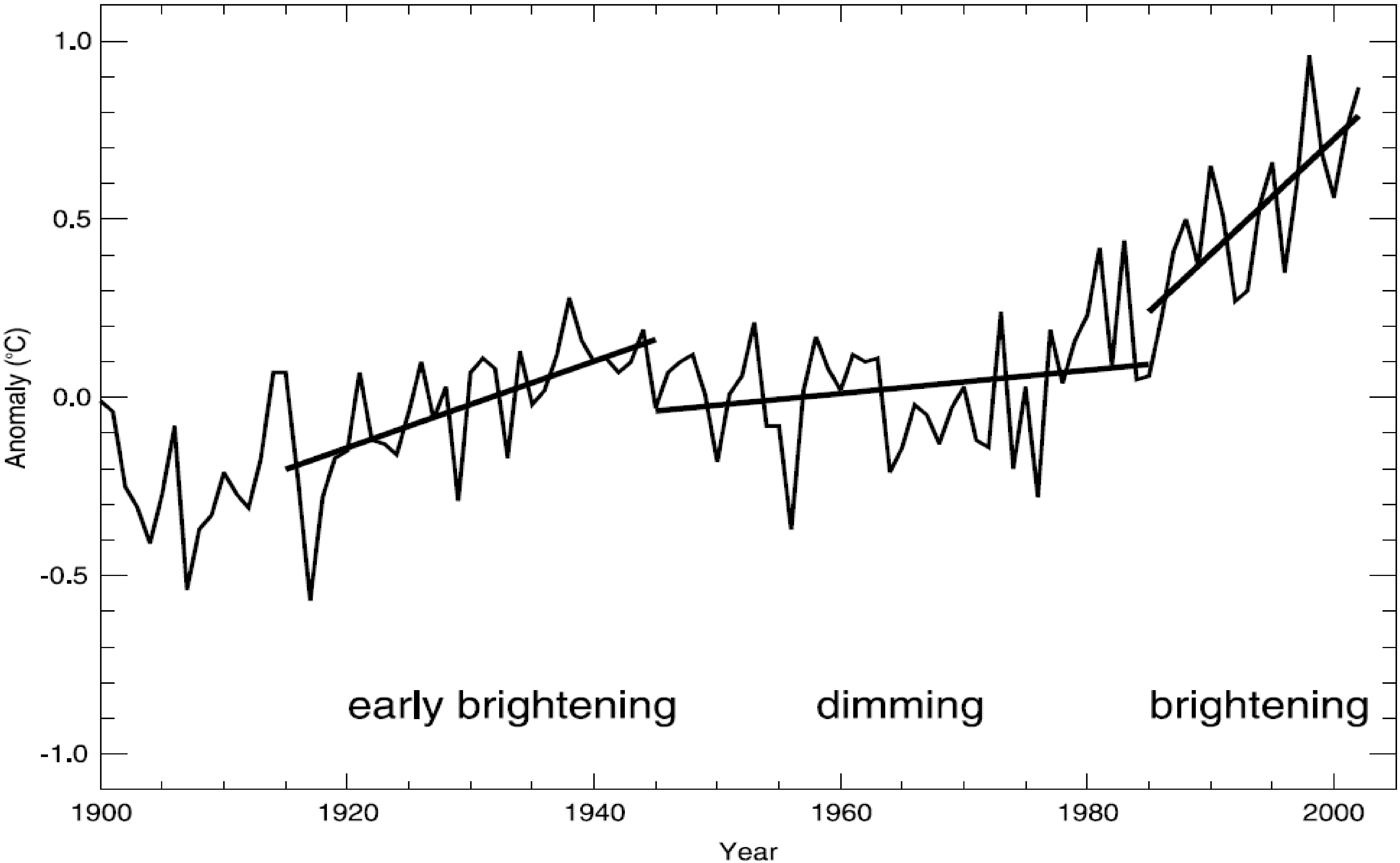

Figure 9. Observed 2-m temperature anomalies over global land surfaces during the 20th century. There is indication for a suppression of greenhouse-induced warming through "global dimming" between the 1950s and 1980s, and an enhancement through "brightening" between the 1920s and 1940s as well as from the 1980s onward. Anomalies with respect to the 20th century average. Units are °C. Adapted from *Wild et al.* [2007].

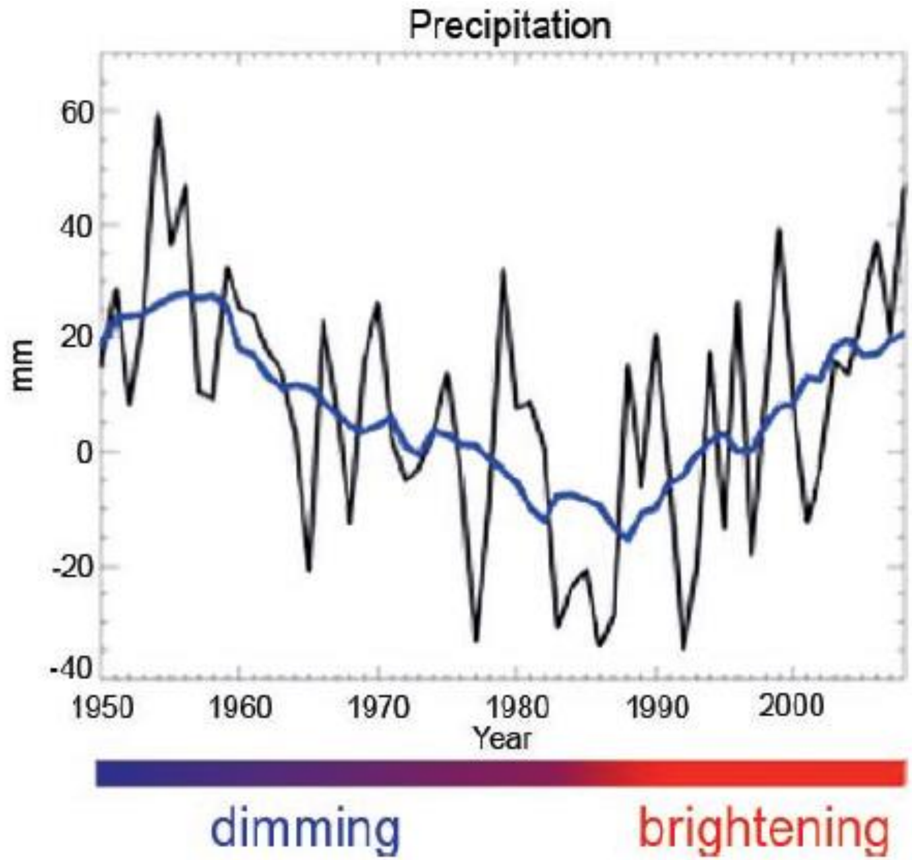

FIG. 5. Observational estimates of annual precipitation anomalies from 1950–2008 over the NH land masses. Data are from the Global Historic Climate Network (Peterson and Vose 1997). Reference period for anomalies is 1961–90; 11-yr running mean in blue. Units are mm.

Impacts of diffuse radiation on LUE & EF

- Clouds and aerosols increase the diffuse component of the solar radiation;
- We are producing both direct and diffuse insolation/PAR;
- Wang, K, R. E. Dickinson, and S. Liang (2008). Observational evidence on the effects of clouds and aerosols on net ecosystem exchange and evapotranspiration. *Geophysical Research Letter*, 35, doi:10.1029/2008GL034167
  - *Light Use Efficiency (LUE)* is 19.4% and 203% larger for patchy clouds, and thick clouds than those for clear skies while *LUE* is about -6% for aerosols or thin clouds than those for clear skies.
  - *Evaporative Fraction (EF)* is 15.4%, 17.9% and 23.2% larger for aerosols or thin clouds, patchy clouds, and thick clouds than those for the clear sky

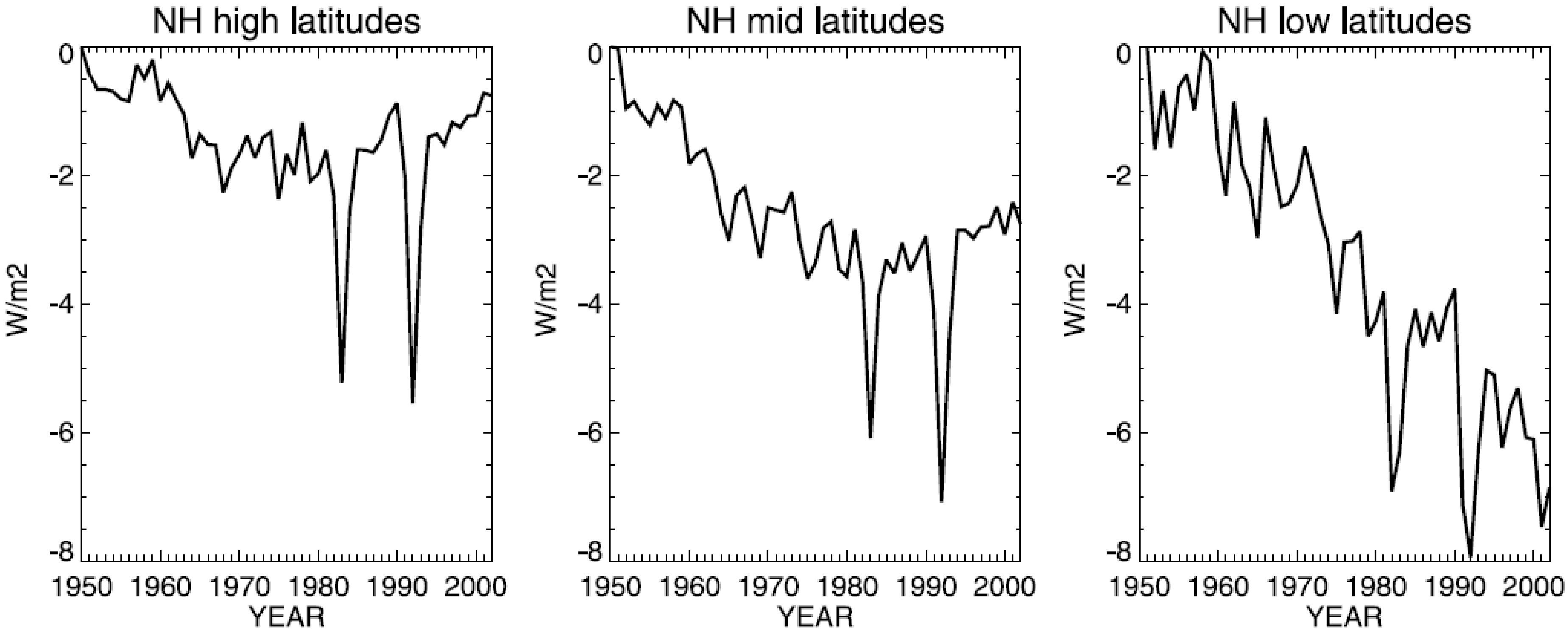

Figure 5. Simulated annual clear-sky surface solar radiation anomalies over the period 1950–2000 in different latitude belts of the Northern Hemisphere: High latitudes (60°N–90°N), middle latitudes (30°N–60°N), and low latitudes (0°–30°N). Simulations done with the aerosol-climate modeling system ECHAM5 HAM [*Stier et al.*, 2005, 2006]. Reference value is 1950. Units are W m^{-2}.

Current solar radiation products

Liang

- The ISCCP (International Satellite Cloud Climatology Project) solar radiation products at 280 km (1983-2000);
- The Global Energy and Water Cycle Experiment (GEWEX) SRB Release 2 has a spatial resolution of 1° x 1°;
- The Clouds and the Earth's Radiant Energy System (CERES) flux products at 140km;
- GCM reanalysis products (> 1°)

Need for high spatial resolution products

Liang

- Current global radiation products have coarse spatial resolution (>1°) but fine temporal resolution (3 hours), primarily for atmospheric modeling
- Those products do not account for many local features, such as urbanization.
- Land applications require high spatial resolution (~1km) but reasonable temporal resolution (e.g., daily)
  - Ecosystem modeling (say, MODIS NPP product) requires high-resolution products (1km)
  - Hydrological modeling (ET) at 1km
  - Other applications on environmental monitoring (e.g., drought detection)

下行短波辐射

产品	空间分辨率	时间分辨率（小时）	时间范围
ISCCP	280km	3	1983-2008
GEWEX-SRB	1°	3	1983-2007
CERES	140km	3	1997-目前
GLASS	5km	3	2008-2010

WMO （世界气象组织）要求

	理想误差 (Wm^{-2})	最大误差 (Wm^{-2})	理想空间分辨率 (km)	最小空间分辨率 (km)
数值天气预报	1	20	10	100
农业气象	N/A	N/A	1	20
气候	5	10	25	100

R^2, Bias, Relative Bias of Satellite Products, STD and Relative STD of the Differences Between Observed and Satellite Surface Downwelling Shortwave Irradiance (Wm^{-2}) at All Sites From 2000–2002

Sites	GEWEX-SRB(AllSky2000-2002)			ISCCP-FD (AllSky2000-2002)			CERES-FSW(AllSky2000-2002)		
	R^2	Bias[a] (%)[b]	STD (%)	R^2	Bias (%)	STD (%)	R^2	Bias (%)	STD (%)
North America									
Bondville	0.91	-6.7(-2.1%)	78.0(25%)	0.89	-12.5(-4%)	83.7(27%)	0.85	14.0(2.7%)	103.2(20%)
Boulder	0.84	-13.5(-4.0%)	107.4(32%)	0.85	-1.9(-0.6%)	106.7(32%)	0.64	9.0(1.5%)	157.0(26%)
Desert_Rock	0.94	-14.2(-3.4%)	74.8(18%)	0.96	-16.2(-3.9%)	62.2(15%)	0.87	20.3(2.9%)	82.0(12%)
Fort_Peck	0.92	-14.6(-5.0%)	70.2(24%)	0.88	-6.5(-2.2%)	84.1(29%)	0.88	18.9(3.8%)	87.9(18%)
Goodwin	0.95	-0.6(-0.2%)	62.5(19%)	0.88	-1.3(-0.4%)	94.5(28%)	0.89	33.9(6.1%)	87.2(16%)
Penn_State	0.92	-0.6(-0.2%)	69.4(24%)	0.90	2.0(0.7%)	78.6(27%)	0.87	37.9(7.8%)	98.7(20%)
Mean	0.91	-8.4(-2.5%)	77.1(24%)	0.89	-6.1(-1.7%)	85.0(26%)	0.83	22.3(4.1%)	102.7(19%)
Tibetan Plateau									
Amdo	0.84	-1.8(-0.5%)	116.9(31%)	0.80	-20.6(-5.4%)	128.5(34%)	0.35	46.5(6.7%)	165.9(24%)
D66	0.87	15.9(4.8%)	88.8(27%)	0.88	24.7(7.5%)	87.7(27%)	0.57	74.9(13.0%)	124.7(22%)
D110	0.85	-44.6(-10%)	131.0(30%)	0.87	-52(-12.1%)	122.8(29%)	0.21	-58.7(-6.8%)	273.9(32%)
Naqu	0.83	-18.0(-4.7%)	125.2(32%)	0.84	-25.9(-6.7%)	121.7(31%)	0.25	10.0(1.4%)	220.6(31%)
Toutouhe	0.86	-18.5(-4.9%)	107.3(29%)	0.86	-15.1(-4.0%)	110.7(30%)	0.36	40.3(6.0%)	189.0(28%)
Mean	0.85	-13.4(-3.1%)	113.8(30%)	0.85	-18.0(-4.1%)	114.4(30%)	0.35	22.6(4.1%)	194.8(27%)
Southeast Asia									
Sukothai	0.80	-90.2(-22%)	153.8(38%)	0.83	-38.9(-9.7%)	138.1(34%)	0.40	-118.8(-15%)	204.9(26%)
TakEgat	0.71	8.2(2.6%)	147.1(47%)	0.77	77.1(24.6%)	141.6(45%)	0.42	107.0(19%)	161.3(28%)
Kogma	0.74	45.8(14.7%)	139.6(45%)	0.77	69.4(23.0%)	137.6(46%)	0.46	125.1(22%)	170.0(30%)
Bukit	0.72	43.4(12.8%)	122.5(36%)	0.68	108.7(32%)	146.1(43%)	0.44	107.5(20%)	161.5(30%)
Palangkaraya	0.79	20.5(5.3%)	113.9(29%)	0.78	65.6(17.1%)	123.0(32%)	0.64	130.7(24%)	110.4(20%)
Sakaerat	0.80	19.0(5.2%)	116.7(32%)	0.81	71.6(19.4%)	119.3(32%)	0.48	83.8(13.5%)	157.0(25%)
Mean	0.76	7.8(3.1%)	132.3(38%)	0.77	58.9(17.7%)	134.3(39%)	0.47	72.6(13.9%)	160.9(27%)

Gui, S., **S. Liang**, K. Wang, and L. Li, (2010), Validation of Three Satellite-Estimated Land Surface Downward Shortwave Radiation Datasets, *IEEE Geoscience and Remote Sensing Letters*,7(4):776-780

Japan									
Fujiyoshida	0.77	-10.7(-3.4%)	123.3(39%)	0.74	-15.4(-4.9%)	128.2(41%)	0.68	26.1(4.7%)	156.5(28%)
Mase	0.84	3.5(1.1%)	97.4(32%)	0.79	2.6(0.9%)	113.0(37%)	0.83	50.5(10.1%)	106.5(21%)
Takayama	0.83	1.7(0.6%)	104.9(37%)	0.81	27.1(9.5%)	109.9(39%)	0.79	106.1(23.3%)	133.5(29%)
Tomakomai	0.81	-2.0(-0.7%)	97.5(38%)	0.63	-6.4(-2.5%)	139.9(54%)	0.72	72.3(17.5%)	129.4(31%)
Teshio	0.77	39.7(17.2%)	107.8(47%)	0.73	4.6(2.0%)	111.3(48%)	0.70	77.4(22.2%)	136.3(39%)
Mean	0.80	6.4(3.0%)	106.2(39%)	0.74	2.5(1.0%)	120.5(44%)	0.74	66.5(15.6%)	132.4(30%)
Siberia									
Tiksi	0.75	-11.5(-7.3%)	85.2(55%)	0.82	-4.9(-3.4%)	71.9(50%)	0.82	12.8(5.9%)	81.0(37%)
Yakutsk	0.87	5.9(2.8%)	75.8(36%)	0.88	-0.02(-0%)	73.8(35%)	0.89	8.2(2.7%)	81.1(27%)
Mean	0.81	-2.8(-2.3%)	80.5(46%)	0.85	-2.5(-1.7%)	72.9(43%)	0.86	10.5(4.3%)	81.1(32%)
Amazon									
AbracosHill	0.82	-14.4(-3.7%)	114.3(29%)	0.85	23.3(6.0%)	108.2(28%)	0.67	4.6(0.7%)	115.7(18%)
AltaFloresta	0.85	-12.9(-3.4%)	112.0(30%)	0.87	0.7(0.2%)	107.3(28%)	0.73	5.6(0.8%)	109.1(16%)
Balbina	0.83	-4.6(-1.2%)	116.4(31%)	0.84	28.7(7.7%)	116.2(31%)	0.56	49.2(7.6%)	154.5(24%)
Belterra	0.89	1.2(0.3%)	92.9(26%)	0.83	16.0(4.5%)	120.2(34%)	0.54	74.4(12.1%)	138.8(23%)
Cuiaba	0.85	8.4(2.4%)	113.5(32%)	0.88	15.9(4.5%)	102.1(29%)	0.78	35.4(5.7%)	106.2(17%)
Rio_Branco	0.81	-6.1(-1.5%)	115.5(28%)	0.79	24.7(6.0%)	123.7(30%)	0.66	10.8(1.7%)	133.4(21%)
Mean	0.84	-4.7(-1.2%)	110.8(29%)	0.84	18.2(4.8%)	113.0(30%)	0.66	30.0(4.8%)	126.3(20%)
Greenland									
HumboldtGl	0.79	-19.3(-8.6%)	81.4(36%)	0.88	-30.0(-13%)	62.7(28%)	0.91	-7.8 (-2.8%)	54.8(20%)
NGRIP	0.80	-19.7(-8.3%)	91.3(38%)	0.85	-27.5(-11%)	78.8(33%)	0.90	-25.6(-8.1%)	64.9(20%)
Saddle	0.82	-22.9(-9.5%)	105.4(44%)	0.89	-29.5(-12%)	81.8(33%)	0.94	-1.7(0.5%)	69.1(20%)
Swiss Camp	0.79	-45.3(-20.2%)	97.6(43%)	0.87	-36.2(-16%)	80.2(36%)	0.89	-17.8(-5.7%)	77.3(25%)
Summit	0.87	-13.2(-5.5%)	80.3(34%)	0.91	-35.7(-15%)	72.3(30%)	0.90	-28.2(-8.5%)	73.0(22%)
Tunu-N	0.83	-20.1(-8.5%)	75.4(32%)	0.90	-40.3(-17%)	57.8(24%)	0.94	-18.2(-6.1%)	46.7(16%)
Mean	0.82	-23.4(-10.1%)	88.6(38%)	0.88	-33.2(-14%)	72.3(31%)	0.91	-16.6(-5.1%)	64.3(21%)
Total Mean	0.83	-5.5(-1.9%)	101.3(35%)	0.83	2.8(0.3%)	101.7(35%)	0.69	29.7(6.0%)	123.2(25.1%)

[a]Bias is calculated by satellite minus ground; [b]Relative bias is calculated by dividing bias by mean observation. Units are Wm^{-2}.

Gui, et al., *IEEE GRSL*, 2010

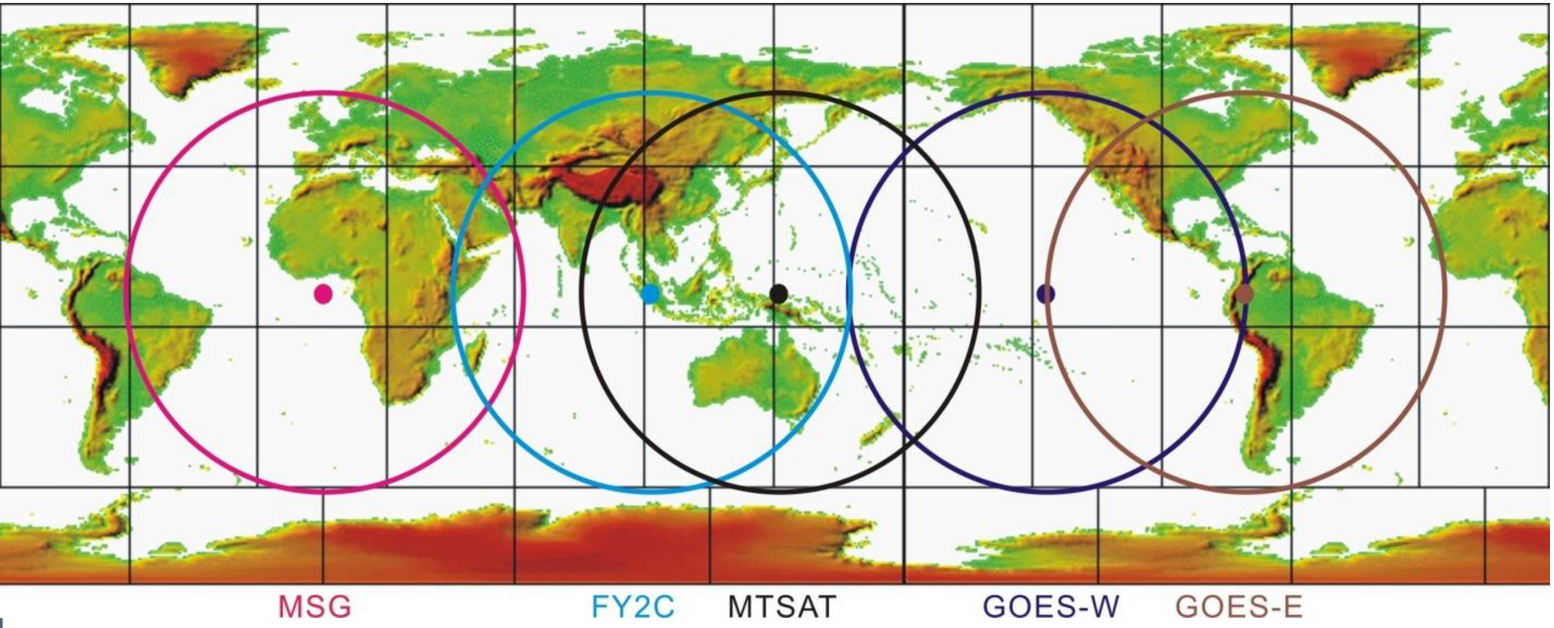

极地卫星:

MODIS

静止卫星:

GOES-W

GOES-E

MSG

MTSAT

FY2C

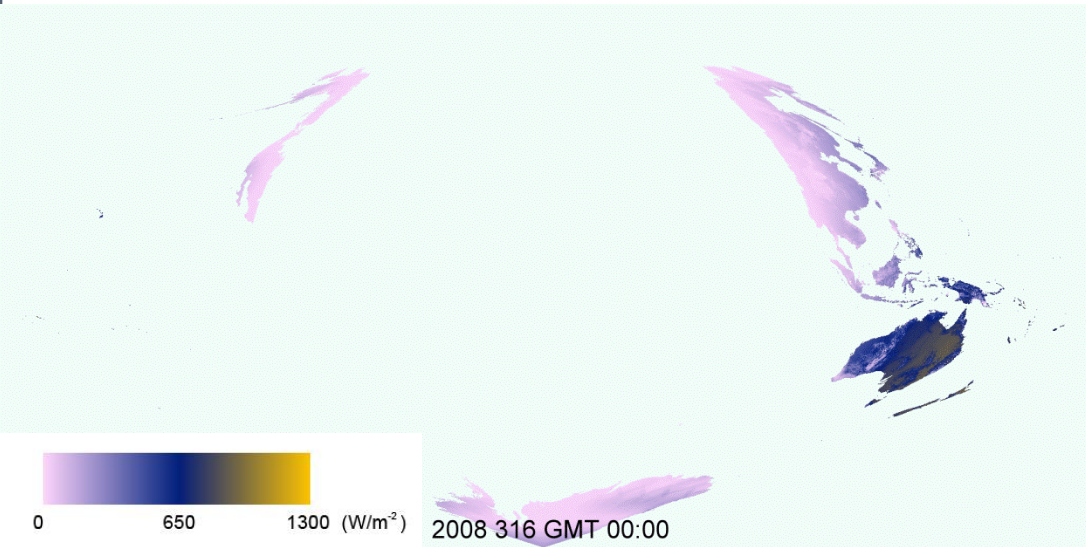

Insolation on Nov. 11, 2008

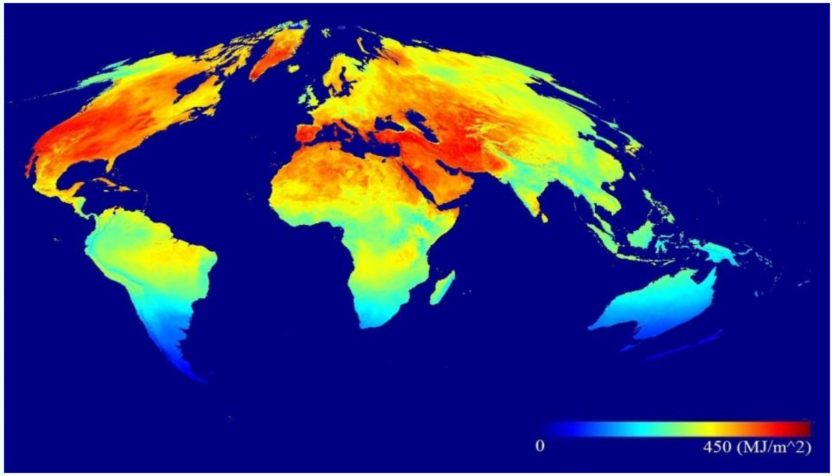

PAR in July 2008

GLASS产品算法

算法技术路线图

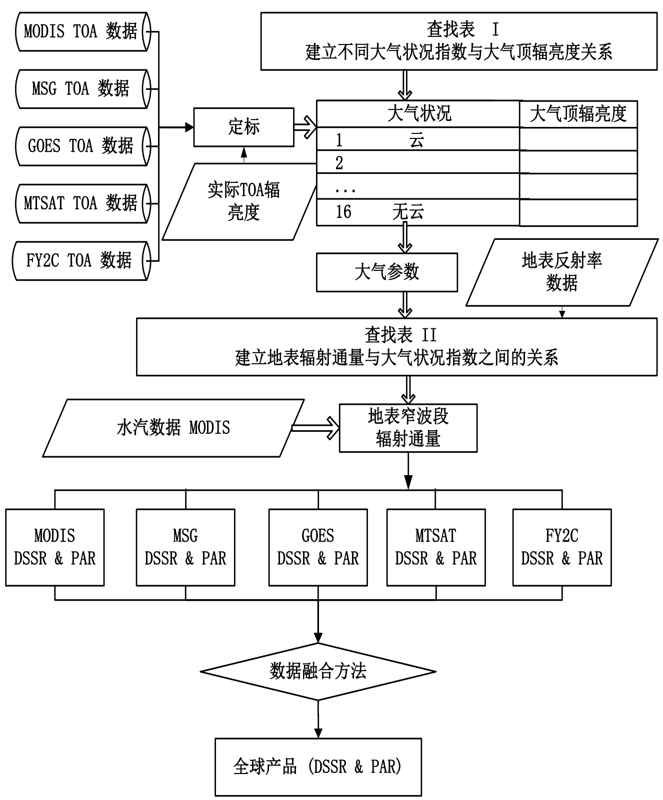

GLASS辐射产品采取算法流程：首先用遥感反演算法处理多源遥感数据得到初级产品，第二步融合多种初级卫星辐射产品得到全球产品。其核心思想是通过MODTRAN4模拟，建立各种大气和观测条件下下行短波辐射和和光合有效辐射与大气顶辐亮度之间关系。

算法特色

- 首次使用多源遥感数据（极轨卫星和静止卫星）反演得到全球陆表短波辐射和光合有效辐射产品，证明了使用多源遥感数据反演全球高级遥感辐射产品的可行性。
- 输入数据简单（无需使用卫星遥感高级产品，避免其它产品误差精度累计）的同时保持了算法反演精度，大幅度提高了现有辐射全球产品的时间和空间分辨率。

Zhang, X., Liang, S., Wu, H., & Zhou, G. (2012). Mapping Global Incident Downward Shortwave Radiation and Photosynthetically Active Radiation Over Land Surfaces Using Multiple Satellite Data. Journal of Geophysical Research, revised

Huang, G., Wang, W., Zhang, X., Liang, S., Liu, S., Zhao, T., Feng, J., & Ma, Z. (2013). Validation of GLASS-DSSR products using surface measurements collected in arid and semi-arid region of China. International Journal of Digital Earth, in revision

Mapping surface radiation-GOES12

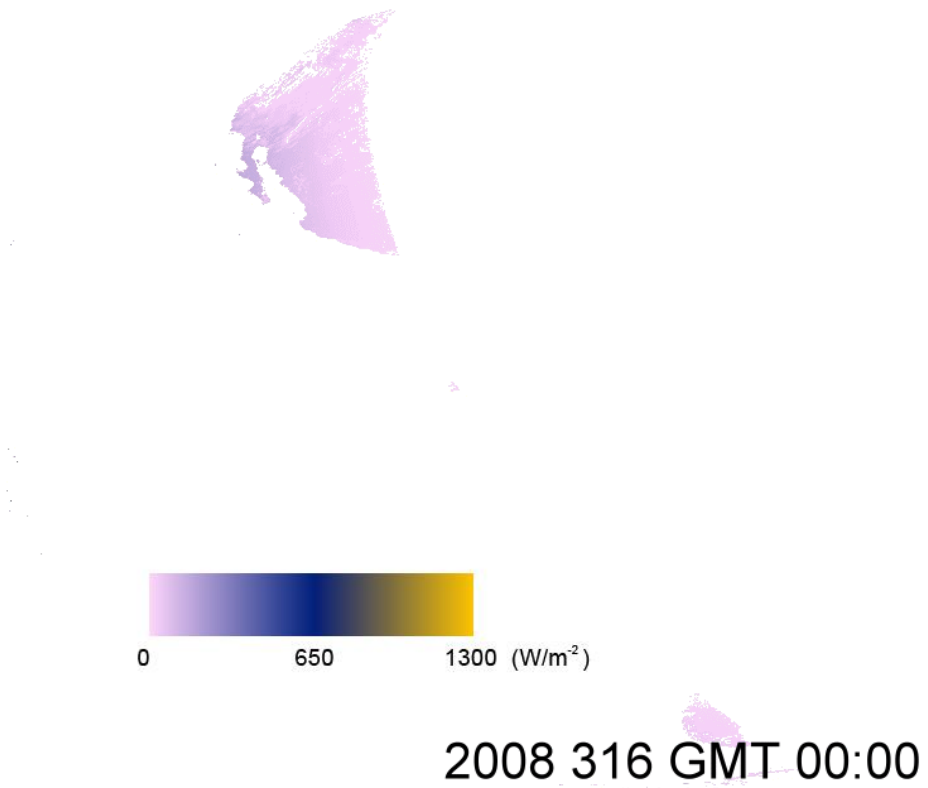

Spatial resolution: 5km
Temporal resolution: 3 hours

Mapping surface radiation-GOES11

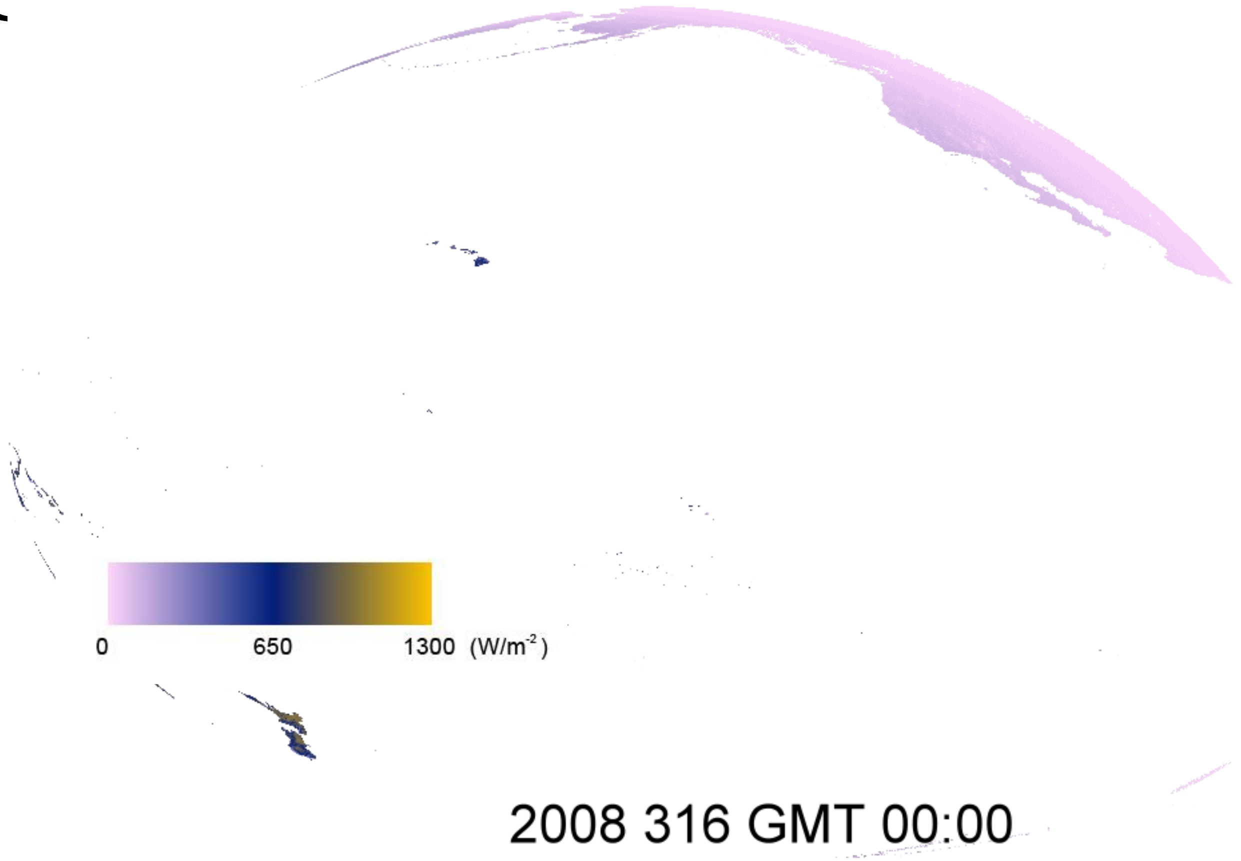

Spatial resolution: 5km
Temporal resolution: 3 hours

Mapping surface radiation-MSG2

Spatial resolution: 5km
Temporal resolution: 15 mins

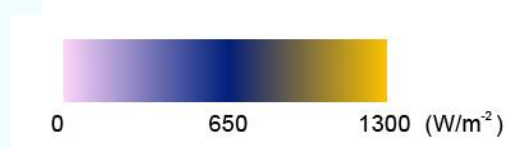

Mapping surface radiation-MTSAT

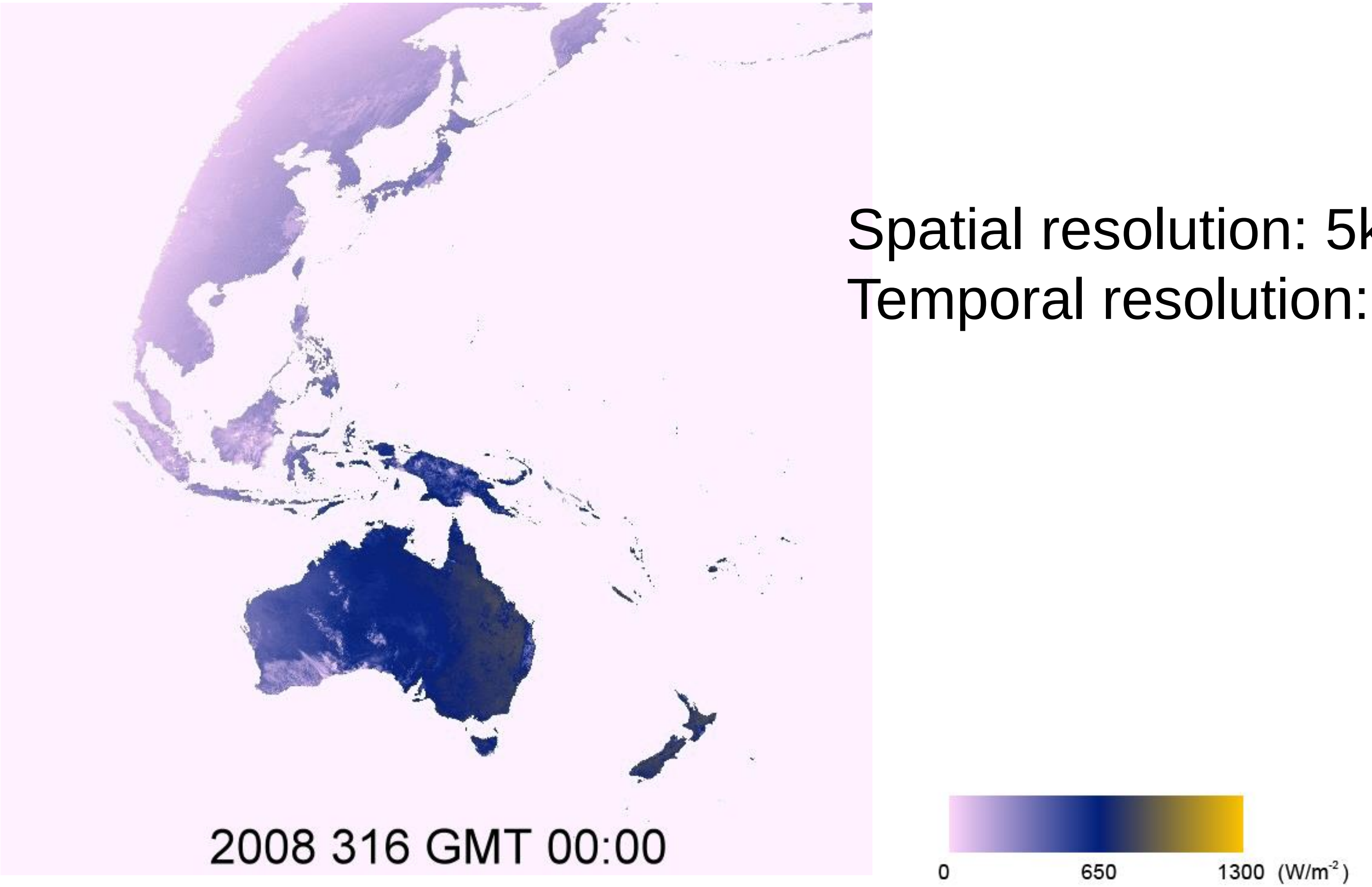

Spatial resolution: 5km
Temporal resolution: 1 hour

Mapping surface radiation-MODIS

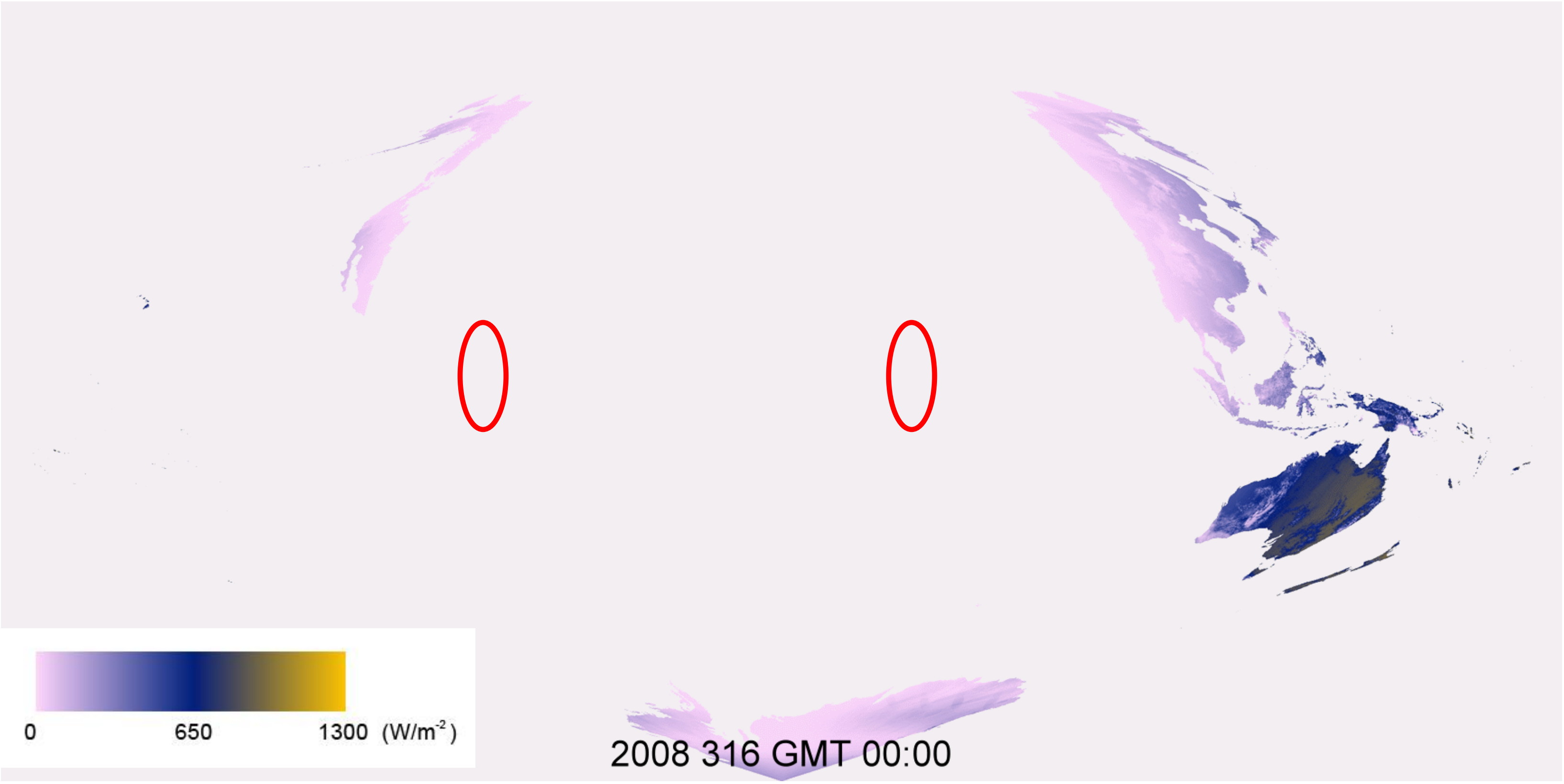

Spatial resolution: 5km
Temporal resolution: 3 hours

Mapping surface radiation-Fusion

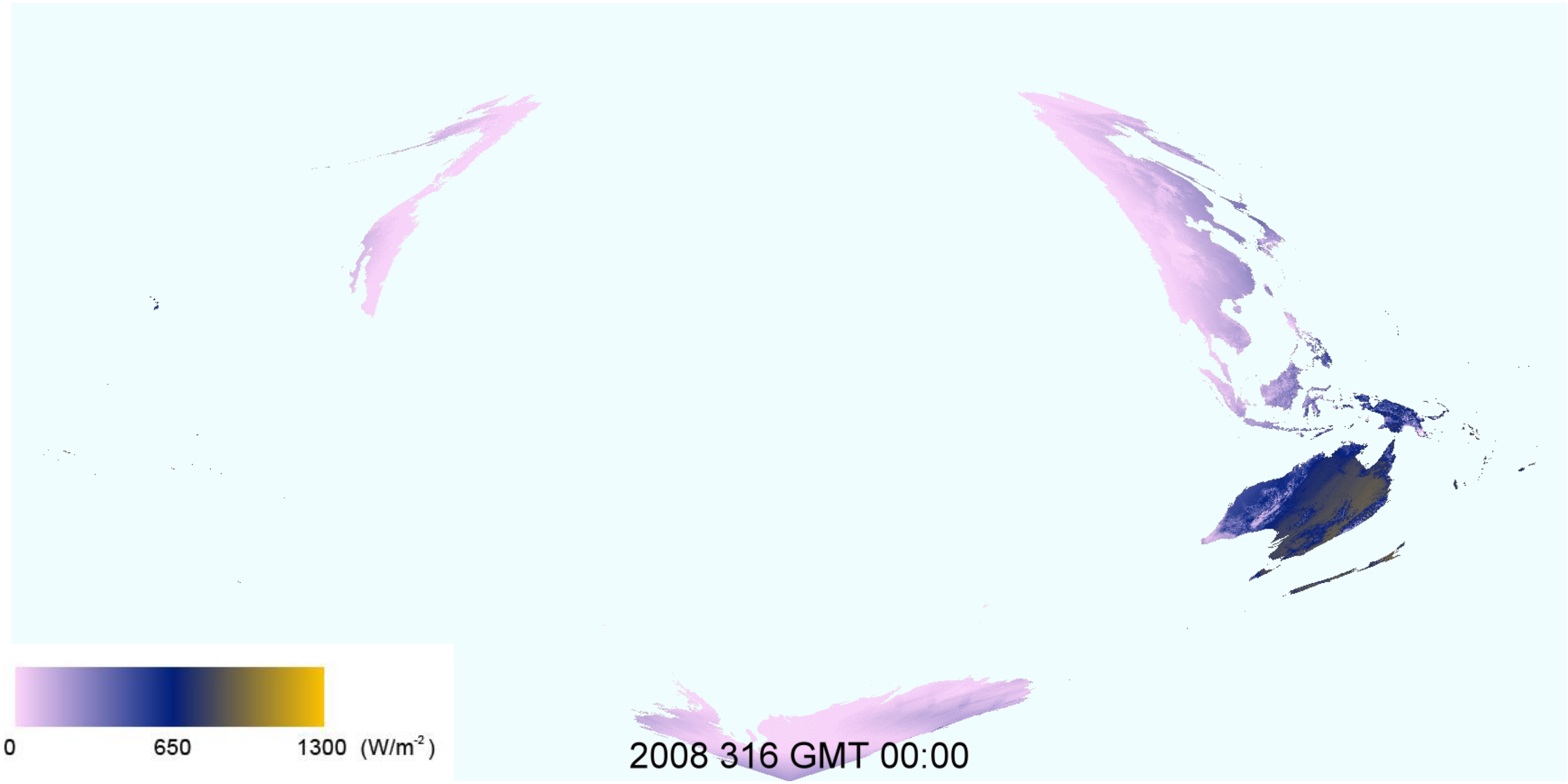

Validation

- SURFRAD – 7 sites

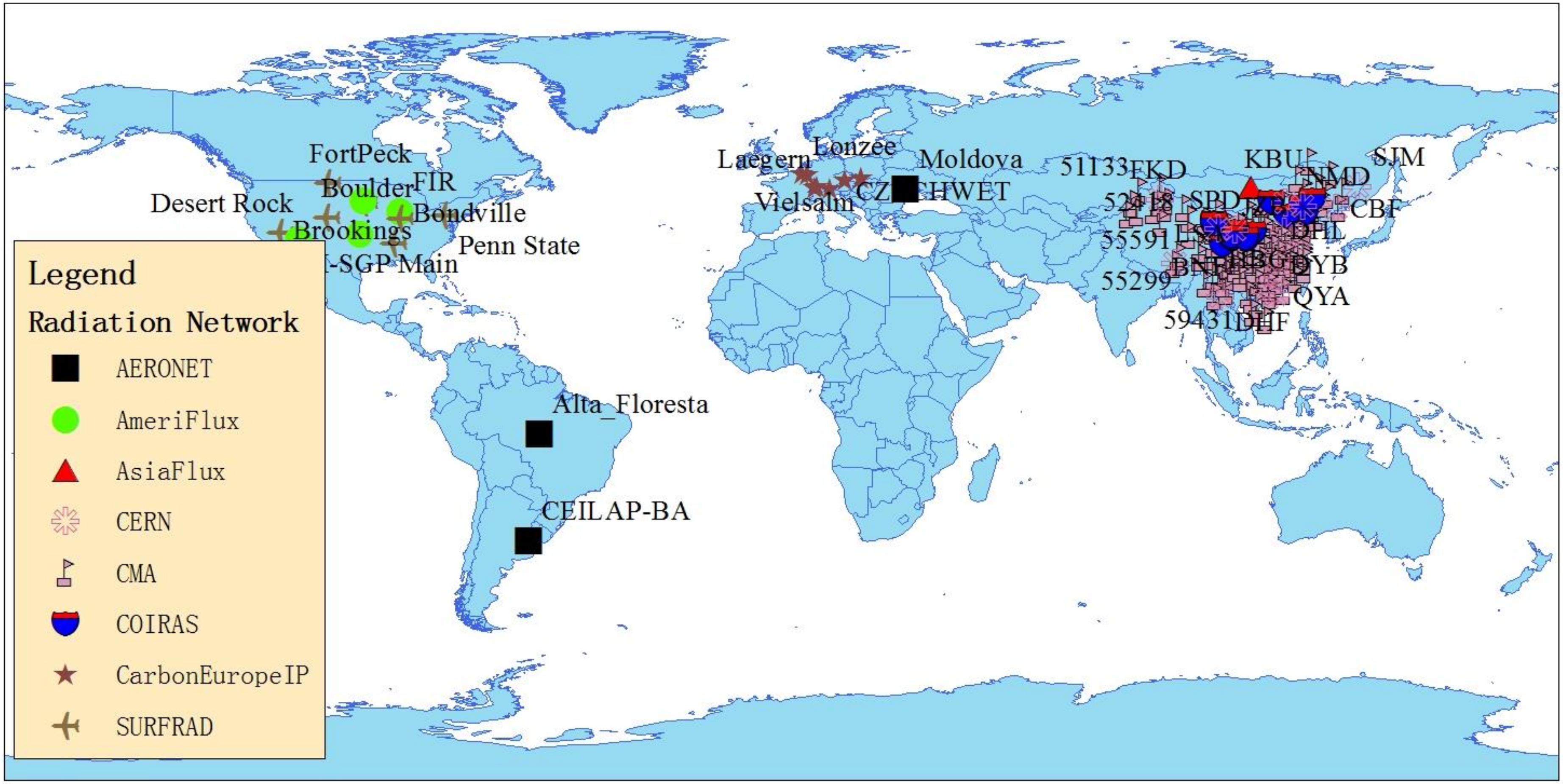

R Square of DSSR validation results at SURFRAD, AERONET, AmeirFlux and CarbonEuropeIP sites

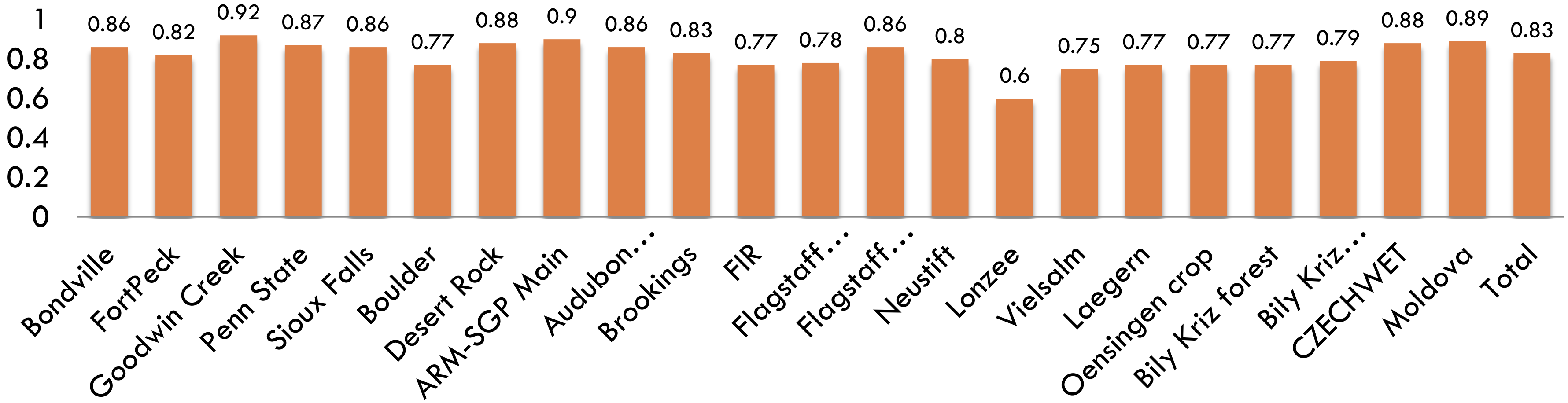

Bias of DSSR validation results at SURFRAD, AERONET, AmeirFlux and CarbonEuropeIP sites

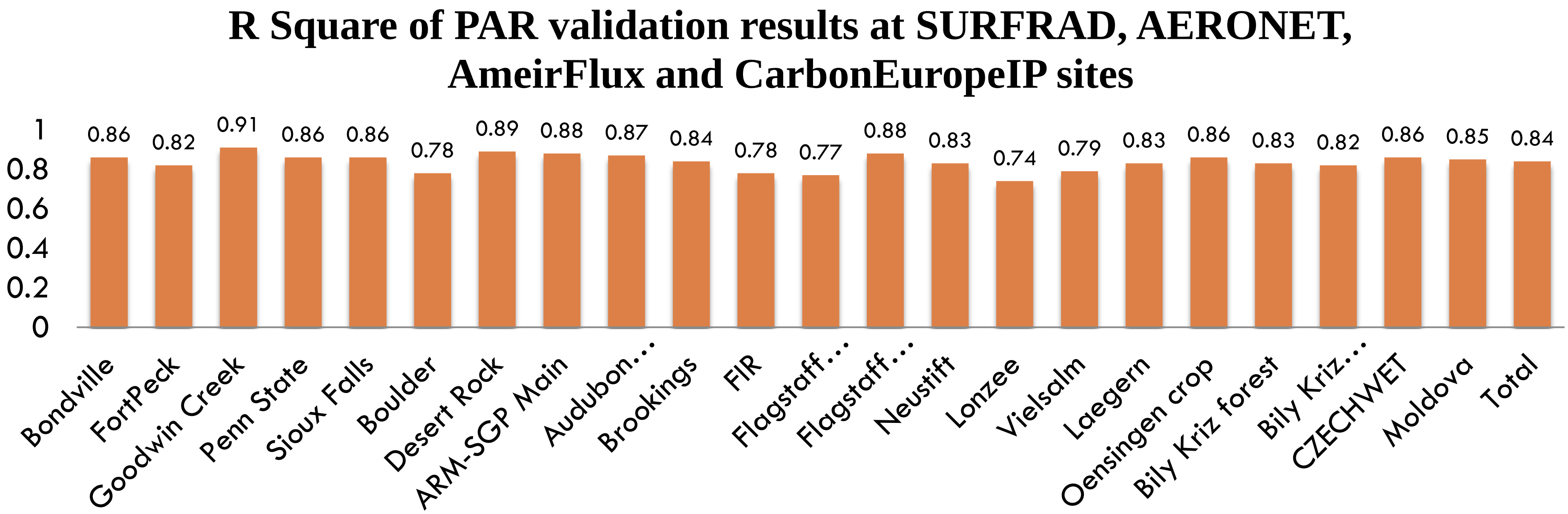
R Square of PAR validation results at SURFRAD, AERONET, AmeirFlux and CarbonEuropeIP sites
1
0.8
0.6
0.4
0.2
0
0.86
0.82
0.91
0.86
0.86
0.78
0.89
0.88
0.87
0.84
0.78
0.77
0.88
0.83
0.74
0.79
0.83
0.86
0.83
0.82
0.86
0.85
0.84
Bondville
FortPeck
Goodwin Creek
Penn State
Sioux Falls
Boulder
Desert Rock
ARM-SGP Main
Audubon…
Brookings
FIR
Flagstaff…
Flagstaff…
Neustift
Lonzee
Vielsalm
Laegern
Oensingen crop
Bily Kriz forest
Bily Kriz…
CZECHWET
Moldova
Total

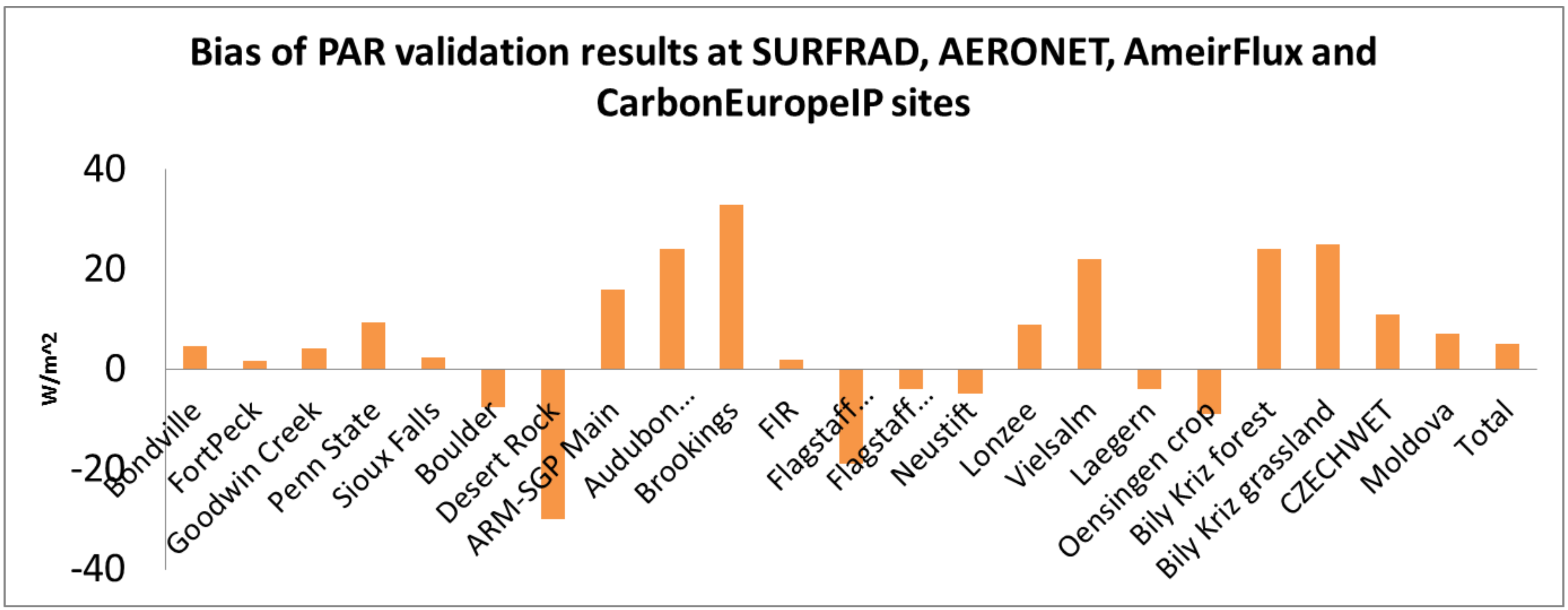
Bias of PAR validation results at SURFRAD, AERONET, AmeirFlux and CarbonEuropeIP sites
W/m^2
40
20
0
-20
-40
Bondville
FortPeck
Goodwin Creek
Penn State
Sioux Falls
Boulder
Desert Rock
ARM-SGP Main
Audubon…
Brookings
FIR
Flagstaff…
Flagstaff…
Neustift
Lonzee
Vielsalm
Laegern
Oensingen crop
Bily Kriz forest
Bily Kriz grassland
CZECHWET
Moldova
Total

Comparison with other products

Site	Retrieved DSSR			ISCCP-FD			CERES-MODIS-CALIPSO (CCCM)			
							Model B			E
	R2	Bias	RMSE	R2	Bias	RMSE	R2	Bias	RMSE	R2
Bondville	0.87	14.68	104.97	0.71	-7.06	149.88	0.84	12.9	119.5	0.82
FortPeck	0.84	10.51	102.75	0.69	9.61	150.37	0.81	5.3	112.40	0.80
Goodwin Creek	0.91	-6.29	99.54	0.64	12.61	184.11	0.69	14.3	172.0	0.66
Penn State	0.85	18.17	109.3	0.7	5.92	152.88	0.87	6.9	107.0	0.86
Sioux Falls	0.81	11.52	114.41	0.65	37.83	168.85	0.62	-11.4	167.4	0.58
Boulder	0.81	-12.8	126.38	0.72	6.49	154.96	0.34	-12.0	249.3	0.47
DesertRock	0.93	-53.4	113.94	0.87	-43.4	135.37	0.53	-34.3	198.0	0.49

提纲

- 背景
- 下行太阳辐射/天空”变亮”与”变暗”
- 地面反照率
- 下行长波辐射
- 地面温度，发射率和上行长波辐射
- ET

森林砍伐后的反照率效应

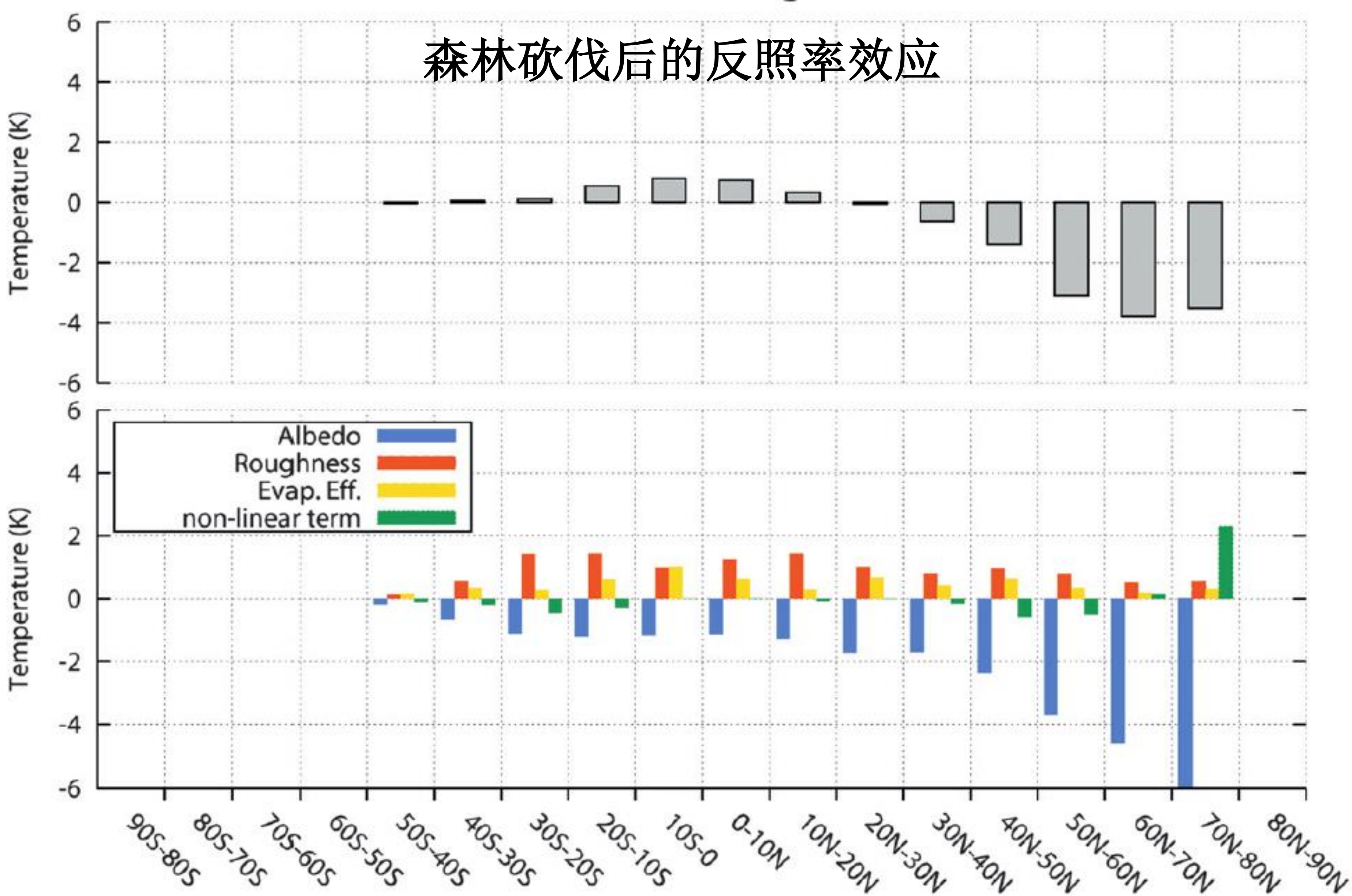

Annual mean change in surface temperature zonally averaged over deforested areas only. The bottom panel of each figure indicates the relative contribution of change in surface albedo, change in evapotranspiration efficiency, change in surface roughness, and nonlinear effects.

Albedo-based geoengineering solutions to offset CO2

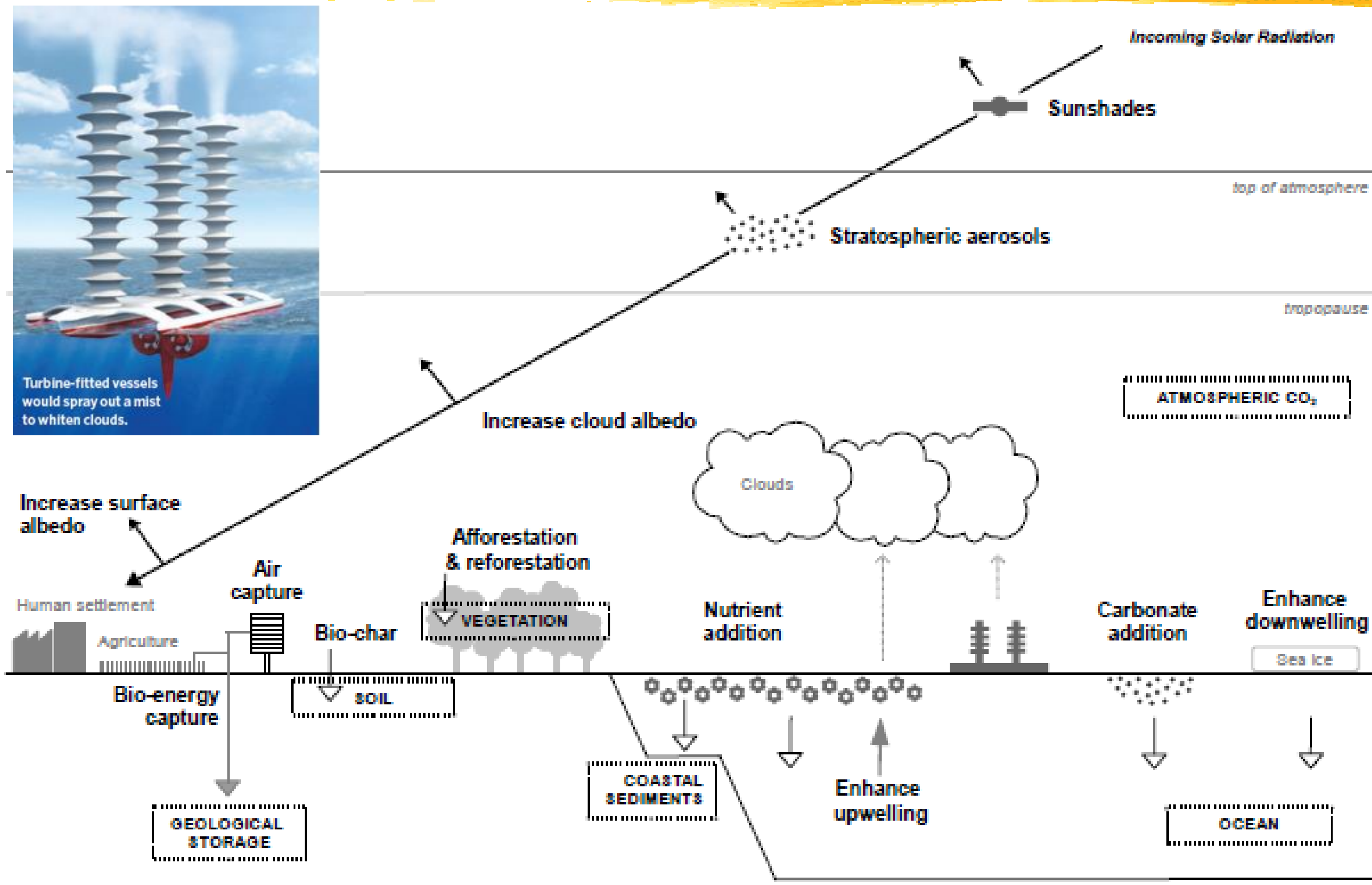

Fig. 1. Schematic overview of the climate geoengineering proposals considered. Black arrowheads indicate shortwave radiation, white arrowheads indicate enhancement of natural flows of carbon, grey downward arrow indicates engineered flow of carbon, grey upward arrow indicates engineered flow of water, dotted vertical arrows illustrate sources of cloud condensation nuclei, and dashed boxes indicate carbon stores. From Vaughan and Lenton (2009), not to scale.

Part of MODIS algorithm for global production

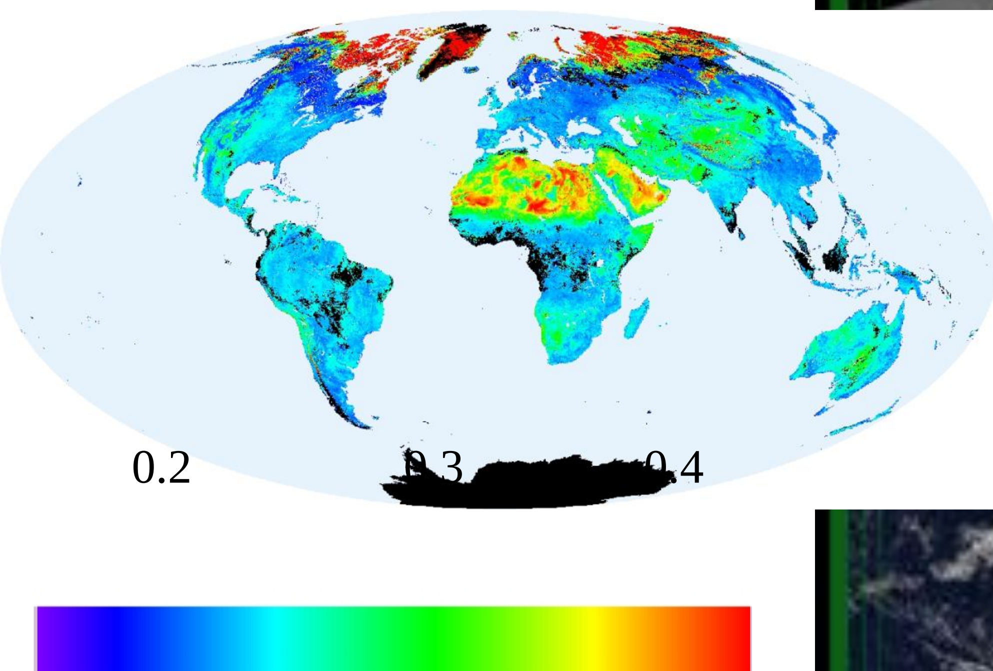

Global White-sky (bihemispherical) Albedo for the period 30 Sep - 13 Oct, 2002

Broadband albedo estimation

Liang

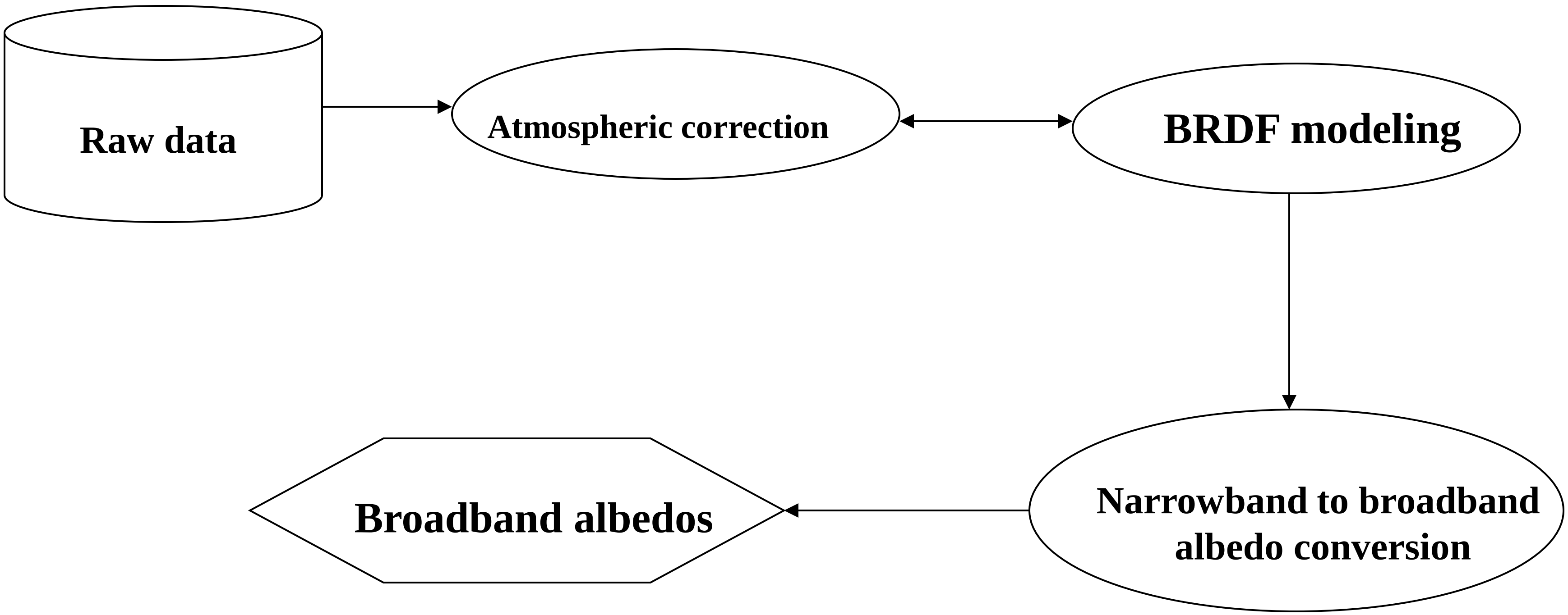

Flowchart of MODIS albedo algorithm

Issues of MODIS albedo algorithm

Liang

- Atmospheric correction: based on the "dark-object" method, requiring dense green vegetation canopies;
- Angular modeling: accumulates observations from multiple (16) days but surface conditions may change;
- Narrowband-broadband conversion: based on empirical statistical analysis for average atmospheric conditions with considerable uncertainty;
- Atmospheric correction requires BRDF information & angular modeling requires atmospherically corrected surface reflectance;
- Errors associated with each procedure may cancel or reinforce each other.

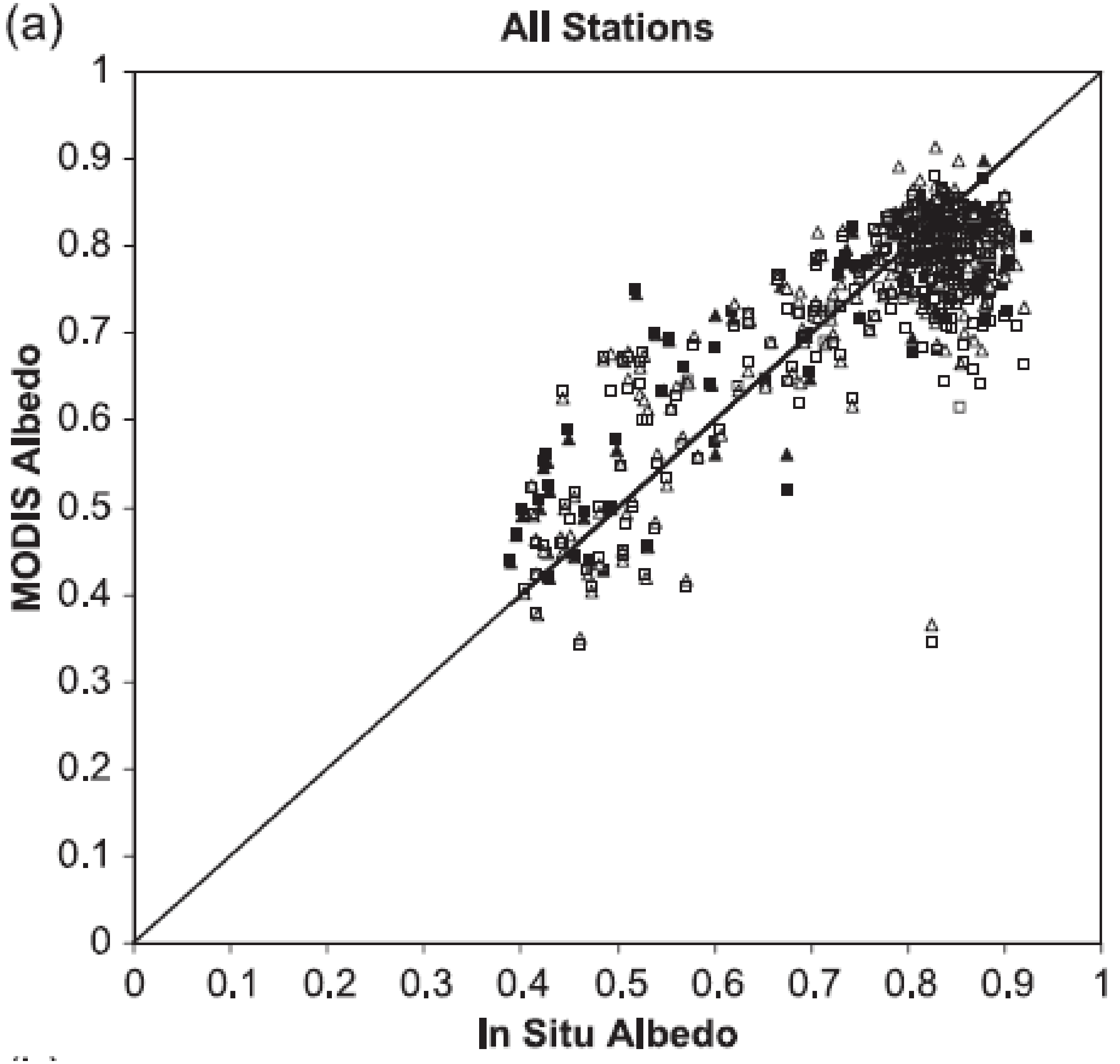

Validation of MODIS shortwave albedo product over Greenland

Stroeve, J., J. Box, F. Gao, **S., Liang**, A., Nolin, and C. Schaaf, (2005), *Accuracy assessment of the MODIS 16-day snow albedo product: Comparisons with Greenland in situ measurements, Remote Sensing of Environment, 94(1):46-60.*

Spatial/temporal filtering

Liang

The NASA albedo product has "gaps" due to instrument malfunction, data missing, and poor retrieval. A gap filling is needed.

Fang, H., S. Liang, H. Kim, J. Townshend, C. Schaaf , A. Stralher, R. Dickinson, (2007), **Developing spatially continuous 1km surface albedo dataset over North America from Terra MODIS products,** *Journal of Geophysical Research*, 112, doi:10.1029/2006JD008377

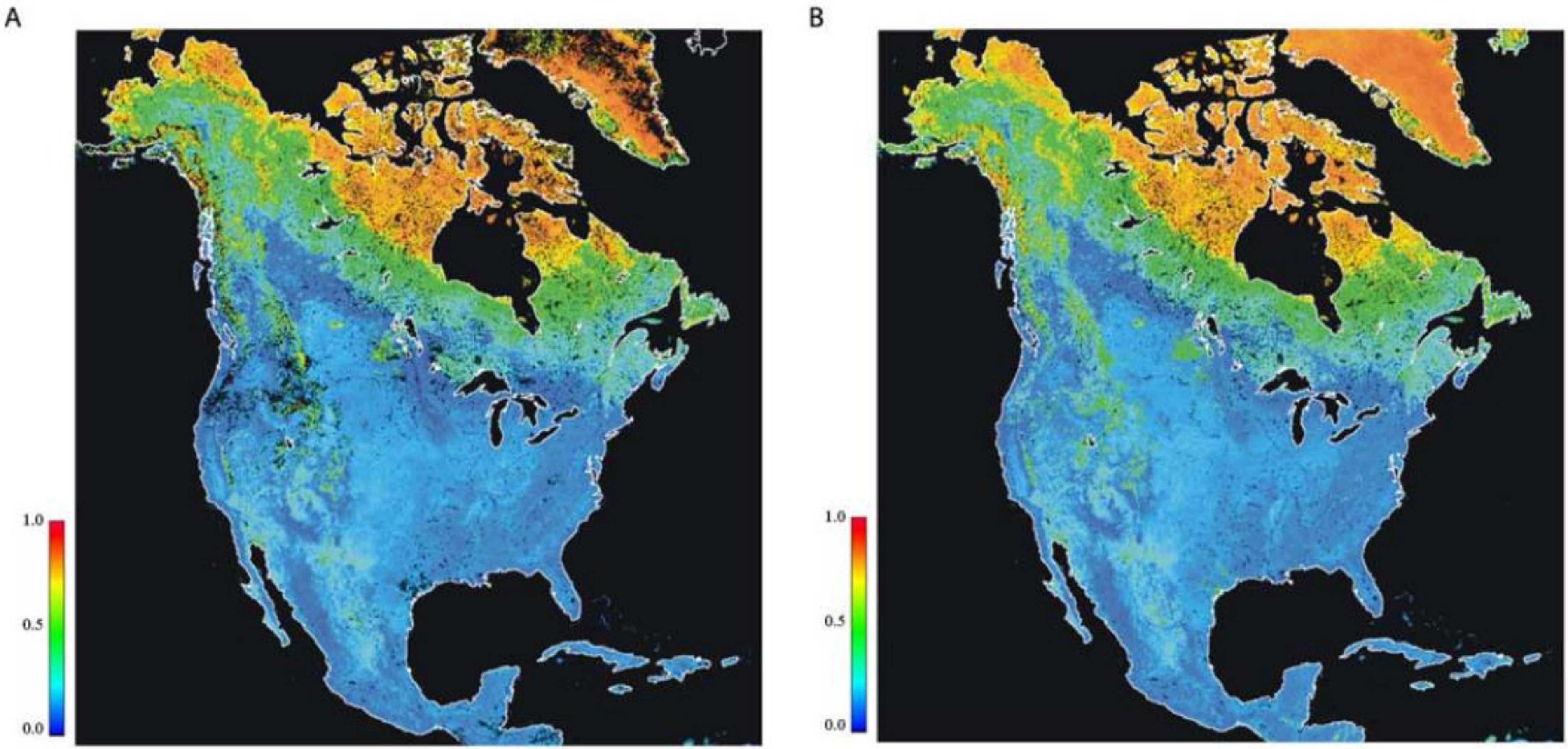

North America total shortwave black-sky albedo (DOY 97–112, 2001). (a) The original MODIS albedo; (b) Derived with the new filter

Fang, H., S. Liang, H.-Y. Kim, J. R. Townshend, C. L. Schaaf, A. H. Strahler, and R. E. Dickinson (2007), Developing a spatially continuous 1 km surface albedo data set over North America from Terra MODIS products, J. Geophys. Res., 112, doi:10.1029/2006JD008377.

Broadband albedo estimation
Joint Polar Satellite System (JPSS)

Liang

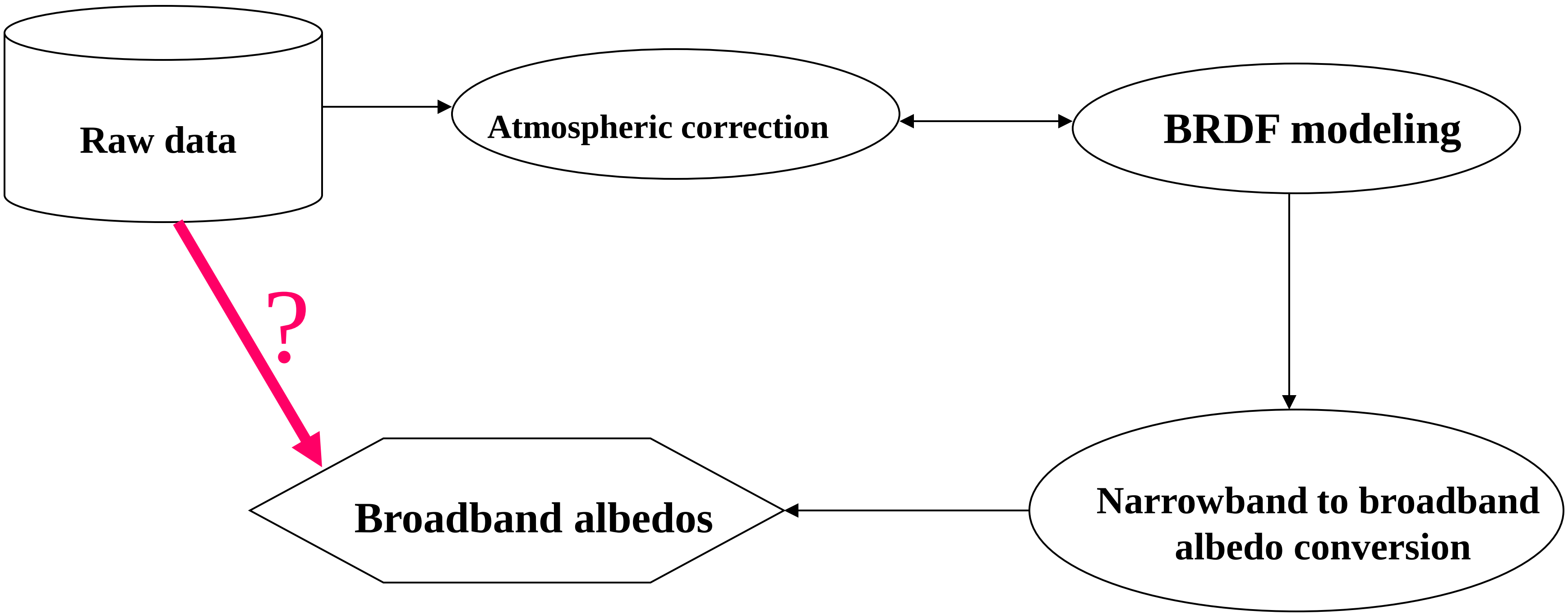

Liang, S., (2003), A direct algorithm for estimating land surface broadband albedos from MODIS imagery, *IEEE Trans. Geosci. Remote Sen.*, 41(1):136-145*;*

Liang, S., J. Stroeve and J. Box, (2005), Mapping daily snow shortwave broadband albedo from MODIS: The improved direct estimation algorithm and validation, *Journal of Geophysical Research.* 110 (D10): Art. No. D10109.

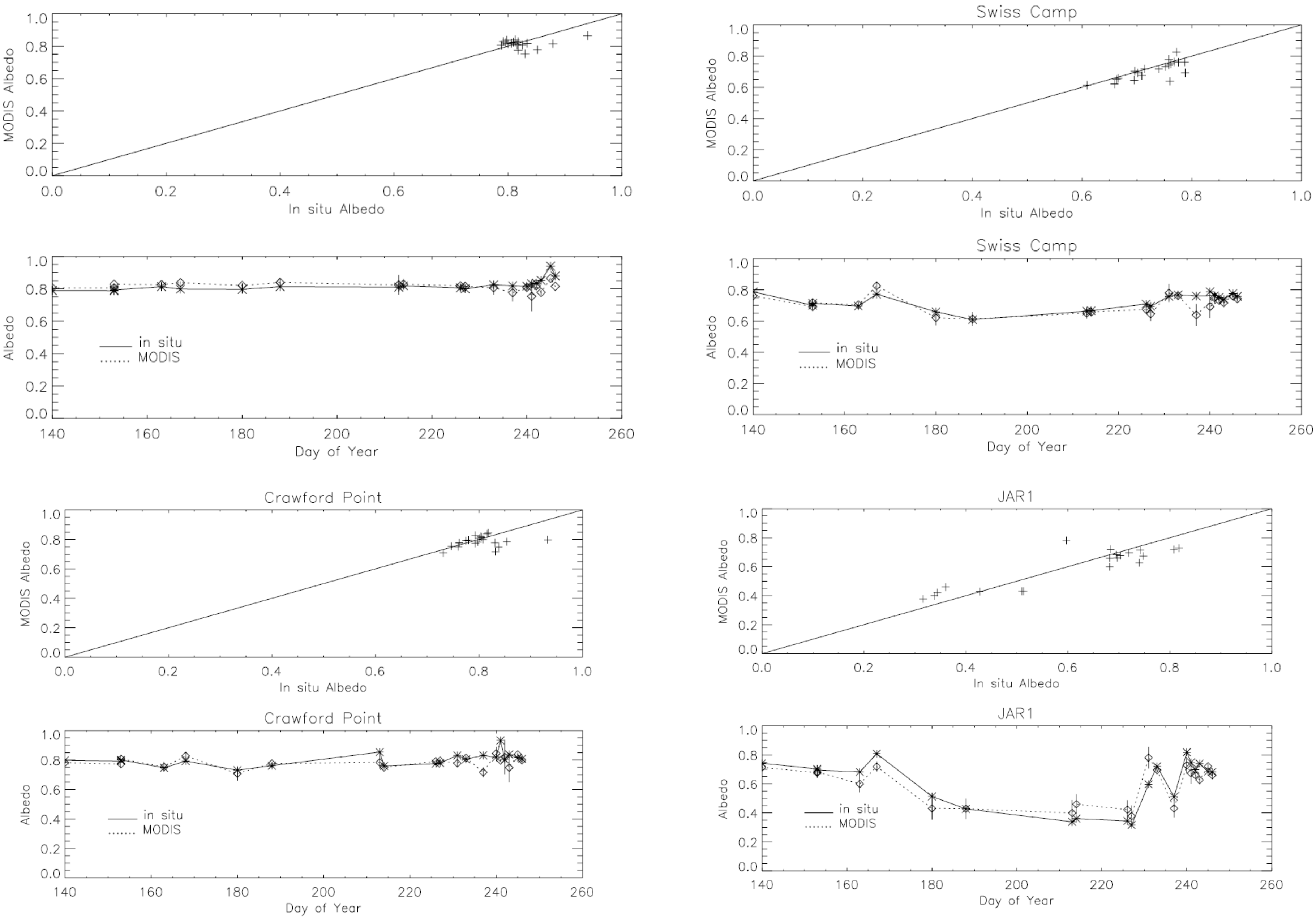

Liang, S., J. Stroeve and J. Box, (2005), *Mapping daily snow shortwave broadband albedo from MODIS: The improved direct estimation algorithm and validation, Journal of Geophysical Research. 110 (D10): Art. No. D10109.*

- This algorithm has been used as the default algorithm for the VIIRS (Visible/Infrared Imager/Radiometer Suite) in the JPSS program

Developing GOSE-R algorithm as a NOAA GOES-R Land Science Team member

Illustration of the proposed GOES-R ABI albedo algorithms

Liang

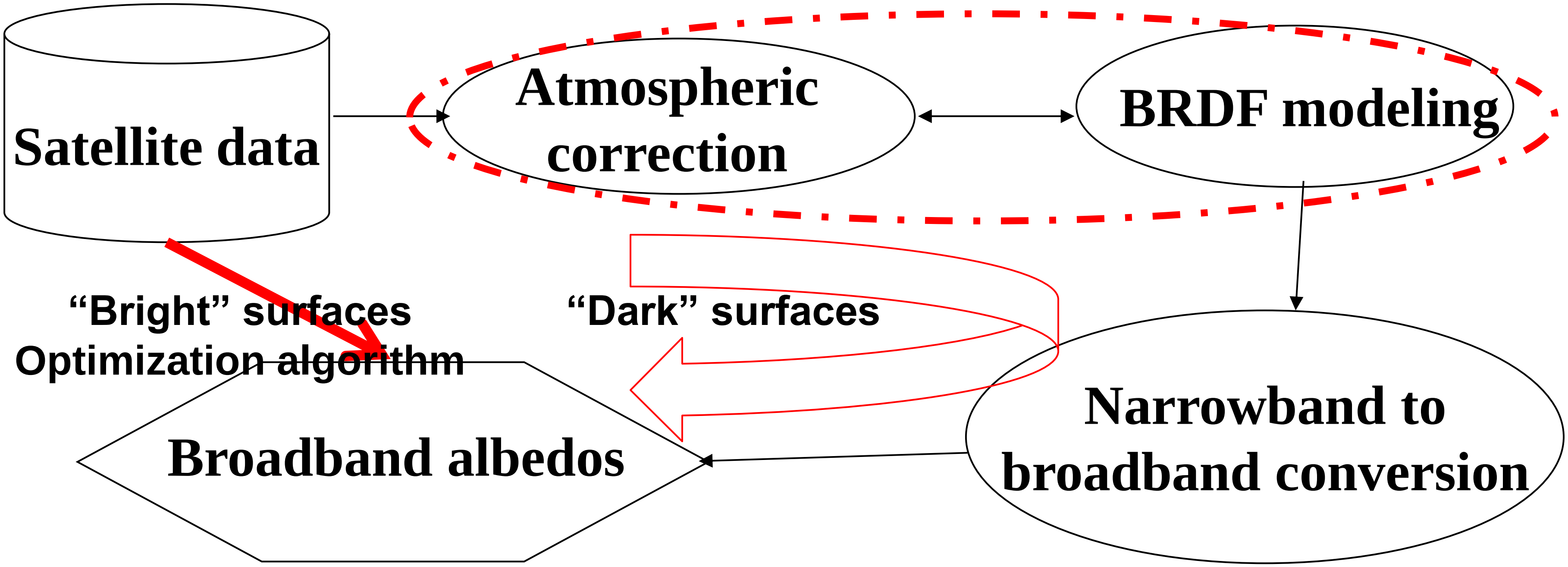

59

地表-大气参数联合优化算法

算法原理

Liang

- 通常来说，地表反照率研究需要大气校正的遥感数据；而大气参数提取及大气校正过程中又需要地表波谱和BRDF的信息，地气相互作用是耦合的。

- 地表-大气联合优化反演的方法针对MSG/SEVIRI静止卫星数据提出，同时求解最优的大气气溶胶参数以及地表二向反射分布函数，该方法主要目的是提取气溶胶信息，同时也求解了地表反照率

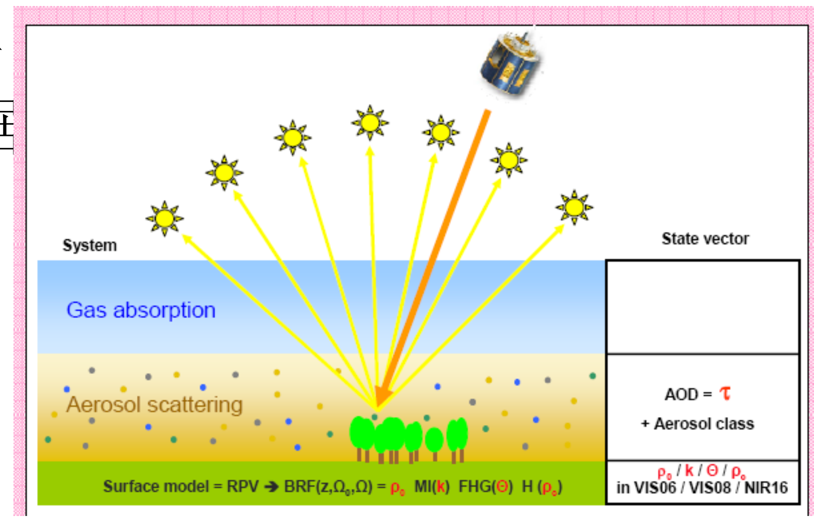

Tao, H., **S. Liang**, D. Wang, H. Wu, Y. Yu, J. Wang, (2012), Estimation of Surface Albedo and Directional Reflectance from Moderate Resolution Imaging Spectroradiometer (MODIS) Observations, *Remote Sensing of Environment*, 119:286-300

GLASS 短波段反照率

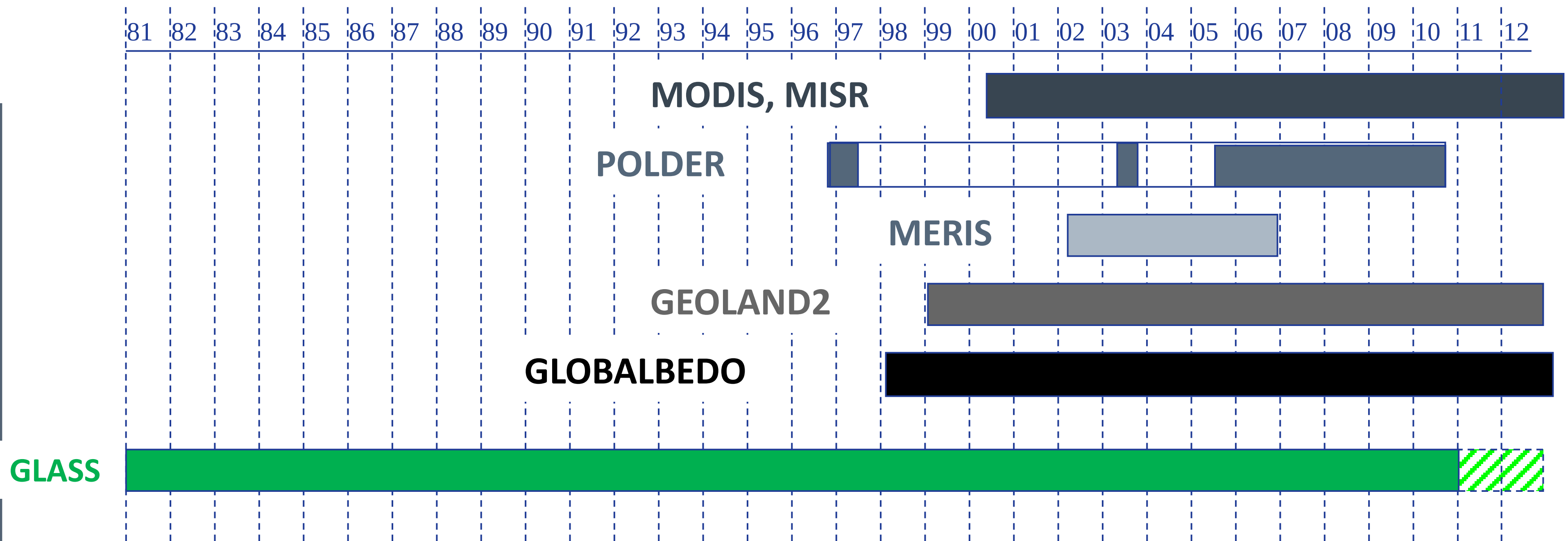

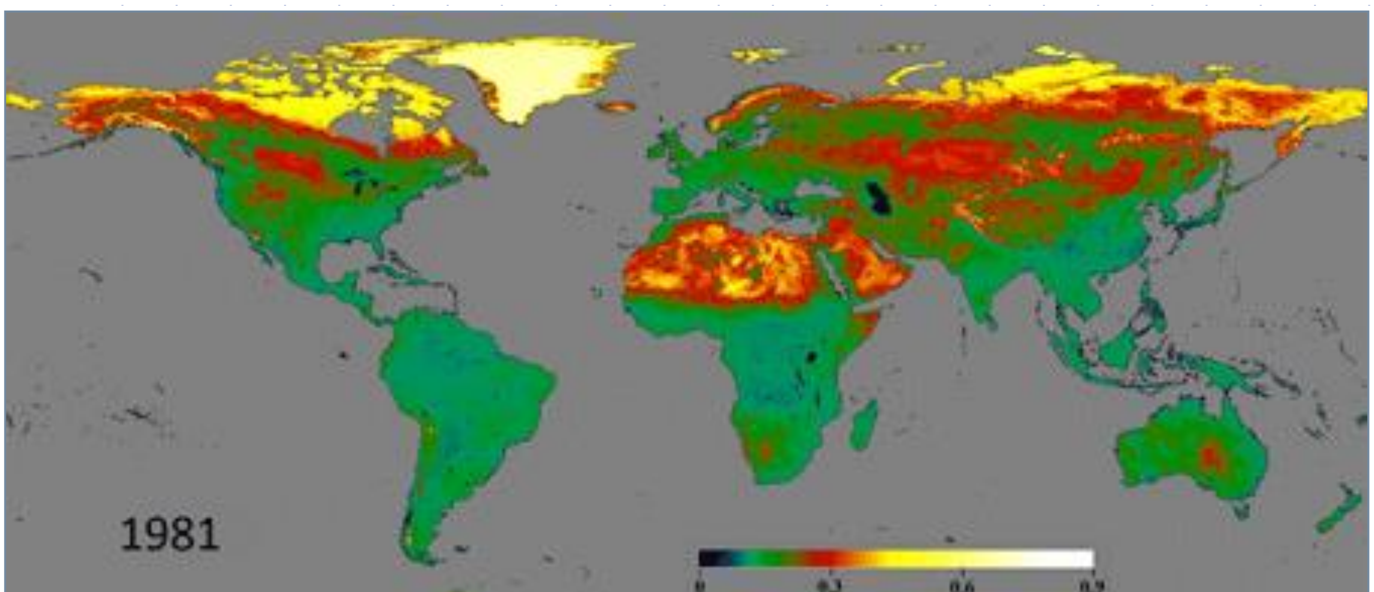

Qu, Y., Liu, Q., Liang, S., Wang, L., Liu, N., & Liu, S. (2013). Improved direct-estimation algorithm for mapping daily land-surface broadband albedo from MODIS data. *IEEE Transaction on Geoscience and Remote Sensing, doi: 10.1109/TGRS.2013.2245670*

Liu, N., Liu, Q., Wang, L., Liang, S., Wen, J., Qu, Y., & Liu, S. (2013a), Liu, N., Liu, Q., Wang, L., Liang, S., Wen, J., Qu, Y., & Liu, S. (2013). A statistics-based temporal filter algorithm to map spatiotemporally continuous shortwave albedo from MODIS data. Hydrology and Earth System Sciences, doi:10.5194/hess-5117-5191-2013

Liu, Q., Wang, L., Qu, Y., Liu, N., Liu, S., Tang, H., & Liang, S. (2013b). A Preliminary Evaluation of GLASS Albedo Product. *International Journal of Digital Earth*, in press

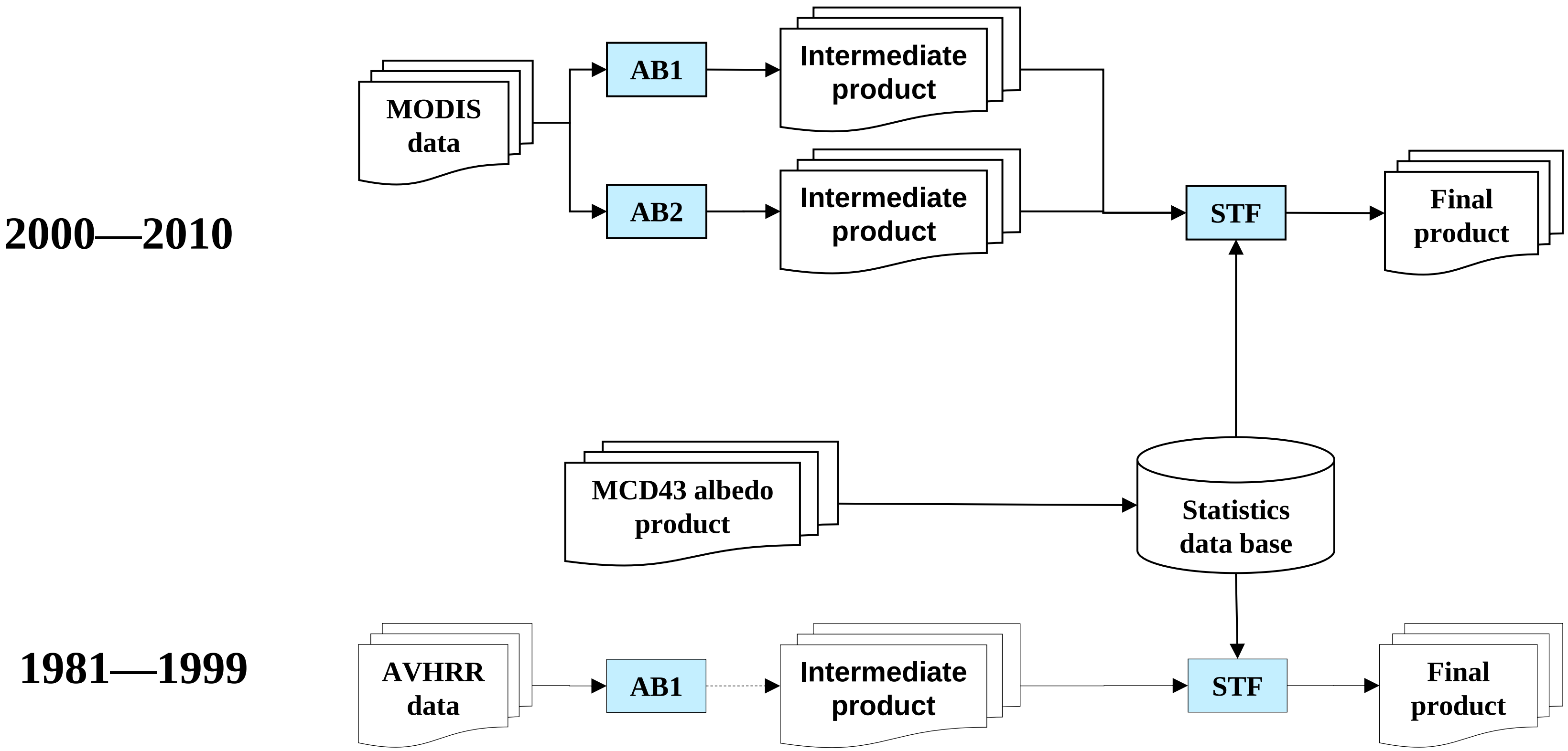

AB1 AB2 ：二套反演算法

STF ：时态滤波算法

这是世界上第一次用多种算法生成全球陆表产品

长期地表反照率变化

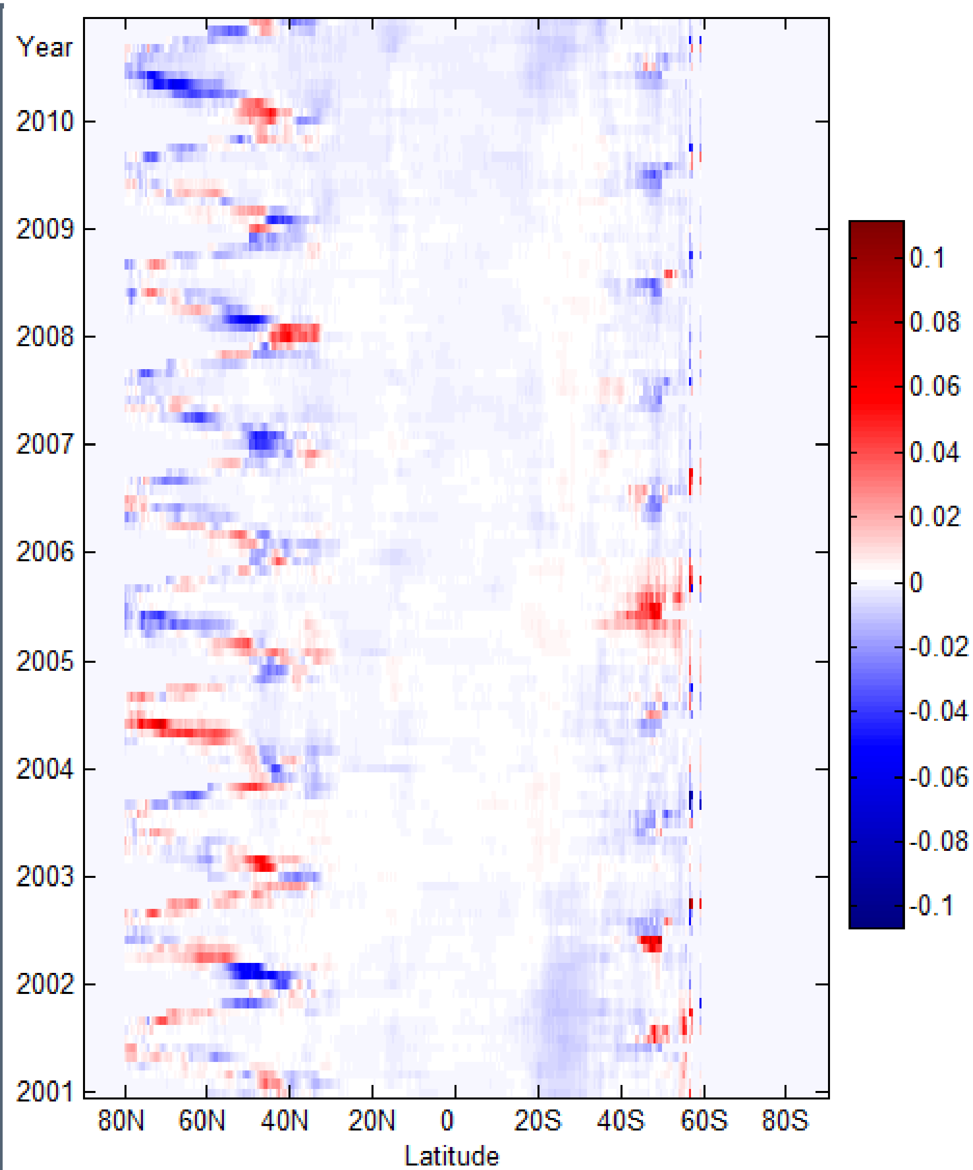
Year
2010
2009
2008
2007
2006
2005
2004
2003
2002
2001
80N 60N 40N 20N 0 20S 40S 60S 80S
Latitude
0.1
0.08
0.06
0.04
0.02
0
-0.02
-0.04
-0.06
-0.08
-0.1

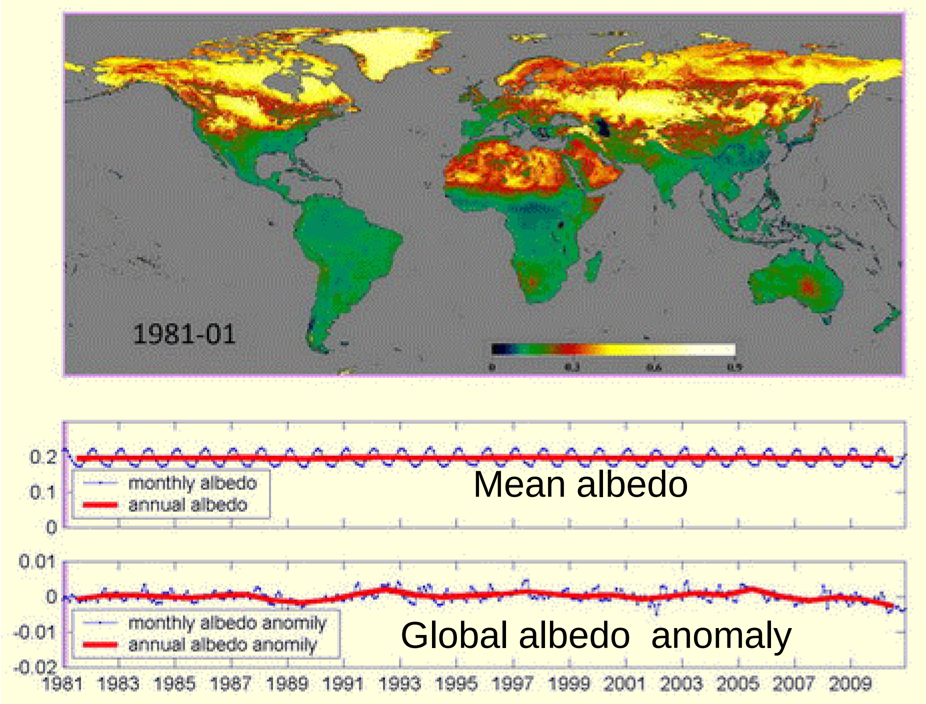
1981-01
0.2
0.1
0
monthly albedo
annual albedo
Mean albedo
0.01
0
-0.01
-0.02
monthly albedo anomily
annual albedo anomily
Global albedo anomaly
1981 1983 1985 1987 1989 1991 1993 1995 1997 1999 2001 2003 2005 2007 2009

全球陆地短波反照率比较

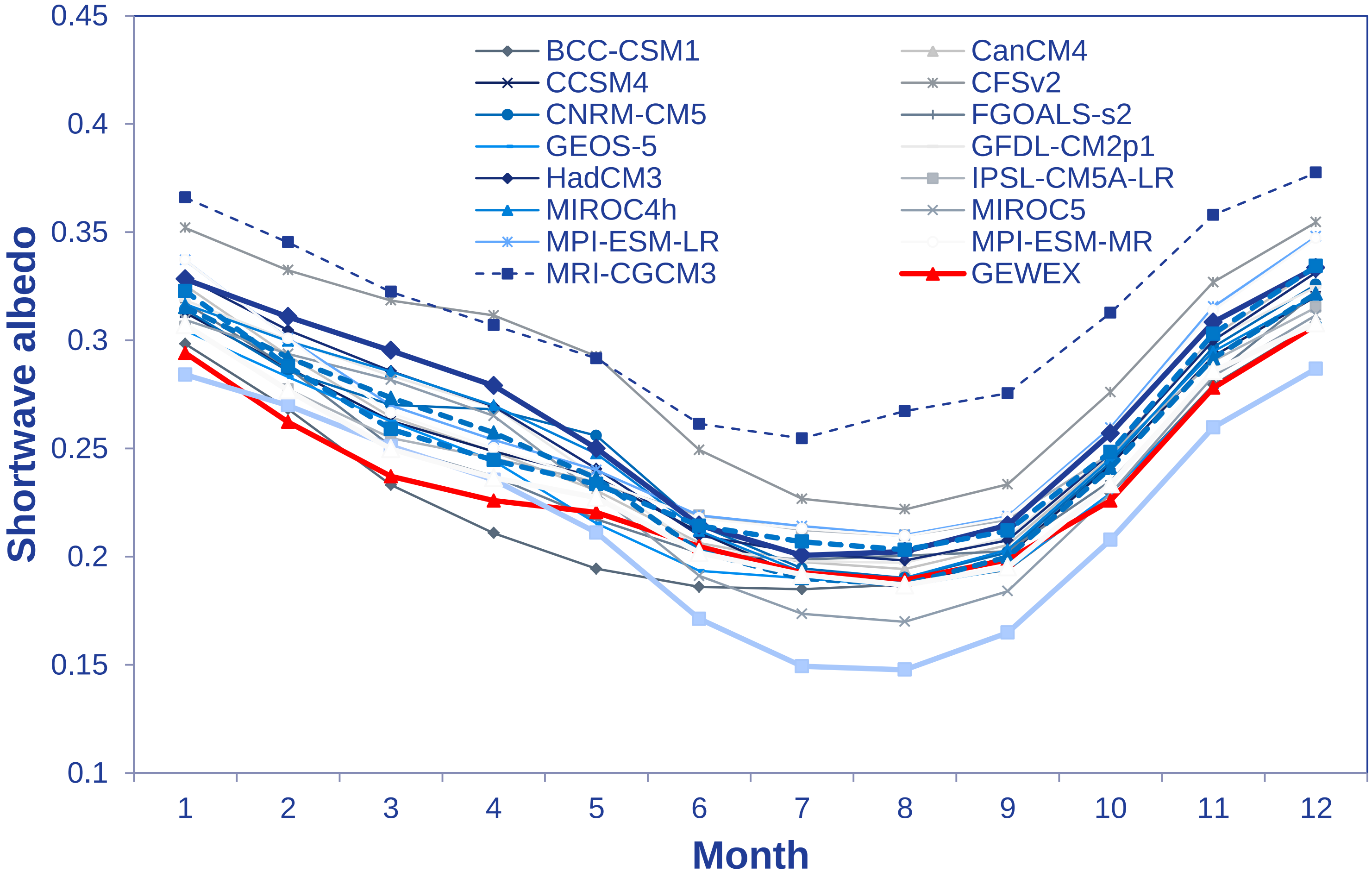

Fig. 1 Inter-comparison of 30-year global albedo climatology derived from satellite products and IPCC AR5 model outputs.

全球及南北半球平均黑空、白空反照率距平与气温、降水、反照率的相关性

（“*”、“**”：分别代表通过了90%、95%的信度检验水平）

	BSA			WSA		
	全球	北半球	南半球	全球	北半球	南半球
LAI	-0.318*	-0.303*	-0.368**	-0.317*	-0.302*	-0.365**
气温	0.324**	0.342**	0.249	0.322**	0.340**	0.248
降水	0.057	0.060	0.047	0.058	0.060	0.048

- 反照率同气温和LAI的相关性良好，全球及南北半球的反照率和LAI均为通过了95%信度检验的负相关；
- 全球和北半球反照率同气温的相关均通过95%信度的检验；
- 反射率同降水的相关普遍不好，均未通过信度检验。

Greenland反照率空间分布与变化

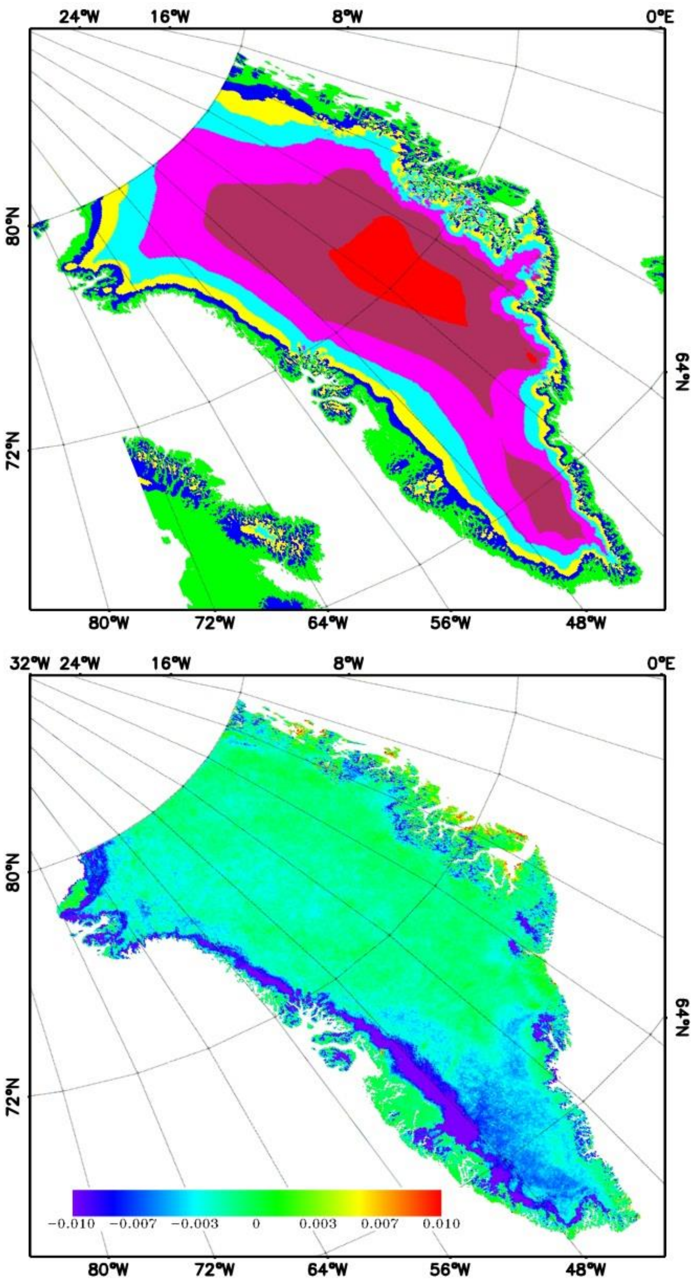

Fig. 5 (a) Digital elevation model of Greenland from USGS GMTED data divided into 8 levels: sea level and below (white), ≤500m (green), 501–1000m (blue), 1001–1500m (yellow), 1501–2000m (cyan), 2001–2500m (magenta), 2501–3000m (maroon), and above 3000m (red); (b) Annual July albedo change rate over Greenland from GLASS products in 2000–2012.

Table 1 Surface albedo changes over different elevations

Elevation (m)	Annual change rate	
	1981–2000	2000–2012
≤500	0.0004	-0.0006
501~1000	0.0001	-0.0035**
1001~1500	-0.0002	-0.0059***
1501~2000	0.0004	-0.0031**
2001~2500	0.0005*	-0.0024**
2501~3000	0.0005**	-0.0015*
>3000	0.0006**	-0.0001

He, et al. 2013b

Greenland 过去32年夏天陆表反照率的变化

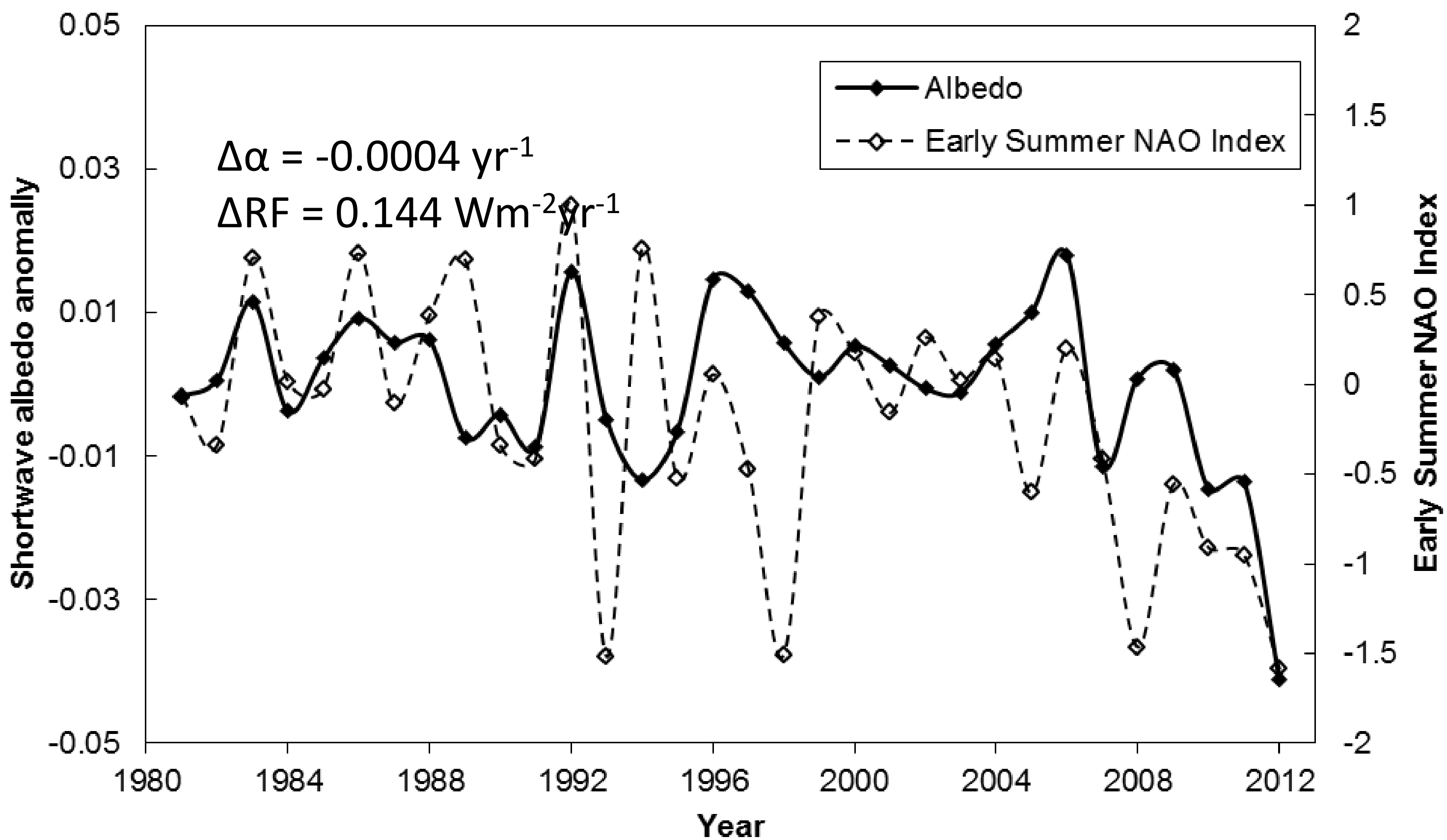

Fig. 6 Surface albedo changes over the entire Greenland from GLASS data and early summer (average of May, June, and July) NAO index (1981–2012).

He, et al. 2013b

青藏高原

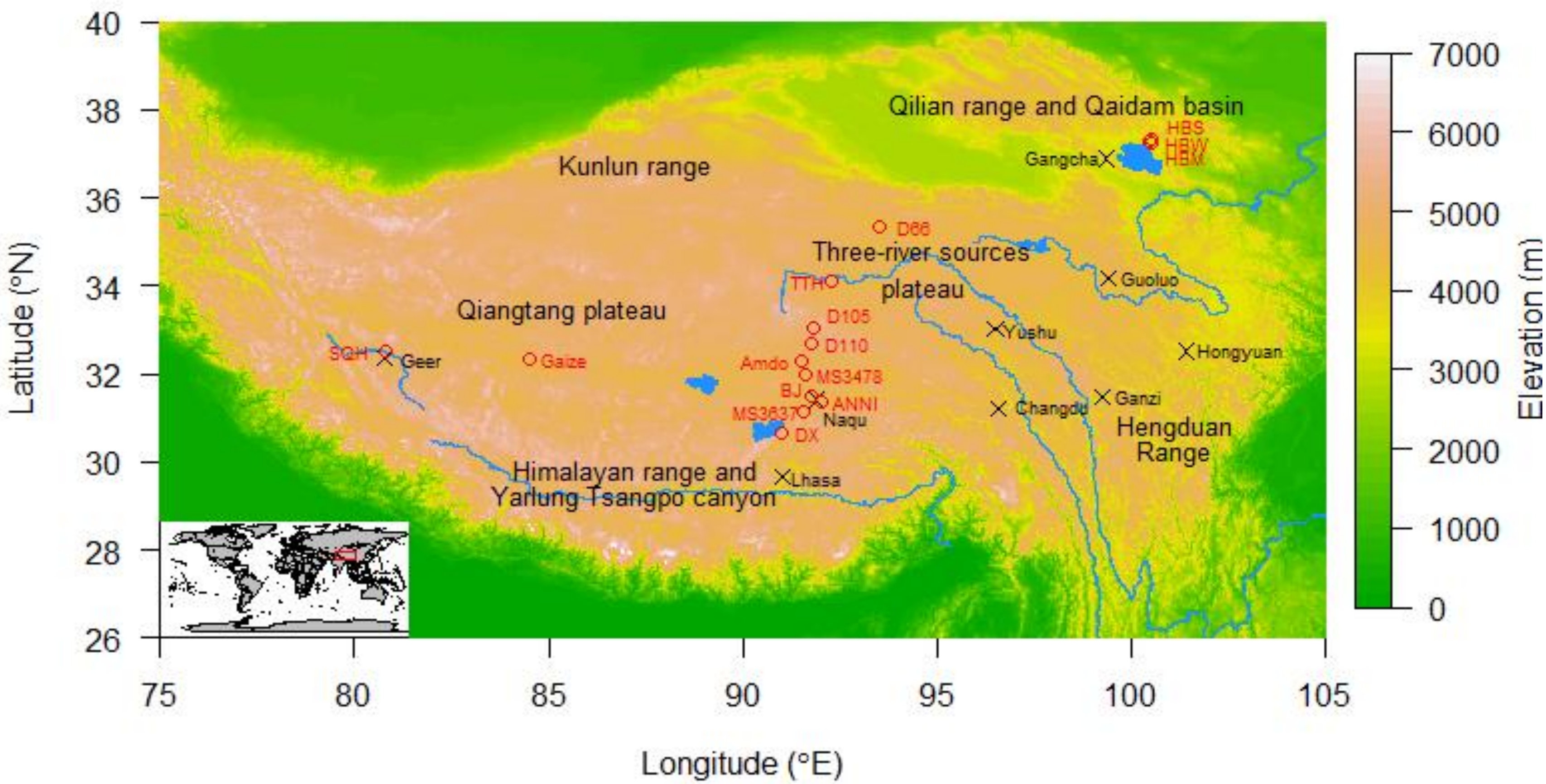

Terrain of the Tibetan Plateau with ground stations, major lakes, rivers, and landforms.

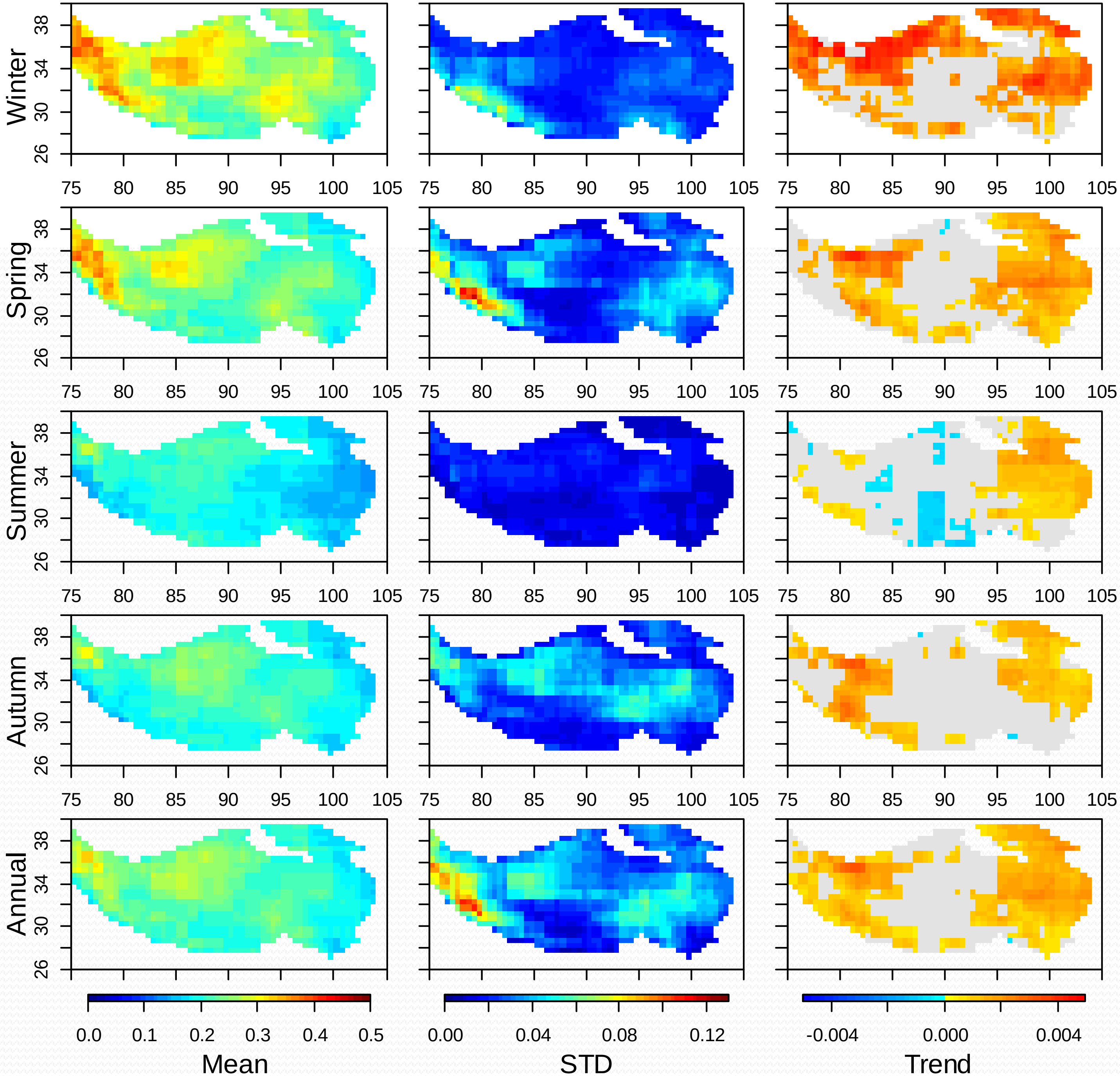

Spatial distribution of mean, STD, and trend of land surface albedo over Tibetan Plateau

反照率和雪覆盖度（SC）（%）

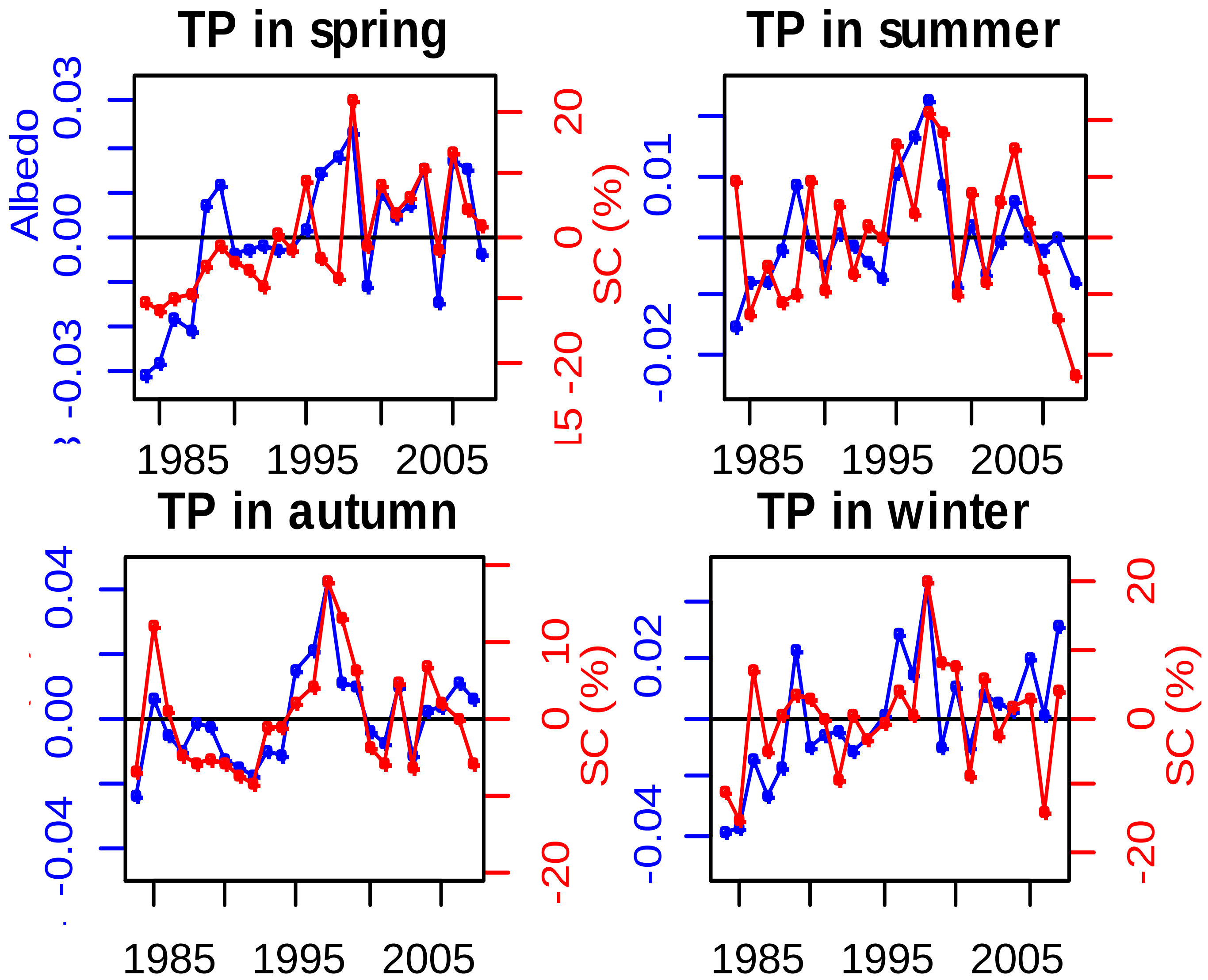
TP in spring
Albedo
SC (%)
1985
1995
2005
TP in summer
TP in autumn
TP in winter

提纲

- 背景
- 下行太阳辐射/天空”变亮”与”变暗”
- 地面反照率
- 下行长波辐射
- 地面温度，发射率和上行长波辐射
- ET

Liang

Fig.1 Monthly averages of longwave downward radiation from two satellite products (ISCCP and GEWEX) and different GCMs in the IPCC AR4.

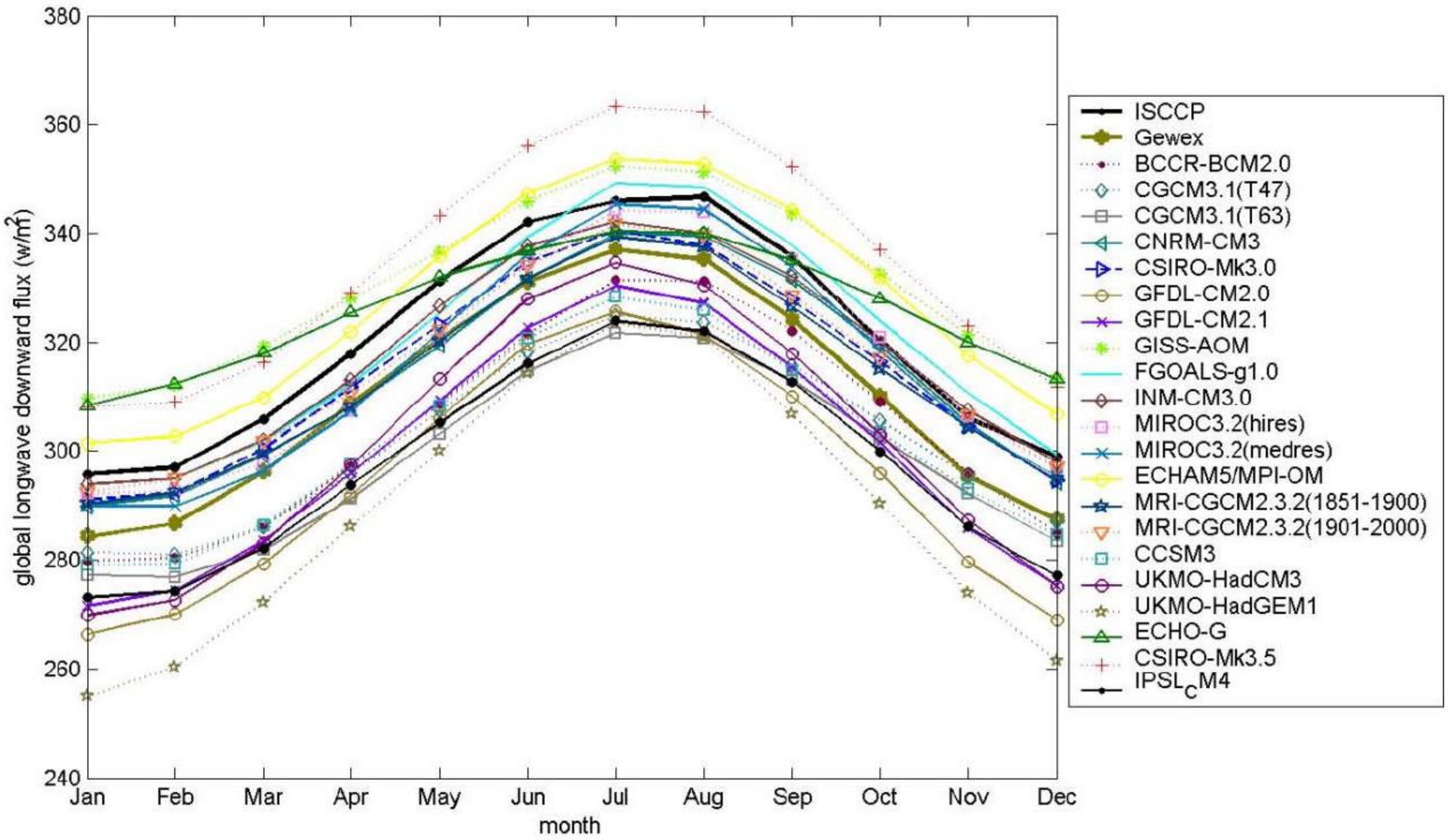

Estimation of downward longwave radiation

Liang

1). Empirical methods
2). Calculating downward flux using atmospheric profiles
3). Calculating downward flux from TOA radiance directly

Wang, K., and **S. Liang**, (2009), Global atmospheric downward longwave radiation under all-sky conditions from 1973 to 2008, *Journal of Geophysical Research*, 114, D19101, doi:19110.11029/12009JD011800

Wang, W. & **S. Liang,** (2009), Estimating High-Spatial Resolution Clear-Sky Land Surface Downwelling and Net Longwave Radiation from MODIS Data, *Remote Sensing of Environment*, 113:745-754

Wang, W., & **S. Liang**, (2010). A Method for Estimating Clear-sky Instantaneous Land Surface Longwave Radiation from GOES Sounder and GOES-R ABI Data. *IEEE Geoscience and Remote Sensing Letters*, 7, 708-712

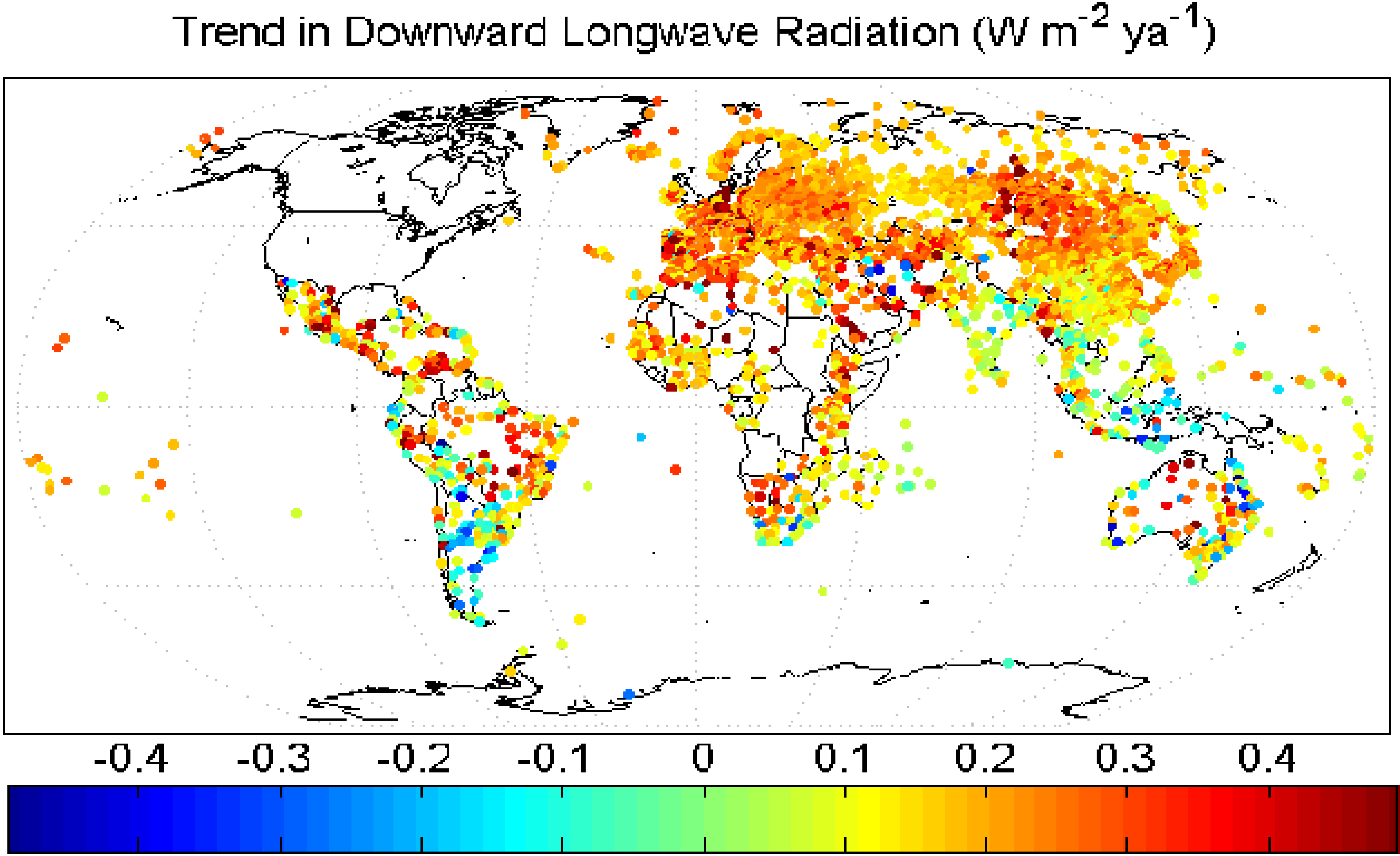

Linear trend of daily (L_d) over 3200 global weather stations where data are available for at least 300 months (35 years) during the period of 1973-2008.

Wang, K., and S. Liang, (2009), Global atmospheric downward longwave radiation under all-sky conditions from 1973 to 2008, *Journal of Geophysical Research*, 114, D19101, doi:10.1029/2009JD011800

Estimating LWDN (MODIS)

Physical Method

- ♣ Using MODIS Profiles & MODTRAN4
- ♣ Problems:
  - ✈ LWDN dominated by near surface temp. & moisture
  - ✈ MODIS profiles are coarse (20 levels)
    - 1000, 950, 920, 850, 800, 700, 620, 500, 400, 300, 250, 200, 150, 100, 70, 50, 30, 20, 10, 5 hPa
  - ✈ Large errors, especially over high elevation sites

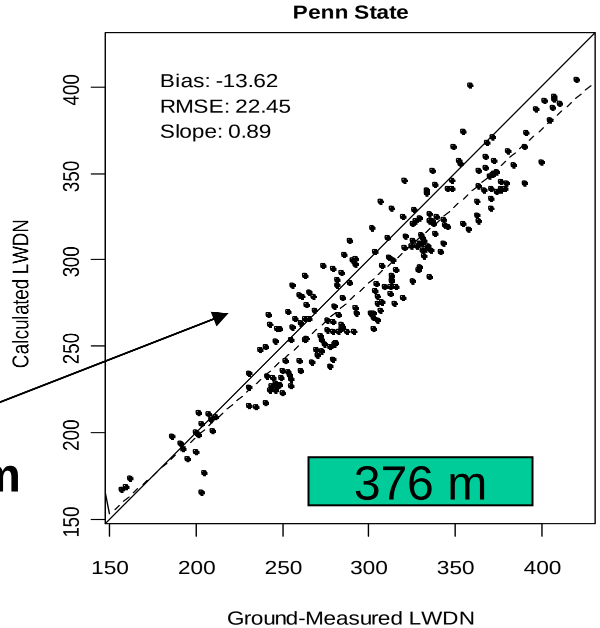

~4 layers below 500 m

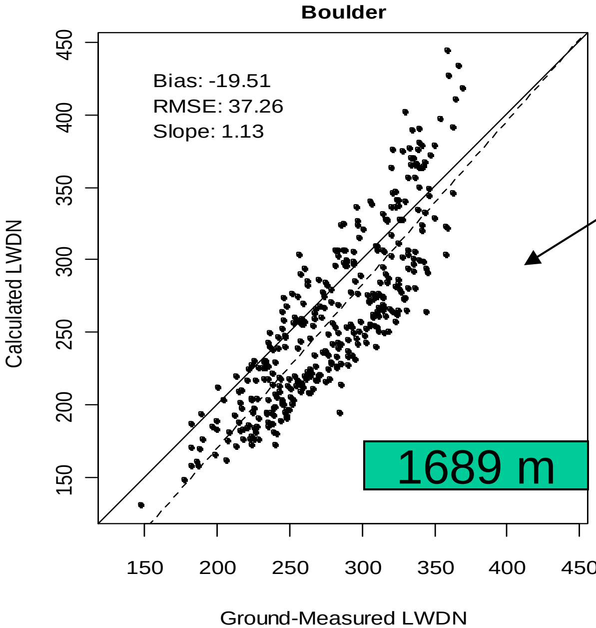

~3 layers below 500 m

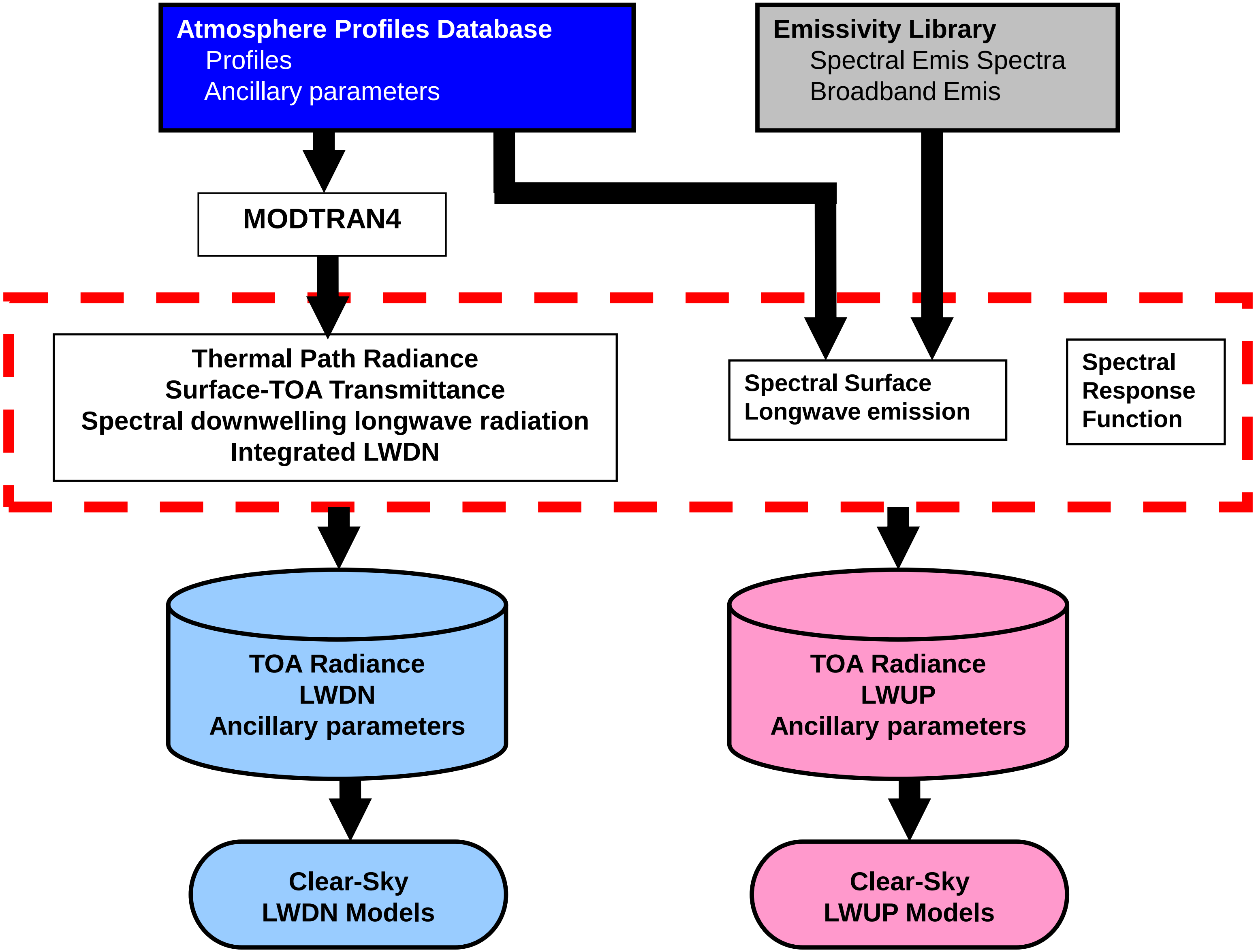

Framework of Hybrid Methods

Estimating LWDN: Validation (Aqua)

Liang

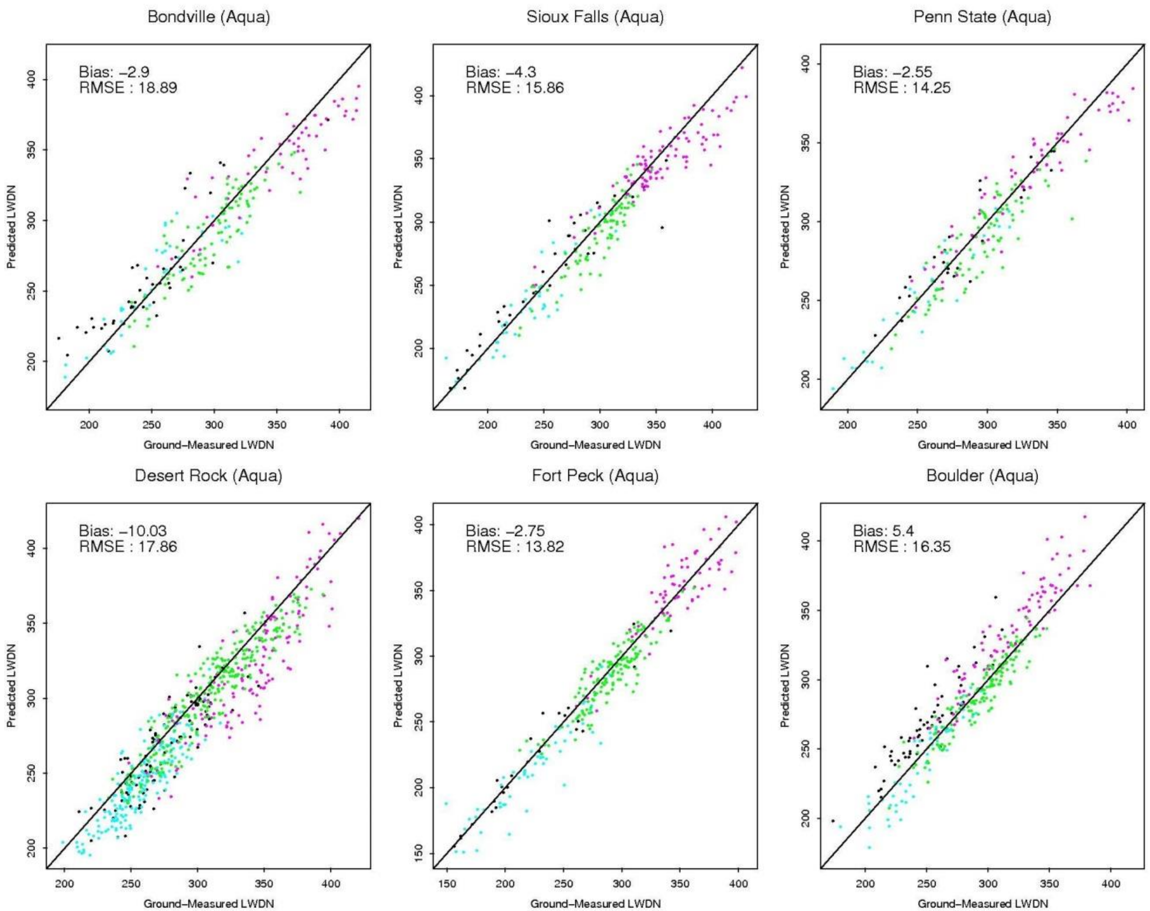

Nonlinear Models

- ♣ Results similar to Terra
- ♣ Smaller RMSEs in Aqua-derived LWDN
  - ✈ Smaller systematic errors in Aqua *(Liu et. Al, 2006)*
  - ✈ *Diff. overpass times → diff. atmospheric conditions*

Avg. RMSE: 17.60 W/m2
Avg. Bias: -0.40 W/m2

day/fallwinter
night/fallwinter
day/springsummer
night/springsumme

Table 5. R^2, Bias, Relative Bias of Satellite Products, STD, and Relative STD of the Differences Between Observed and Satellite-Estimated Clear-Sky LWDN at All Sites for 2003 (Wm^{-2})

	GEWEX-SRB			ISCCP-FD			CERES-FSW			MODIS		
Sites	R^2	Bias(%)	STD(%)	R^2	Bias(%)	STD(%)	R^2	Bias(%)	STD(%)	R^2	Bias(%)	STD(%)
North America												
BON	0.86	−17.7(−5.6)	21.6(6.8)	0.62	−5.2(−1.6)	32.1(10.0)	0.95	3.2(1.1)	15.0(5.0)	0.88	−5.4(−1.8)	22.3(7.4)
TBL	0.79	−23.6(−8.1)	18.4(6.3)	0.58	18.8(6.4)	32.0(10.8)	0.86	−6.4(−2.2)	18.5(6.5)	0.87	1.3(0.5)	18.6(6.5)
DRA	0.94	−29.9(−9.9)	11.4(3.7)	0.76	26.5(8.6)	22.8(7.4)	0.95	−17.7(−5.8)	11.7(3.8)	0.84	−18.2(−5.9)	20.2(6.5)
FPK	0.85	−16.5(−5.7)	20.3(7.0)	0.78	5.6(1.9)	28.2(9.8)	0.92	−3.6(−1.3)	17.9(6.3)	0.93	−4.7(−1.7)	15.7(5.6)
GWN	0.86	−19.9(−5.9)	19.7(5.9)	0.54	−13.0(−3.9)	32.6(9.8)	0.94	−6.3(−2.0)	15.2(4.7)	0.81	−8.2(−2.6)	27.4(8.5)
PSU	0.85	−21.7(−7.1)	21.3(7.0)	0.64	7.2(2.4)	31.7(10.4)	0.92	1.2(0.4)	16.4(5.4)	0.86	−7.3(−2.4)	19.5(6.5)
Mean	0.86	−21.55(−7.1)	18.8(6.1)	0.65	6.7(2.3)	29.9(9.7)	0.92	−4.9(−1.6)	15.8(5.3)	0.87	−7.1(−2.3)	20.6(6.8)
Qinghai-Tibetan Plateau												
Amdo	0.72	−8.8(−5.2)	18.3(10.9)	0.39	34.4(21.9)	24.6(15.6)	0.63	−1.0(−0.6)	21.2(12.3)	0.49	16.0(9.4)	36.2(21.2)
BJ	0.85	−22.6(−10.9)	18.2(8.8)	0.58	39.6(21.5)	25.7(13.9)	0.83	−7.3(−3.7)	18.0(9.1)	0.60	26.3(13.3)	36.4(18.5)
D105	0.72	−7.1(−4.0)	24.6(14.0)	0.49	28.3(17.0)	35.5(21.4)	0.81	−1.9(−1.1)	19.7(11.3)	0.54	17.4(9.9)	34.9(20.0)
Gaize	0.87	−22.2(−11.3)	13.3(6.8)	0.50	21.6(11.0)	37.7(19.3)	0.87	−13.8(−6.8)	15.8(7.8)	0.81	16.4(8.0)	26.4(12.9)
QHB	0.81	−2.5(−1.2)	23.7(10.9)	0.55	4.2(2.1)	39.5(19.4)	0.81	−10.6(−4.7)	23.5(10.6)	0.69	0.0(0.0)	32.1(14.5)
Mean	0.79	−12.6(−6.5)	19.6(10.3)	0.50	25.6(14.7)	32.6(17.9)	0.79	−6.9(−3.4)	19.6(10.2)	0.63	15.2(8.1)	33.2(17.4)
Southeast Asia												
MKL	0.65	−19.1(−4.9)	16.5(4.3)	0.39	−3.5(−0.9)	21.8(5.7)	0.10	−19.7(−5.0)	29.5(7.4)	0.66	−25.4(−6.4)	17.3(4.4)
SKR	0.54	−14.3(−3.7)	13.8(3.5)	0.42	−6.1(−1.6)	17.1(4.4)	0.71	−13.1(−3.4)	10.5(2.7)	0.55	−16.5(−4.3)	12.7(3.3)
Mean	0.60	−16.7(−4.3)	15.2(3.9)	0.41	−4.8(−1.3)	19.5(5.1)	0.41	−16.4(−4.2)	20.0(5.1)	0.61	−21.0(−5.4)	15.0(3.9)
Japan												
TKY	0.59	−41.5(−12.9)	34.1(10.6)	0.56	−14.5(−4.4)	36.9(11.3)	0.66	−16.7(−5.4)	22.6(7.2)	0.82	−29.8(−9.5)	16.1(5.2)
TMK	0.73	−19.8(−6.4)	23.4(7.6)	0.66	−5.0(−1.7)	27.7(9.4)	0.77	−12.2(−4.0)	19.8(6.6)	0.87	−17.7(−5.9)	14.5(4.8)
Mean	0.66	−30.7(−9.7)	28.8(9.1)	0.61	−9.8(−3.1)	32.3(10.4)	0.72	−14.5(−4.7)	21.2(6.9)	0.85	−23.8(−7.7)	15.3(5.0)
Four Regions Combined												
All Mean	0.73	−20.4(−6.9)	20.6(7.4)	0.54	4.4(3.2)	28.6(10.8)	0.71	−10.7(−3.5)	19.2(6.9)	0.74	−9.2(−1.8)	21.0(8.3)

Gui, S., Liang, S.L., & Li, L. (2010). Evaluation of satellite-estimated surface longwave radiation using ground-based observations. *Journal of Geophysical Research-Atmospheres*, 115(D18): D18214, doi: 10.1029/2009JD013635

提纲

Liang

- 背景
- 下行太阳辐射/天空”变亮”与”变暗”
- 地面反照率
- 下行长波辐射
- 地面温度，发射率和上行长波辐射
- 地面净辐射

Fig.2 Monthly averages of longwave upwelling radiation from two satellite products (ISCCP and GEWEX) and different GCMs in the IPCC AR4.

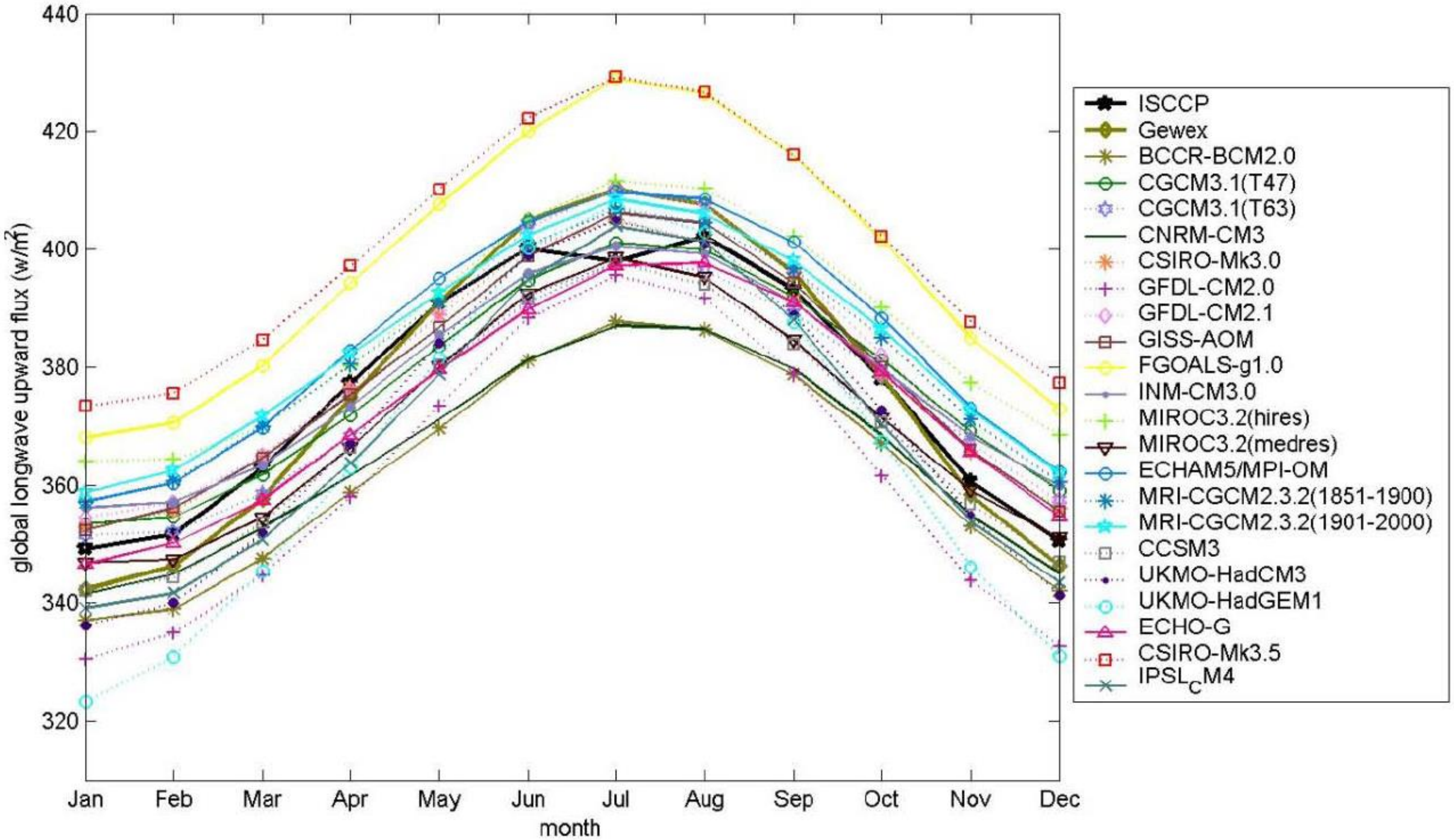

辐射平衡

Liang

$$R_n = R_n^s + R_n^l = (1-\alpha)F_d^s + \varepsilon F_d^l - \sigma\varepsilon T^4$$

albedo

Insolation

Emissivity

Longwave downward radiation

Skin temperature

MODIS split-window algorithm for determining surface skin temperature

Liang

$$T_s = C + \left(A_1 + A_2 \frac{1-\varepsilon}{\varepsilon} + A_3 \frac{\Delta\varepsilon}{\varepsilon^2}\right) \frac{T_{31} + T_{32}}{2}$$

$$+ \left(B_1 + B_2 \frac{1-\varepsilon}{\varepsilon} + B_3 \frac{\Delta\varepsilon}{\varepsilon^2}\right) \frac{T_{31} - T_{32}}{2}$$

$$\varepsilon = (\varepsilon_{31} + \varepsilon_{32})/2$$

$$\Delta\varepsilon = \varepsilon_{31} - \varepsilon_{32}$$

Emissivity determination

Liang

- Vegetation indices (AVHRR)
- Land cover classification (MODIS)
- Multispectral inversion method (MODIS & ASTER)
- Hyperspectral data
  - Cheng, J., **S. Liang**, Q. Liu, X. Li, (2011), Temperature and emissivity separation from ground-based MIR hyperspectral data, *IEEE Transactions on Geosciences and Remote Sensing*, 49(4): 1473-1484
  - Cheng J., **S. Liang,** J. Wang, and X. Li, (2010), A Stepwise Refining Algorithm of Temperature and Emissivity Separation for Hyperspectral Thermal Infrared Data, *IEEE Transactions on Geosciences and Remote Sensing*,48(3), 1588-1597

Multiple-band methods for determining both LST and emissivity

Liang

- Wan, Z.,&Li, Z. -L. (1997). A physics-based algorithmfor retrieving land-surface emissivity and temperature from EOS/MODIS data. *IEEE Transactions on Geoscience and Remote Sensing*, 35(4), 980–996.
- Gillespie, A.   Rokugawa, S.   Matsunaga, T.   Cothern, J.S.   Hook, S.   Kahle, A.B (1998), A temperature and emissivity separation algorithm for Advanced Spaceborne Thermal Emission and Reflection Radiometer (ASTER) images,., *IEEE Transactions on Geoscience and Remote Sensing*, 36 (4): 1113-1126
- Liang, S. (2001). An optimization algorithm for separating land surface temperature and emissivity from multispectral thermal infrared imagery. *IEEE Transactions on Geoscience and Remote Sensing*, 39(2), 264–274.

Convert narrowband emissivity to broadband emissivity

Liang

MODIS

$$\varepsilon = 0.227 + 0.188\varepsilon_{29} + 0.217\varepsilon_{31} + 0.359\varepsilon_{32}$$

Jin, M., S. Liang, (2006), Improved emissivity parametrization for land surface modeling using global remote sensing observations, *Journal of Climate*. 19(12):2867-2881.

Estimating LWUP

(1)Temperature-Emissivity Method

Liang

$$F_u = \varepsilon \int_{\lambda_1}^{\lambda_2} \pi B(T_s) d\lambda + (1 - \varepsilon) F_d$$

T_s MODIS LST (MOD11_L2)

ε Broadband emis (derived from MOD11B1)

(2) Hybrid Method

- Following the framework for hybrid methods
  - Emissivity Effect
    - UCSB Emissivity Library (59 spectra)
    - ~2000 MODIS Profile
- Statistical Analysis
  - Linear SULR Models (R^2: 0.990, RMSE< 5.42 W/m^2)

$$F_u = a_0 + a_1 L_{29} + a_2 L_{31} + a_3 L_{32}$$

  - Artificial Neural Network (ANN) Models (R^2: 0.996 RMSEs<3.7 W/m^2)

5 Models in total

θ	Model
0 º	
15 º	
30 º	
45 º	
60 º	

Representative thermal space-borne RS systems

sensors	**Wavebands (μm)**	# of bands	**Spatial resolution**
AVHRR	3.55 – 3.93 10.30 –12.50	1 2	1.1km
MODIS	3.66 – 4.08 8.400 – 13.48	3 4	1km
ATSR/ATSR–2/AASTR	3.55 –3.93 10.4 – 12.5	1 2	1km
ASTER	8.125 – 11.65	5	90m
TM/ETM+	10.00 –12.90	1	120m/60m
MSG–SEVIRI	8.30–13.0	3	3km at nadir
FY–3	3.7 – 4 9.59 – 13.49	2 4	1.1km
GOES	10.2 – 12.5	2	4km at nadir
GMS(Geostationary Meteorological Satellite)	3.5 – 4.0 10.3 – 12.5	1 1	4km at nadir
HJ–1B	3.50 – 3.90 10.5 – 12.5	1 1	150m 300m
METOP–IASI	3.2–15.5 (645–2760 cm^{-1})	8461	12km

Estimating LWUP: validation

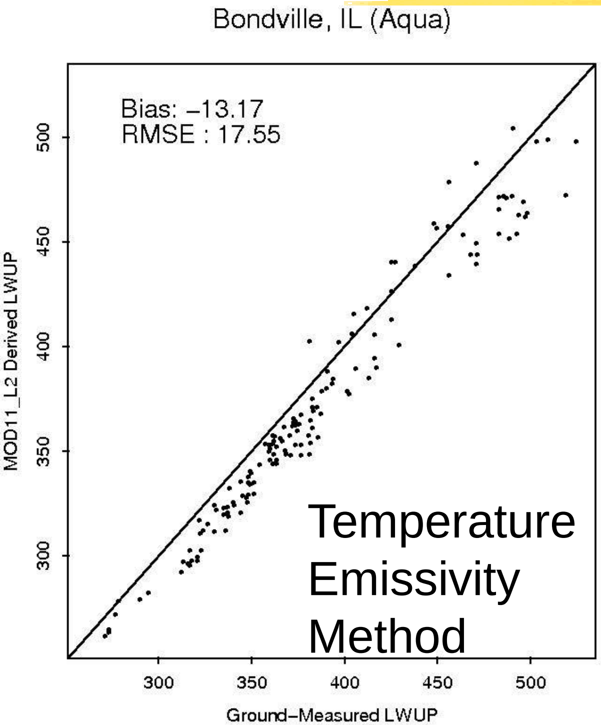

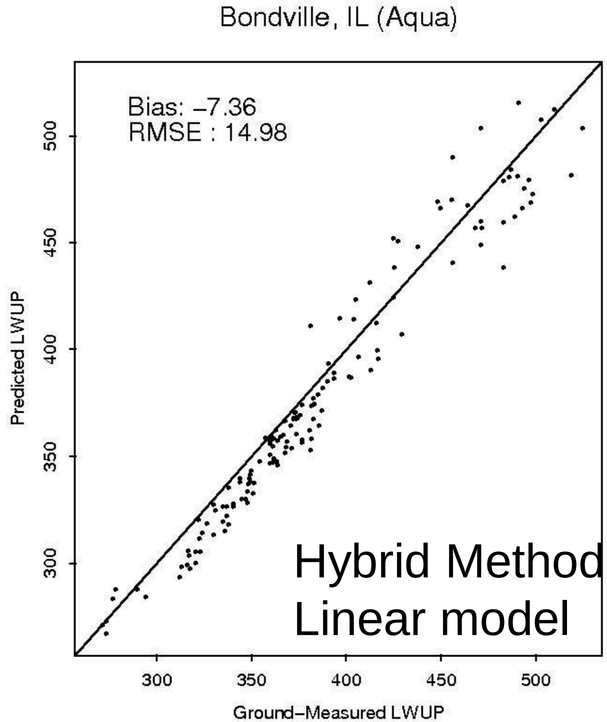

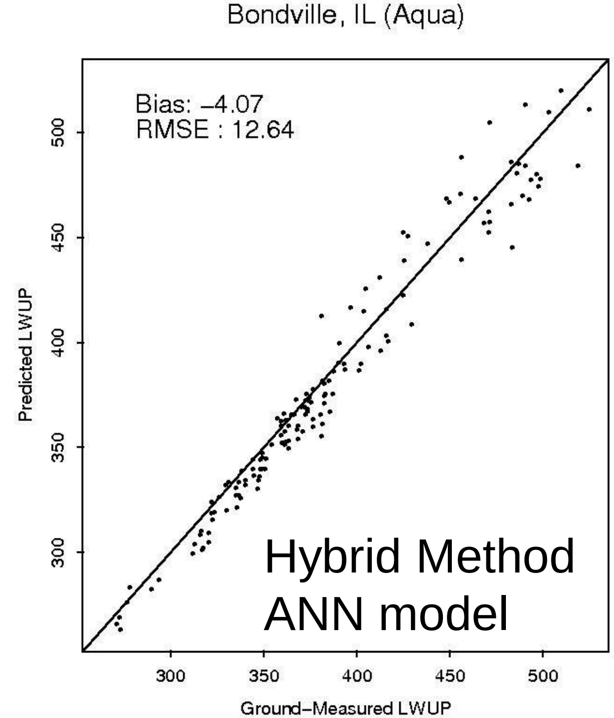

Bondville, IL (cropland, elevation 213 m)

- Smaller RMSEs in Aqua
- Hybrid method outperforms temperature-emissivity method
- ANN model outperforms linear model

Wang, W., S. Liang & J. A. Augustine, (2009),Estimating Clear-Sky Land Surface Upwelling Longwave Radiation from MODIS Data. *IEEE Trans. Geosci. and Remote Sens.* 47(5):1555-1570

MODIS LST validation

Liang

Summary of validation sites

Site	Latitude Longitude	Land cover	Canopy height (m)	Elevation (m)	Time period	# of data points	Instrument	Field Of view	Measurement height (m)
Brookings, South Dakota, USA	44.34529 −96.83617	Grassland	0.2–0.4	510	2004/113–2005/62	84	Apogee IR Radiometer	30°	4
Audubon Research Ranch, Arizona USA	31.59073 −110.51038	Grassland	0.1–0.2	985	2002/159–2005/063	466	Apogee IR Radiometer	30°	4
Canaan Valley, West Virginia, USA	39.0633 −79.4208	Grassland	0.1–0.5	988	2004/46–2004/307	36	Apogee IR Radiometer	30°	4
Black Hills, South Dakota, USA	44.15438 −103.6428	Conifer Forest	13–15	About 1700	2001/232–2004/143	126	Apogee IR Radiometer	30°	24
Fort Peck Indian Reservation, Montana, USA	48.30768 −105.10185	Grassland	0.2–0.4	634	2000/61–2005/146	531	Apogee IR Radiometer	30°	3.5
Hainich, Germany	51.07920 10.45218	Mixed broadleaf Forest	33	445	2004/51–2005/147	95	Schulzet radiometer	180°	44.0
Tharandt, Germany	50.96361 13.56694	Conifer Forest	26	380	2004/77–2004/350	82	Heitronics IR pyrometer	Only canopy is viewed	42.0
Bondville, Illinois USA	40.00621 −88.29041	Cropland (corn/soybean)	NA	213	2000/056–2005/050	390	Apogee IR Radiometer	30°	8–10

Wang, W., S. Liang, and T. Meyer, (2008), Validating MODIS land surface temperature products, *Remote Sensing of Environment*,112:623-635

MODIS LST validation

Liang

Summary of validation results

Site	MOD11_L2 (°C)		MOD07_L2 (°C)	
	Bias (MOD-GT)	RMSE	Bias (MOD-GT)	RMSE
Brookings	0.62	1.63	1.30	1.97
Audubon	0.72	1.31	2.98	3.74
Canaan Valley	0.04	1.42	1.20	2.08
Black Hills	0.15	1.48	3.14	4.10
Fort Peck	−2.19	2.51	0.34	2.70
Hainich	−2.21	2.51	−2.12	2.58
Tharandt	−3.23	3.44	−3.38	3.73
Bondville	−3.09	3.41	−0.16	2.50

Wang, W., S. Liang, and T. Meyer, (2008), Validating MODIS land surface temperature products, *Remote Sensing of Environment*,112:623-635

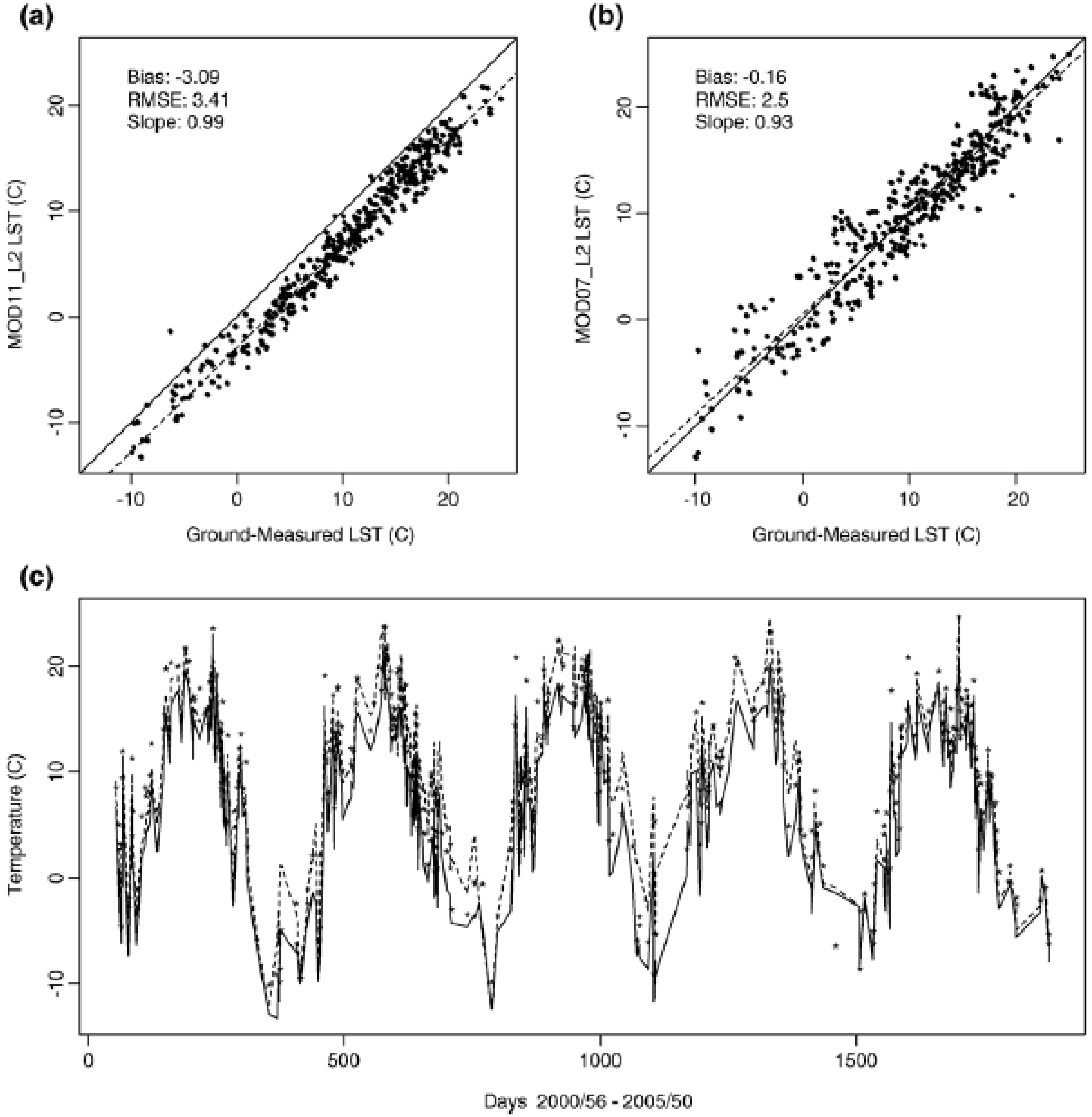

Fig. 8. Plots for Bondville cropland site (a) ground-measured LSTs vs. MOD11_L2 LSTs (b) ground-measured LSTs vs. MOD07_L2 LSTs (c) time series of MOD11_L2 LSTs (solid line), MOD07_L2 LSTs (dash line), and ground-measured LSTs (*).

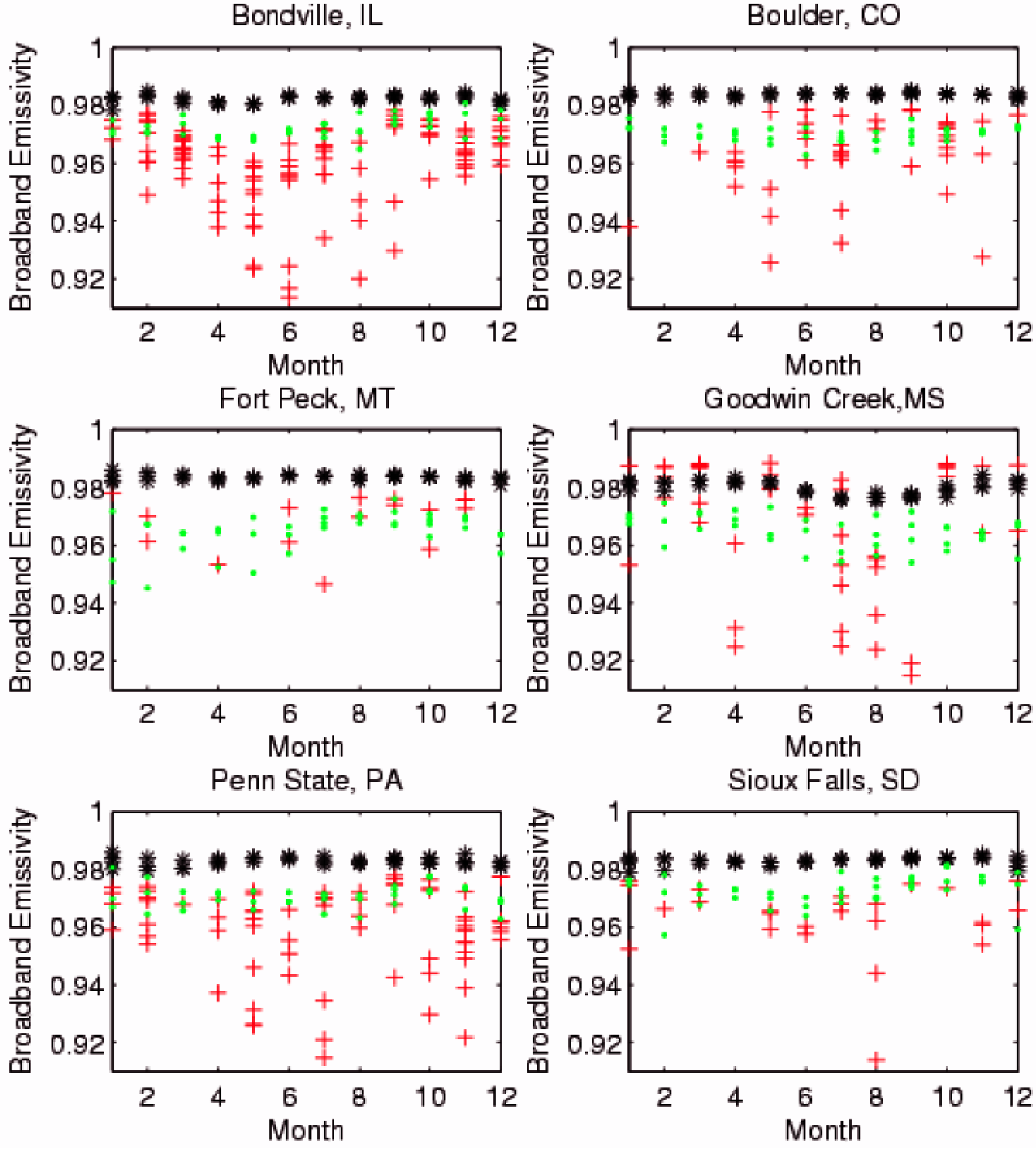

Broadband emissivity calculated from MODIS Collection 4 (green dot) and Collection 5 (black star) monthly emissivity products and ASTER daily emissivity products (red plus sign) at a resolution of 0.05° at six SURFRAD sites.

Wang, K., and S. Liang, (2009), Evaluation of ASTER and MODIS land surface temperature and emissivity products using surface longwave radiation observations at SURFRAD sites, *Remote Sensing of Environment*, 113:745-754

The emissivity impact on ground temperature in the coupled CAM2/CLM2 model, control run minus sensitivity run. Unit is K.

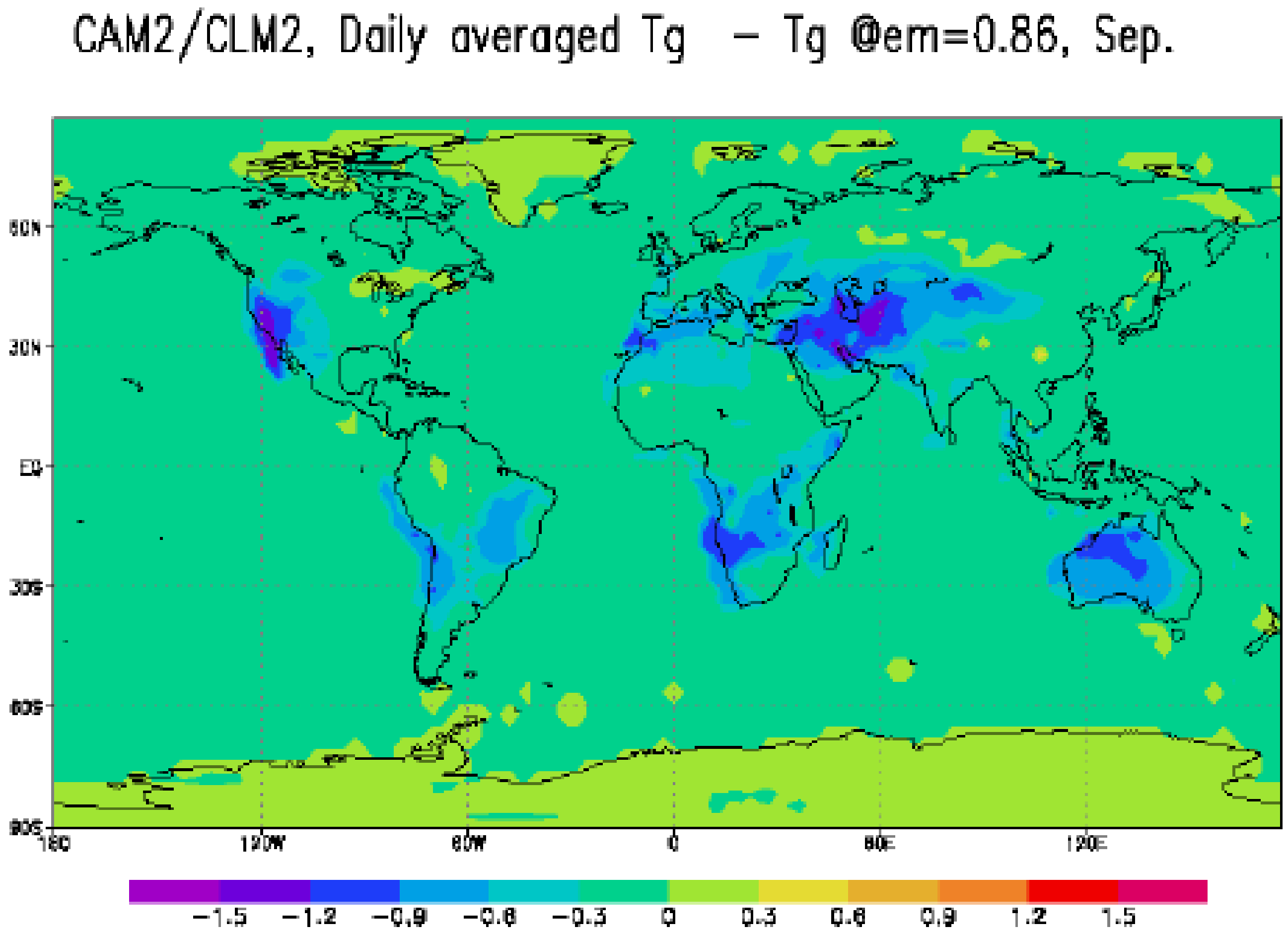

Jin, M., and S. Liang, (2006), Impacts of the MODIS broadband emissivity on GCM simulation, *J. Climate*, 19:2867-2881.

长波发射率 —全球已有产品

- 地表宽波段发射率是地表能量平衡估算的关键参数；
- 因缺乏有效的观测，气候模式中将其设置为常数或者采用简单参数化方案表征；遥感宽波段发射率能够显著改善气候模式的模拟精度（*）。
- 长时间序列、高时空分辨率全球陆表宽波段发射率仍属空白。

作者	方法	分辨率	光谱范围	用途	缺点
Wilber等	根据地表类型赋值	全球10′×10′	12个波段和宽波段(5-100μm)	辐射传输模式和NASA云与地球辐射能量系统	无法反映地表发射率的真实变化
Seemann等	基线拟合法	全球0.05°；月平均, 2000-2010	3.6-14.3μm内10个波段发射率	改善大气温湿度廓线反演精度	单一传感器；未验证
Pequignot等	多光谱方法	全球南北纬30°，月平均;三年; 1°×1°	3.7-14 μm; 0.05 μm	--	同上；空间分辨率太粗；

* Jin, M., & Liang, S. (2006). Improve land surface emissivity parameter for land surface models using global remote sensing observations. Journal of Climate, 19, 2867-2881

长波发射率—算法特色

- **GLASS BBE算法建立宽波段发射率和可见/近红外反射特性之间的函数关系，具有显著的创新性，为宽波段发射率的反演提供了新的视角；**
- **GLASS BBE算法有机结合了MODIS反照率产品和ASTER发射率产品的优势， 使得反演全球陆表8天、1公里宽波段发射率成为可能。**
- **GLASS BBE算法首次实现了基于AVHRR数据的全球宽波段发射率反演。**

Cheng, J., S. Liang, Y. Yao, X. zhang (2013). "Estimating the Optimal Broadband Emissivity Spectral Range for Calculating Surface Longwave Net Radiation." IEEE Geoscience and Remote Sensing Letters **10**(2): 401-405.

Ren, H., S. Liang, G. Yan, J. Cheng (2013). "Empirical algorithms to map global broadband emissivities over vegetated surfaces." IEEE Transactions on Geoscience and Remote Sensing: doi:10.1109/TGRS.2012.2216887.

Cheng, J. and S. Liang (2013). "Estimating global land surface broadband thermal-infrared emissivity from the Advanced Very High Resolution Radiometer optical data." International Journal of Digital Earth: in press.

GLASS 反射率

地点	测量值	ASTER	GLASS
Algodones	0.906	0.900	0.916
Great Sands	0.924	0.946	0.953
Kelso	0.907	-	0.928
Little Sahara	0.914	0.947	0.946
Stovepipe Wells	0.936	0.930	0.939

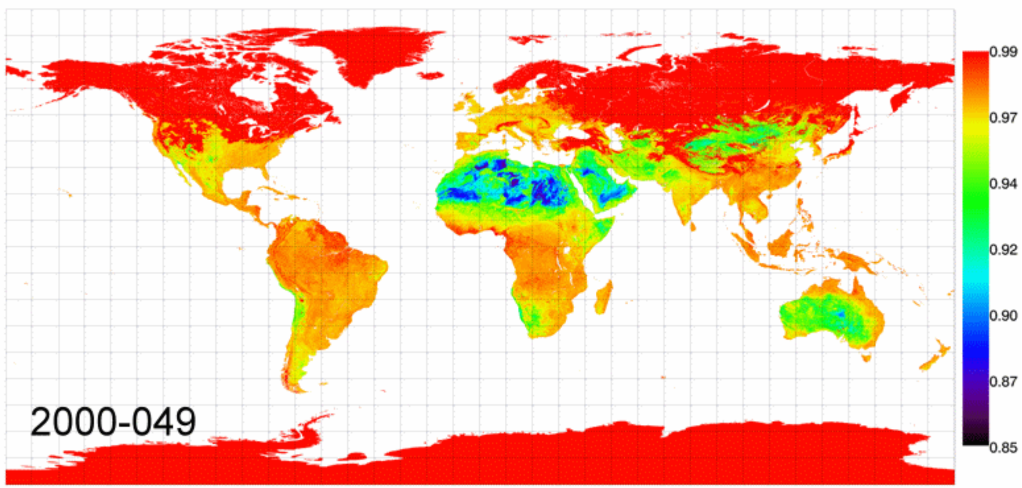

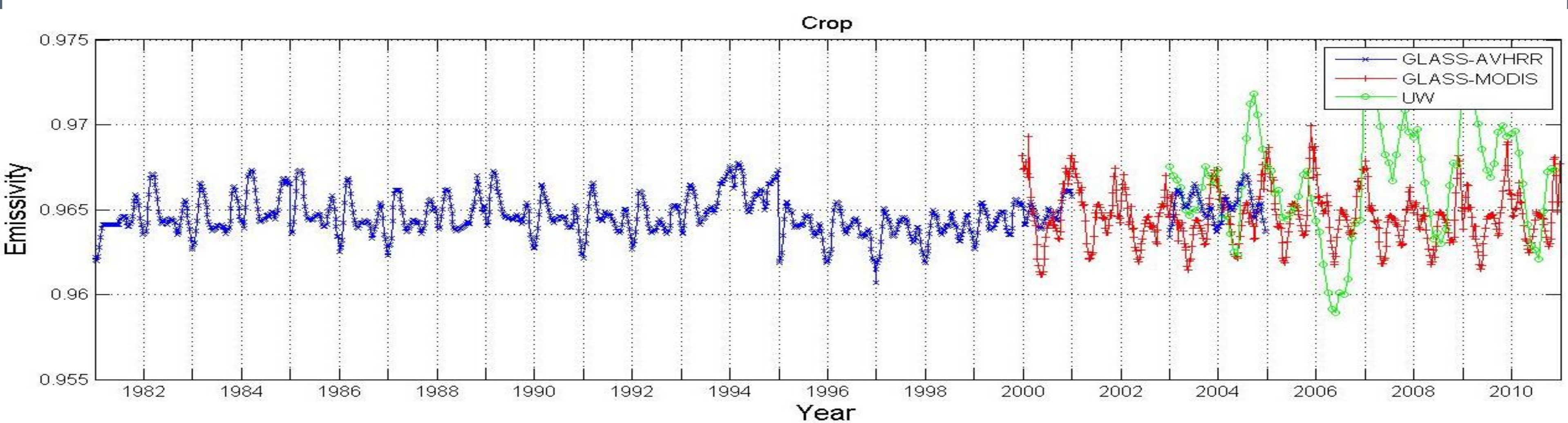

提纲

Liang

- 背景
- 下行太阳辐射/天空”变亮”与”变暗”
- 地面反照率
- 下行长波辐射
- 地面温度，发射率和上行长波辐射
- ET

地表蒸散发(Evapotranspiration, ET)是指通过土壤-空气、水-空气和植被-空气界面进入到大气中的水量。

它包括土壤、水体的蒸发(Evaporation)和植被蒸腾(Transpiration)，是地表能量平衡与水量平衡的重要组成部分。

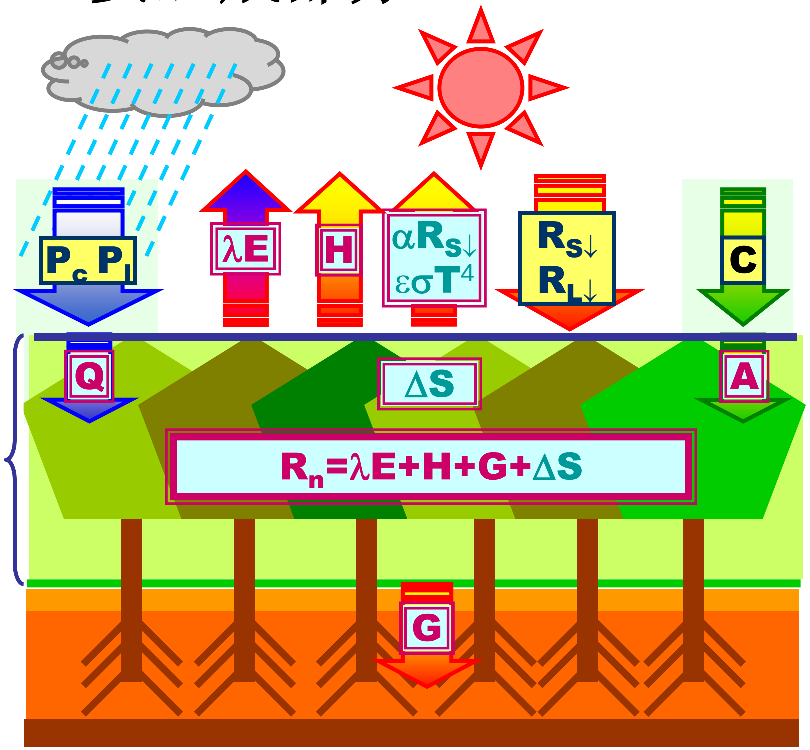

地表能量平衡

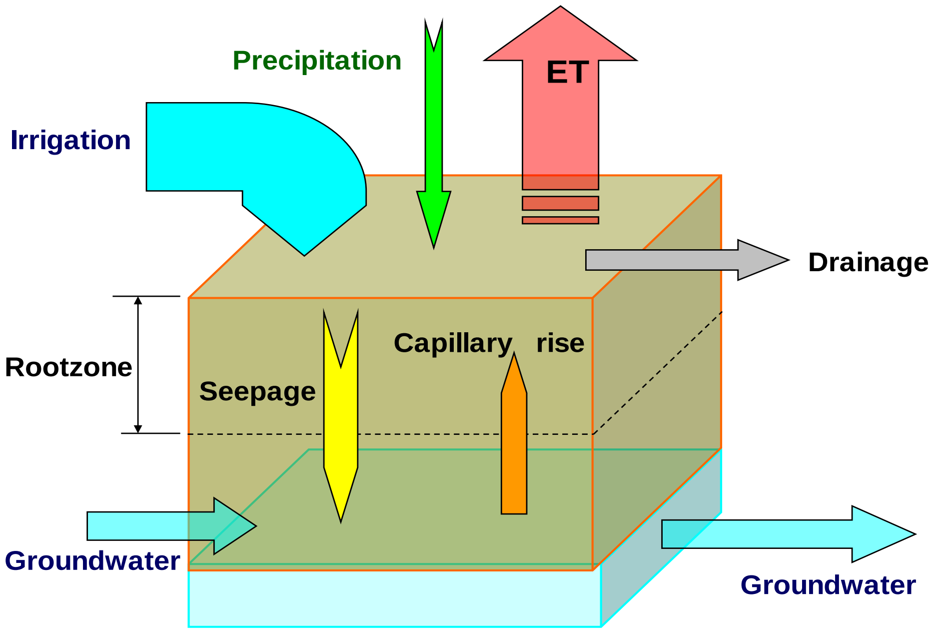

$$P + I = D + ET \pm R \pm \Delta S$$

地表水量平衡

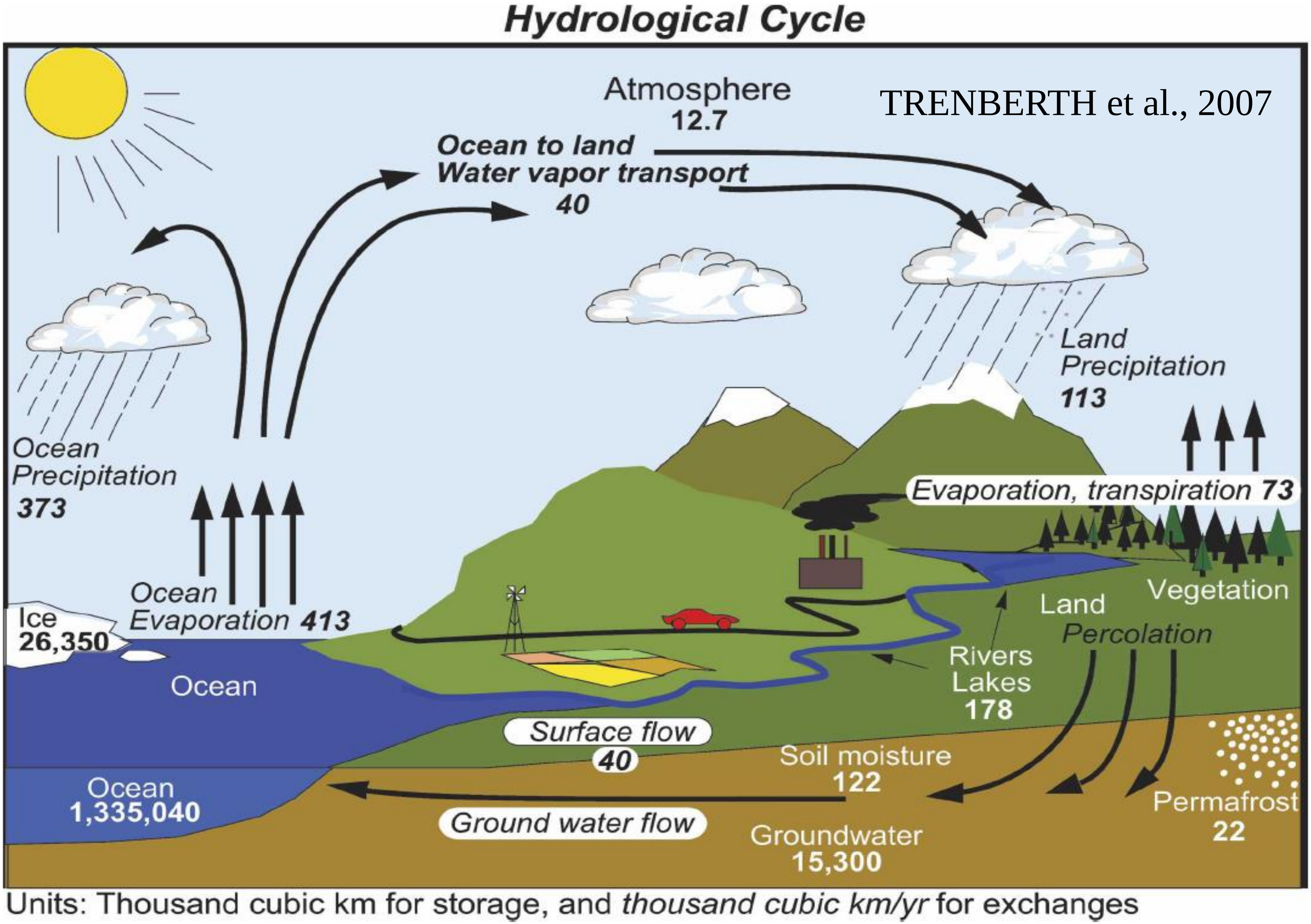

FIG. 1. The hydrological cycle. Estimates of the main water reservoirs, given in plain font in 10^3 km^3, and the flow of moisture through the system, given in slant font (10^3 km^3 yr^{-1}), equivalent to Eg (10^{18} g) yr^{-1}.

由于多时相、多波段、多角度的遥感信息能够综合反映下垫面的几何结构和水、热状况，使遥感方法在非均匀下垫面上区域蒸散发量的监测方面具有明显的优越性。

遥感估算蒸散发量的方法主要分为以下五类：

- **经验统计模型**
- **地表能量平衡模型**
- **与传统方法相结合的遥感模型**
- **温度-植被指数特征空间法**
- **数据同化方法**

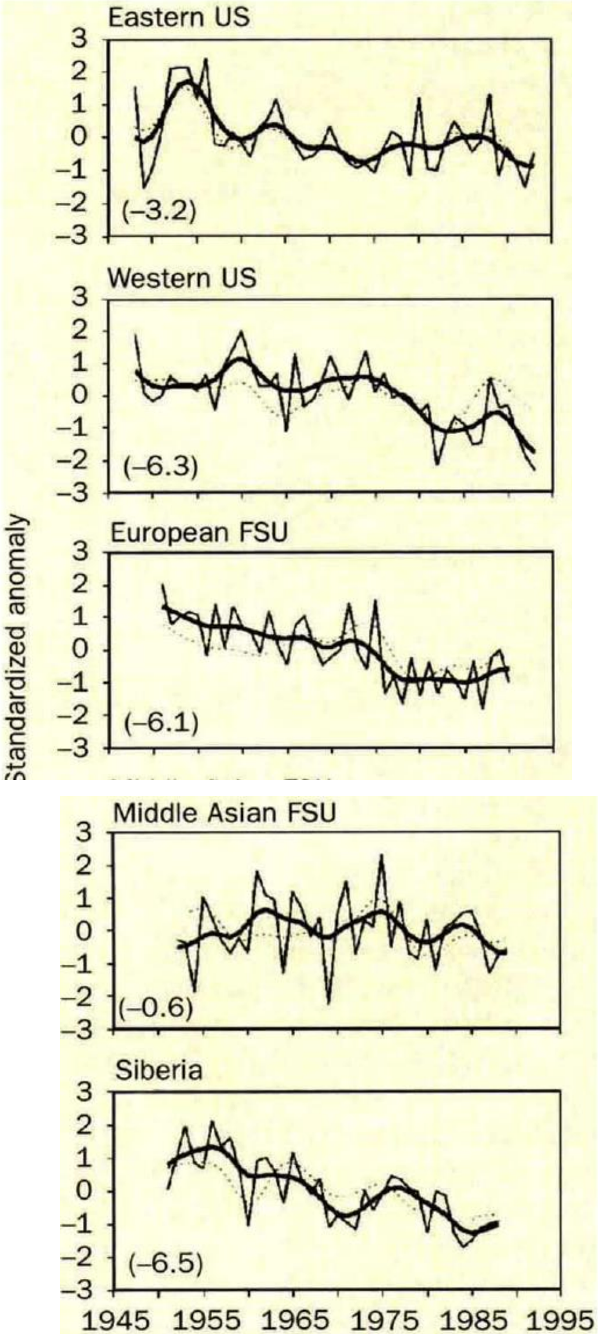

Peterson, T.C., Golubev, V.S. and Groisman, P.Y. 1995: EVAPORATION LOSING ITS STRENGTH. *Nature 377, 687-688.*

Farquhar 2002 *Science;*
Ohmura and Wild 2002 *Science*

85 sites in China

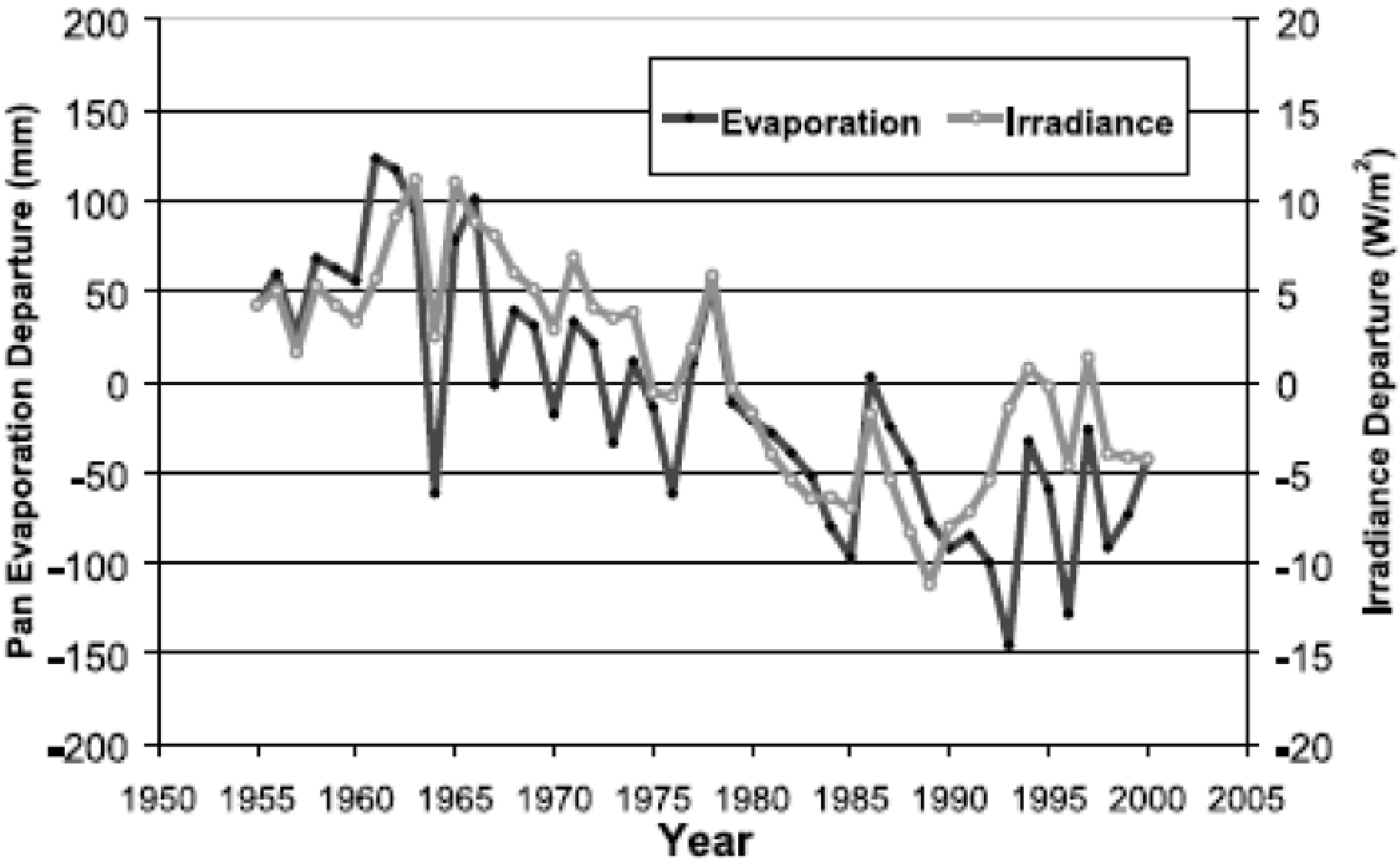

Qian et al. 2006 GRL

Impact on pan evaporation

Jung, et al., *Nature*, 2010

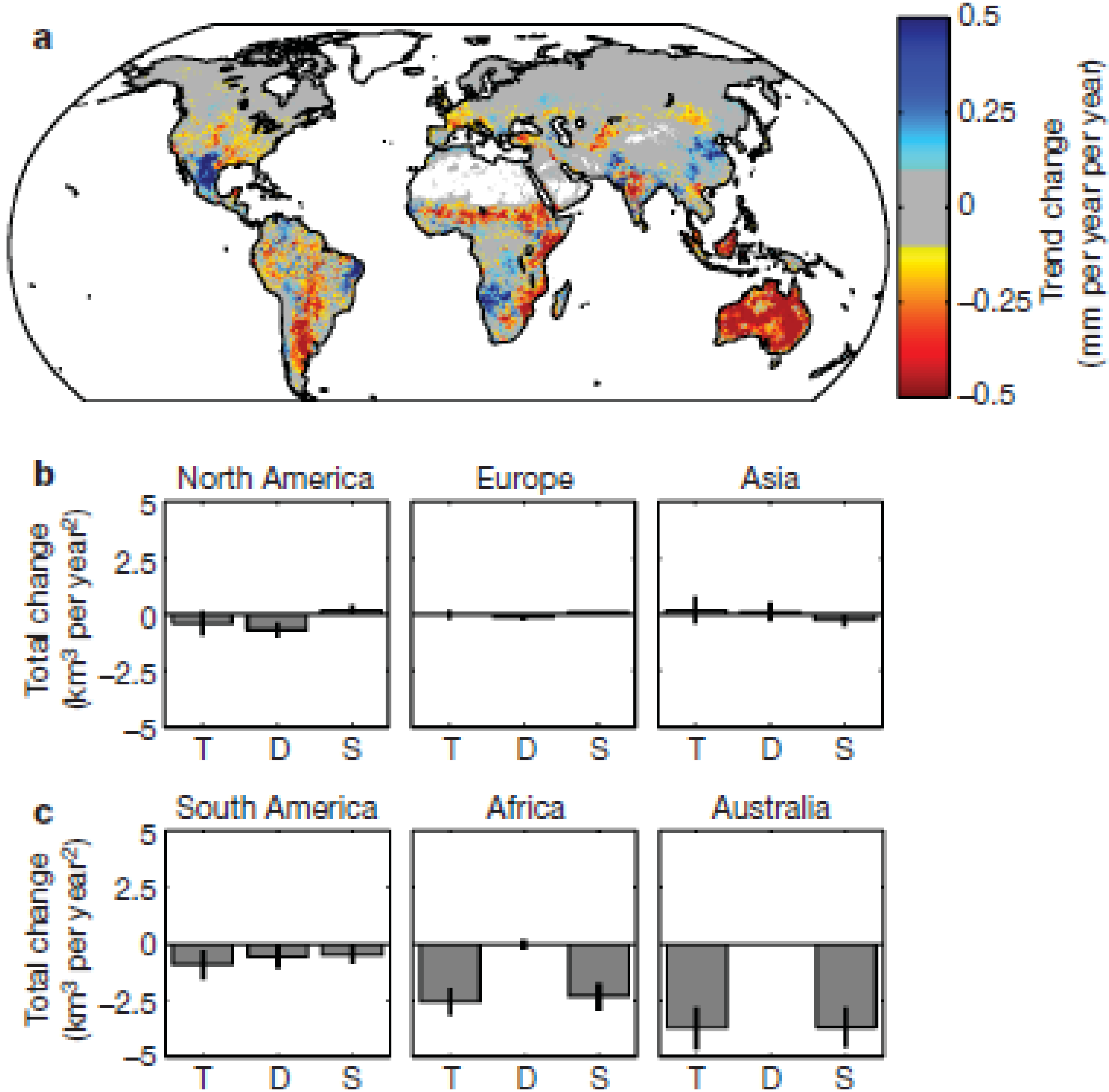

Figure 3 | ET trend changes. a, Map of the change in ET trend between 1982–1997 and 1998–2008 in millimetres per year per year. Small trend changes of ±0.1 mm per year per year are shown in grey to enhance clarity. Total

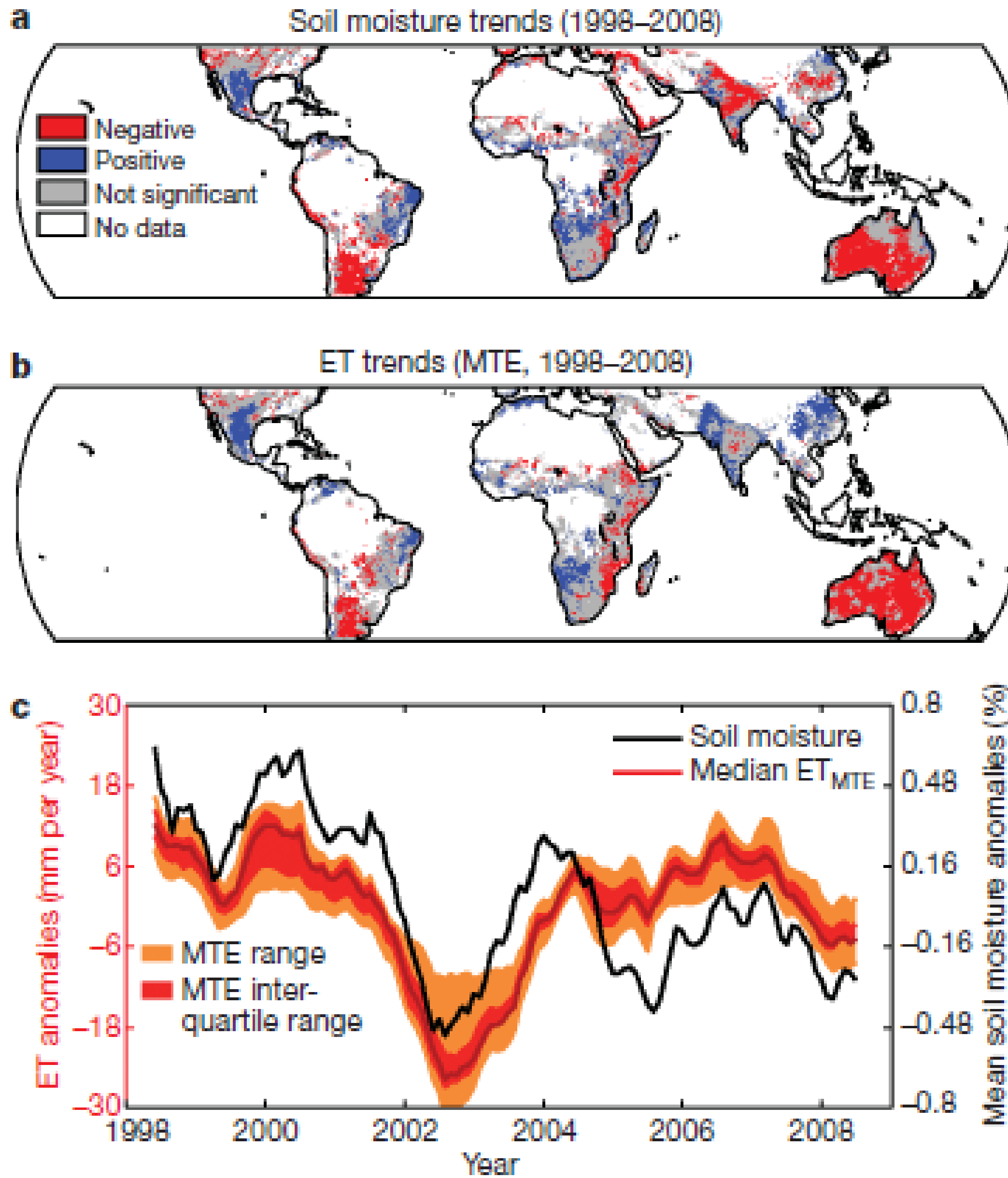

Figure 4 | Soil-moisture and ET trends. Significant ($P < 0.1$) soil-moisture trends derived from TRMM (**a**), significant ($P < 0.1$) ET trends from MTE (**b**) and mean ET and soil-moisture anomalies (seasonal cycle subtracted and filtered with an 11-month running mean) of all valid pixels of the TRMM

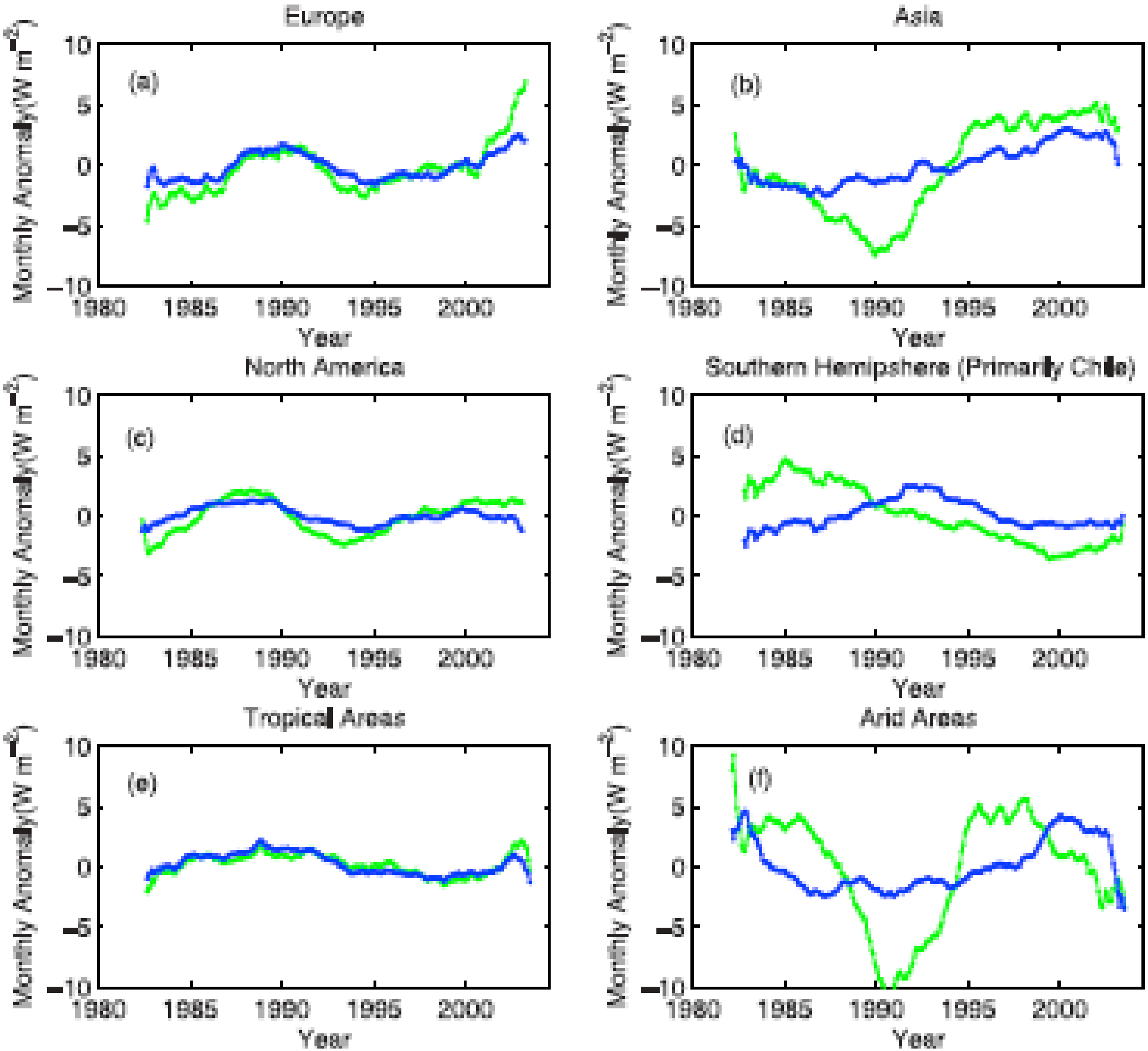

The times series of 5 year smoothed ET (blue line) and solar radiation Rs (green line) anomalies, Wang, Dickinson, Wild, Liang, JGR, 2010

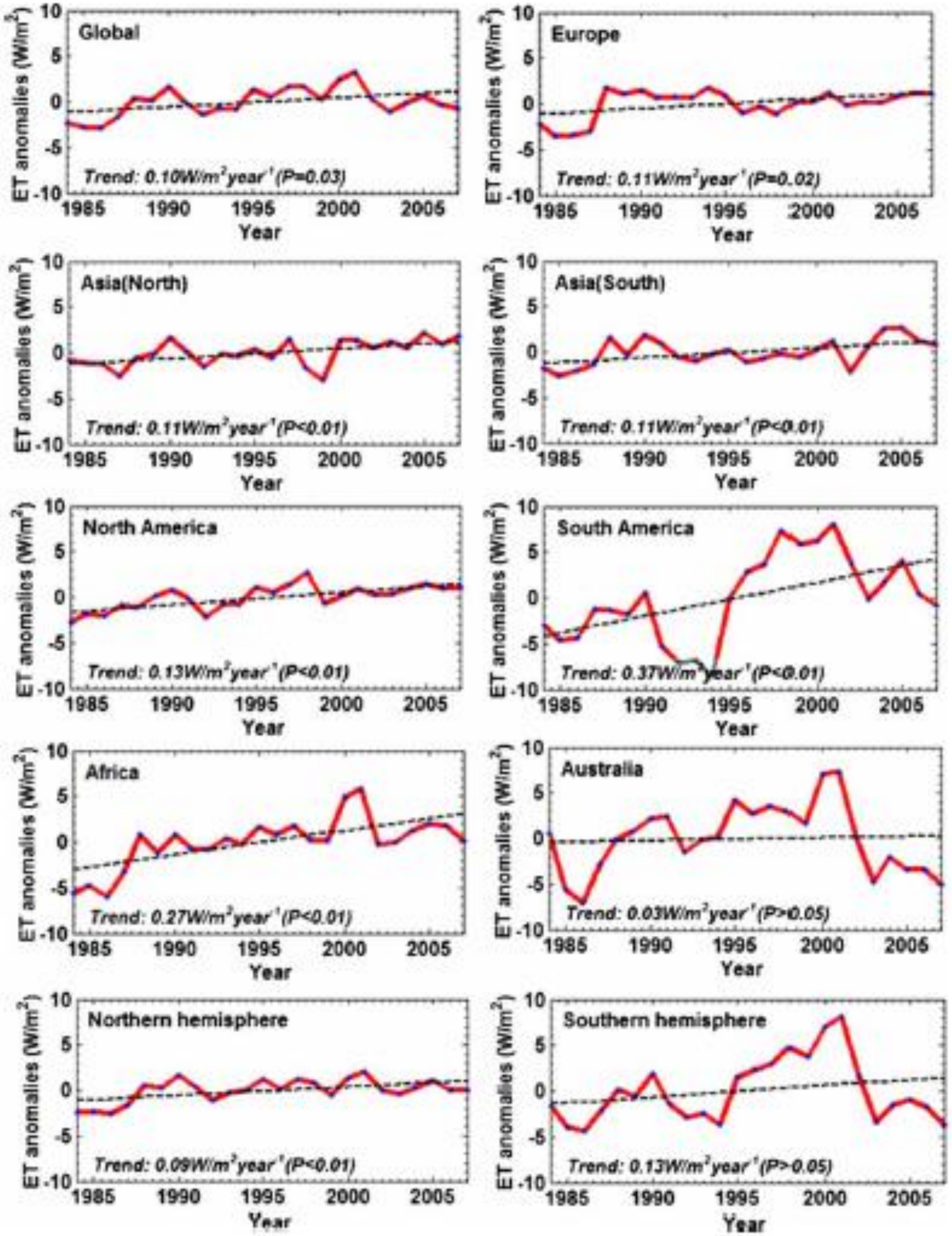

Figure 5. Regional and global land surface averaged monthly ET anomalies. Dashed lines represent the linear trends in the ET estimated using the ISCCP, AVHRR-GIMMS-NDVI and NCEP-2 datasets (unit: W/m^2 per year).

Yao, Y.J., Liang, S.L., Qin, Q.M., Wang, K.C., Liu, S.M., & Zhao, S.H. (2012). Satellite detection of increases in global land surface evapotranspiration during 1984-2007. International Journal of Digital Earth, 5, 299-318

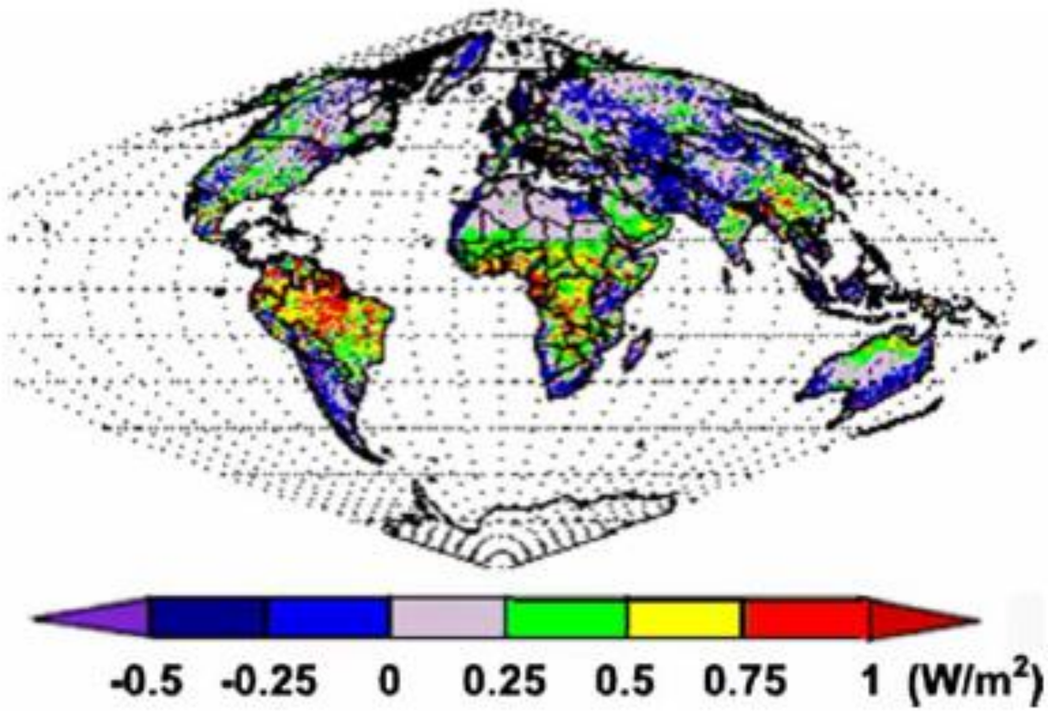

Figure 6. Maps of the linear trend in estimated global land surface ET from 1984 to 2007 using the ISCCP, AVHRR-GIMMS-NDVI and NCEP-2 datasets (unit: W/m^2 per year).

Summary

- Land surface radiation energy components are critical in various modeling and applications;
- Remote sensing estimated radiation products are urgently needed to calibrate/validate GCM models;
- High spatial resolution net radiation product from polar-orbiting satellite observations is also urgently needed for land applications;

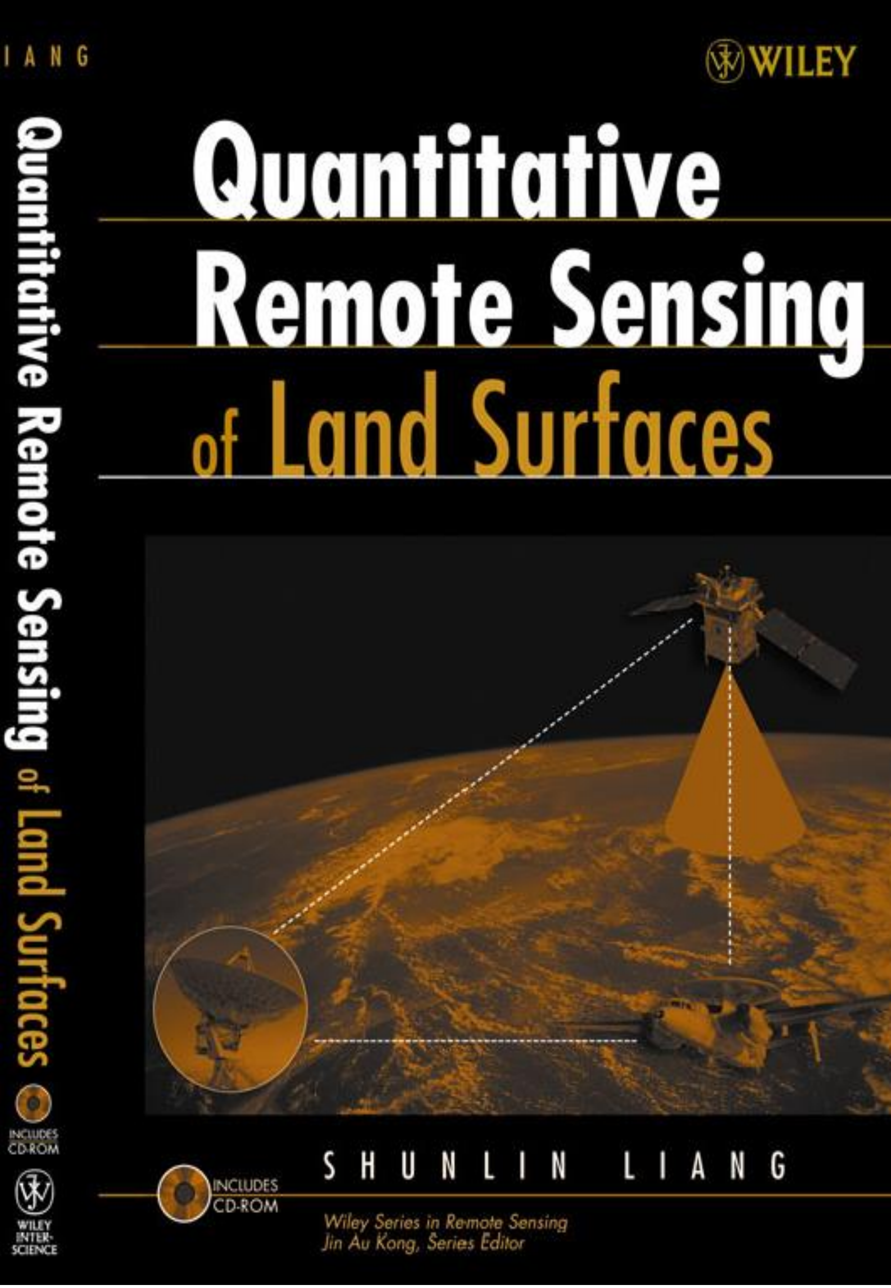
IANG
Quantitative Remote Sensing of Land Surfaces
INCLUDES CD-ROM
WILEY INTER-SCIENCE
WILEY
Quantitative
Remote Sensing
of Land Surfaces
INCLUDES CD-ROM
SHUNLIN LIANG
Wiley Series in Remote Sensing
Jin Au Kong, Series Editor


〔美〕梁顺林 著
范闻捷 等 译
定量遥感
科学出版社
www.sciencep.com
WILEY

Shunlin Liang
Editor

Advances in Land Remote Sensing
System, Modelling, Inversion and Application

This book collects the review papers from both technical sessions and three discussion panels of the 9th International Symposium on Physical Measurements and Signatures in Remote Sensing (ISPMSRS). It systematically summarizes the past achievements and identifies the frontier issues as well as the research agenda for the near future. It covers all aspects of land remote sensing, from sensor systems, physical modelling, inversion algorithms, to various applications. The papers on remote sensing systems evaluate the capabilities of different sensor systems for estimating key land surface variables and how they can best be improved and integrated effectively in the future. Papers on modelling and inversion review the state-of-the-art methodologies on physical modelling and the inversion algorithms for estimating a series of land surface variables. The papers on remote sensing application assess the current status of various applications and discuss how better to bridge the development of remote-sensing science and technology and practical applications. Representing the community effort and contributed by a team of international leading experts, this indispensable reference book for graduate students and practitioners of remote sensing also aids those engaged in academic research, government and industry.

Audience: This book will be of interest to graduate students, practitioners of remote sensing through academic research, government and industry.

CD Rom included:
This volume includes is a CD Rom containing the full colour images which are printed in Black and White in the book

ISBN 978-1-4020-6449-4
9 781402 064494

springer.com

Liang *Ed.*

Advances in Land Remote Sensing

Shunlin Liang
Editor

Advances in Land Remote Sensing

System, Modelling, Inversion and Application

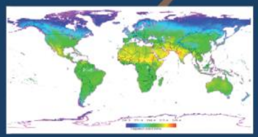

Springer

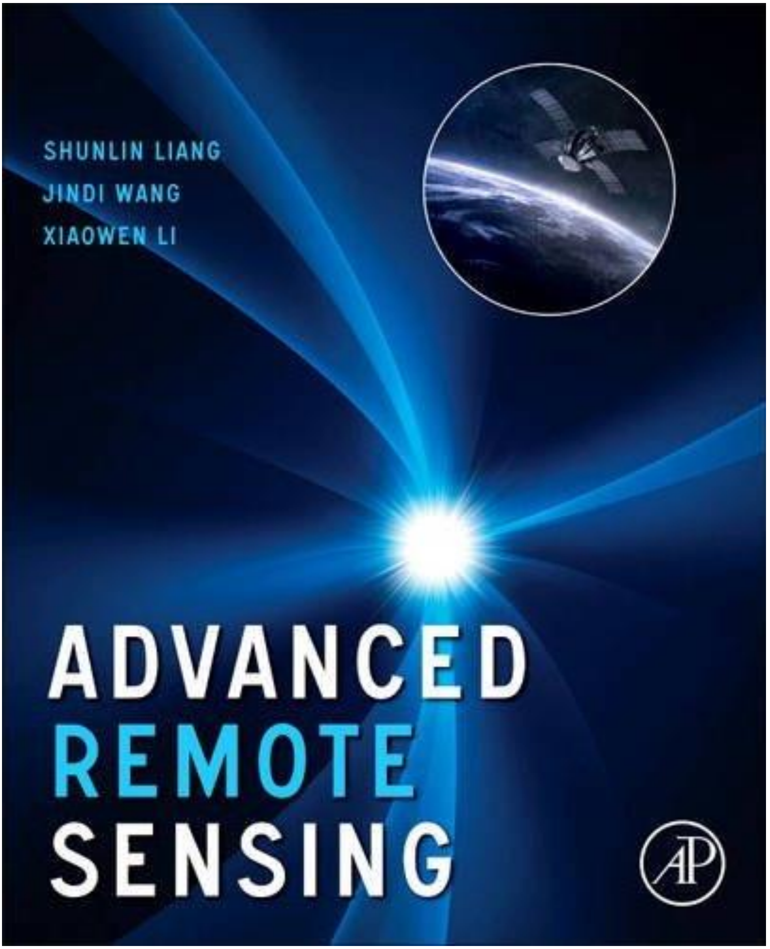

Publication Date: **August 24, 2012** |
ISBN-10: **0123859549** |
ISBN-13: **978-0123859549**

Thank you !